The impact of two-fluid MHD instabilities on the transport of impurities in tokamak plasmas

Jae Heon Ahn

NNT : **2016SACLX104**

Thèse de doctorat

de l'**Université Paris-Saclay**
préparée à l'**École Polytechnique**

École Doctorale 572 : **Ondes et Matière**
Spécialité : Physique des plasmas

The Impact of Two-Fluid MHD Instabilities on the Transport of Impurities in Tokamak Plasmas

par

Jae Heon Ahn

Thèse présentée et soutenue à l'École Polytechnique, le 24 novembre 2016

Composition du jury :

Prof. Jean-Marcel Rax	Professor at École Polytechnique	Chairman
Dr. Ian Chapman	Chief Executive Officer at UKAEA	Referee
Prof. Jonathan Graves	Professor at EPFL	Referee
Dr. Hinrich Lütjens	Research Director at CNRS	Director
Dr. Xavier Garbet	Research Director at CEA	Co-director
Dr. Rémy Guirlet	Research Engineer at CEA	CEA supervisor

Laboratoire d'accueil :
Institut de **R**echerche sur la **F**usion
par confinement **M**agnétique
CEA – Cadarache
F-13108 Saint-Paul-lez-Durance, France

What shall I render unto the LORD
for all his benefits toward me?
- Psalms 116:12

Acknowledgments/Remerciements/감사말

24th December 2016, Paris.

Although only my name figures on the front page, I do admit that this manuscript is a fruit of a full support and encouragement from those around me. This thesis also marks the end of a chapter in my life during which I spent more than 10 years in France as student. In this occasion, I would like to thank from all my heart those who have stood on my side during this unforgettable adventure.

I would like to start with the reviewers, Dr. Ian Chapman and Prof. Jonathan Graves, for the evaluation of my thesis and for their valuable comments to improve it. Je remercie Prof. Jean-Marcel Rax pour avoir accepté de présider la soutenance. Ce fut un honneur pour moi d'y avoir assisté à ses cours de Master, où j'ai pu découvrir le monde de la physique des plasmas de tokamaks.

Pendant ces 3 années de thèse, j'ai été encadré par, ce que je peux appeler la 'Dream team'. Tout d'abord, je tiens à remercier Xavier pour m'avoir donné l'opportunité de travailler sur ce sujet. Malgré que la liste des louanges que les thésards précédents ont déjà faites est complète, je vais quand même essayer de garder l'originalité. Merci pour ta patience et la direction tout au long de la durée de stage et de la thèse. J'avais l'impression d'avoir un wikipédia vivant avec moi, sans oublier les discussions en dehors du cadre scientifique. Je trouve dommange que ma manque de culture générale était le facteur limitant pour comprendre tous tes humours. Ensuite, je remercie Rémy qui était toujours disponible à mes questions, pour des discussions qui m'ont permis d'éviter de rester dans un monde 'virtuel'. Je pense aussi à la générosité des sourires dont il m'a fait cadeaux, même lorsque mes blagues étaient de mauvaise qualité. Enfin, j'ai été beaucoup aidé par Hinrich, malgré la distance physique entre Palaiseau et Cadarache. Il a dû subir mes inombrables questions sur le code XTOR-2F, avec patience et toujours à l'écoute. Mes 3 encadrants de thèse ont été de bons exemples, non seulement en tant que chercheurs et encadrants, mais aussi en tant que personnes, dont je me référerai au long de ma carrière.

Je suis reconnaissant à l'administration de l'IRFM pour leurs intérêts sur ce sujet et les supports financiers qui m'ont permi de partager les travaux de thèse avec la communauté scientifique grâce aux collaborations internationales et participations aux conférencess. Je remercie le chef de l'institut Alain Bécoulet, les chefs du service et du groupe de l'époque du SCCP, Xavier Litaudon et Roland Sabot, et de l'ère du SPPF actuel, Frédéric Imbeaux et

Rémi Dumont. D'autant plus, je n'oublie pas Valérie et Nathalie du secrétariat du service qui ont contribué au bon déroulement de la thèse grâce à tous leurs travaux admisnistratifs fournis derrière la scène.

Je dois beaucoup à l'équipe XTOR-2F qui s'est rassemblée autour de l'arbre virtuelle, nommée 'GitLab'. D'abord, je remercie Patrick M. qui a dû s'occuper de tous les dossiers et les rapports pour les demandes d'heures de calculs. Ensuite, un grand merci à Olivier avec qui j'ai passé le temps à déchiffrer et débugger le code. Je n'oublie pas son talent exceptionnel en conduite (surtout des camions), son esprit aventurier en cuisine, et son amour envers les burgers. J'ai eu la grande joie de lui connaître et partager ces 3 ans et demi de stage et thèse autour des discussions scientifiques ou non, utiles et inutiles. Enfin, je souhaite bon courage à Fabien qui poursuivra l'aventure.

C'était une énorme chance, honneur et privilège pour moi, de pouvoir passer ces années entouré des collègues et amis, avec autant de qualités scientifiques, en plus, de qualités humaines. Un grand merci aussi aux collègues du 1er étage du bâtiment 513 - Chantal, Guilhem, Guillaume, Gloria, Marina, Maurizio, Patrick T., Virginie, Tuong - pour l'ambiance chaleureuse et les discussions abordant diverses sujets autour du café à 10h (9h30 maintenant). Je remercie particulièrement Yanick, Philippe et Pascale pour l'enseignement et les conseils qu'ils m'ont donné depuis le Master. Je suis aussi très reconnaissant à Jean-François Mahieu et Yannick Mineo pour leurs supports lors des problèmes informatiques, malgré le surcharge de travail.

Je tiens aussi à remercier mes amis qui étaient/sont à Cadarache, avec qui j'ai pu partager des moments de bonheur et qui m'ont supportés lors des moments les plus nuageux avec des encouragements. David Z. - dont j'ai malheureusement raté sa tournée de croissants, Jorge - en possesion de tant d'énergie et du dynamisme qui viennent probablement des bons rhums, Didier - expert des cookies et amoureux des choux-fleurs, Timothée - qui m'a beaucoup aidé à l'utiliser le code XTOR-2F et futur lauréat du prix Nobel, Claudia et Farah - avec qui j'ai eu l'honneur partager le bureau pendant mon stage, François - le 1er étage du 513 manquait de la couleur rouge sans lui, Thomas (a.k.a 'TC') - un mur d'une chambre insonorisée pourrait être conçue en utilisant sa barbe, Jean-Baptiste - le futur ministre voire monsieur le président, Damien - Tony Parker normand et le camarade avec qui j'ai partagé la souffrance lors du déchiffrement de la théorie du transport néoclassique des impuretés, Alexandre - le capitaine de l'équipe de foot 'IRFM' décorée par la victoire de la coupe (ultra-consolante) de Cadarache, Clothilde - ma 'co-bureau' à temps partiel, Hugo (a.k.a 'Bobiz') - laveur de pare-brise moustachu et/ou barbu, Laurent Valade - en possession d'un atelier dans son studio et passionné par ce qu'il appelle la 'science alternative', Etienne - admirateur de la musique de Maître Gims, Nicolas - le nouveau capitaine de foot et habitant de la grande ville de Manosque (fier de l'être!), Camille - ex-Marseillaise qui recherche de l'air fraîche, Charles - le chef de la section constituée des électrons 'lourds', Christian - amoureux

des hamiltoniens, Adrien et Axel - les étoiles émergentes de Youtube, Julien Denis (et Denis Julien) - qui ont offert de quoi rigoler aux thésards grâce à leurs échanges de courriels intimes, Rennan - une petite touche brésilienne à l'institut, Alberto - expert des noisettes de café, Matteo - MV800, Davide - basketteur de base mais meilleur buteur de l'équipe de foot, Peter - le nouveau manosquien (très bon choix) et maître des collisions, Elisabetta - qui en profitera bien du bon emplacement de mon ancien bureau pendant les 3 prochaines années.

I also thank the collaborators from outside IRFM with whom I had the opportunity to have fruitful exchanges - Prof. Cassio Amador, Dr. Jonathan Citrin, Prof. Olivier Sauter, Dr. Marco Sertoli, Tomas Odstrcil and Alexander Lessig.

Je n'oublie pas mes amis depuis la classe prépa et de l'école díngénieur qui m'ont encouragé de loin pendant ces dernières années. Je pense spécialement à Quentin (a.k.a. Big-Légowski), Jinlei (a.k.a. l'inou ite), Mathieu, le capitaine Victor Neel (a.k.a. 'binôme'), Joachim Fleury (a.k.a. McFleury). Je dois beaucoup aussi à Dr. Jean-Marie Thiebaud et Soeur Hélène Lebrun qui m'avaient donné l'idée de venir faire mes études en France.

Now, I would like to write a long text for my Korean friends who encouraged me from far away. 먼저, 내가 한국에 들어면 따로 시간을 내어줘서 나의 근황을 들어준 친구들에게 고맙다는 말을 하고 싶다. 중학교 때부터 친구인 희만이와 영래, 나의 몇 안 남은 고등학교 친구들 윤영, 선희, 샛별, 그리고 하비에르 출신 친구들 선동, 웅돈, 지연.

내가 프로방스에서 지낸 4년이 조금 안 되는 기간 동안에 나의 시시콜콜한 이야기와 푸념들을 들어주시고, 따뜻하게 챙겨주시고, 무엇보다 Marseille의 Hard Rock Café라는 신세계를 알게 해주신 고마운 분들도 있었다. 여명이형, 우연누나 그리고 사랑이, 정현이형, 고은누나 그리고 삼형제 주진, 주언, 주아, 내 끝없는 잡담을 무한한 인내로 들어준 수영누나에게 고마운 마음을 전한다.

프랑스에서, 특히 파리에서 지낸 6년 반의 시간은 내 인생의 전환점이라 할 수 있다. 무엇보다 신앙적으로 주님과 가까워지는 시간이 되었기 때문이다. 항상 기도와 응원의 말들을 해준 파리장로교회 식구들에게 감사 드린다. 특별히, 말씀으로 훈련시켜 주신 이극범 목사님과 매년 잊지 않으시고 생일카드를 보내 주신 김숙희 사모님, 그리고 일대일 양육을 지도해 주신 스승님 이동원 집사님께 진심으로 감사드립니다.

때론 신앙의 멘토이자 기도의 동역자로, 때론 내가 가족과 떨어져 지내는 유학생활 동안에 가족 같은 따뜻함으로 보살펴 주셨던 집사님, 권사님, 청년부 형제, 자매들에게 정말 감사합니다. 김상용 집사님, 김미정 권사님, 이윤수 집사님, 최만식 집사님, 임은희 권사님, 한충희 장로님, 김경희 권사님, 백채훈 집사님, 김신재 집사님, 정욱 집사님, 백성미 권사님, 김수정 집사님, 이역녀 집사님. 그리고 재욱이형, 승연이형, 성혁이, 재민이, 장현이, 경준이. 예전에 한창 그랑제꼴 시험 볼 때 선뜻 자신의 기숙사 방을 내 주었던 준원이형, 창현이형, 태우형. 파리 올 때마다 내가 매장으로 쳐들어가도 반갑게 맞이해 주고 귀한 교제를 나눈 상훈이형과 수연이 부부. 매년 송구영신 예배 후, 단 둘이 따로 만나 한 해를 함께 돌아봤던 지섭이. 친동생 같았던 영원한 축구 9번 유망주 창훈이. 갈 곳 없는 나그네에게 따뜻한 잠자리를 선뜻

내어준 재홍이, 단열이. 논문 발표하는 날 멀리까지 응원하러 고마운 발걸음을 해 주었던 날아, 가영이, 경명이. 네버엔딩 수다의 끝장판을 함께한 소울메이트급의 제니누나.

멀리서 중보기도로 응원해 주신 가족과 친척들에게 감사드립니다. 특별히, 한국에 들어갈 때마다 따뜻하게 맞이해 주시고 세심하게 챙겨주신 외가 친척들에게 진심으로 감사의 뜻을 전하고 싶습니다. 우리 가족의 기도의 뿌리이신 대한민국의 Willam Booth (a.k.a. K-Booth) 외할아버지, 큰삼촌, 작은삼촌, 작은외숙모, 이모, 이모부, 세미누나, 매형, 세찬이형, 형수, 그리고 매번 나의 기쁨이 되어준 사랑스러운 조카들 정원이, 서원이, 주원이, 진원이.

아마도 먼저 길을 열어준 형이 없었다면 분명 지금의 나는 없었을 것이다. 아무도 모르는 곳에 혼자 유학 나와서 고생하고 있었던 형. 함께 있을 때는 괴롭히고, 옆에서 장난치는게 귀찮기만 했지만, 형이 한국 들어가고 나서부터 느낀게.. 우리가 이렇게 오래 떨어져 지낼 줄 알았으면 진작 파리에서 더 많은 추억들을 만들면서 지냈을걸 하며 종종 후회한다. 앞으로도 서로를 위해 중보하고 늘 힘이 되는 삶을 하자.

무엇보다 새벽마다 기도의 제단을 쌓으신 부모님이 없었다면 이 모든 것이 존재하지 않았을 것이다. 부모님께서 내게 신앙의 뿌리를 심어주셨기에 수많은 풍파 속에서도 두려움 없이 이 곳까지 걸어올 수 있었던 것이다. 내가 늘 부족함 없도록 지원해 주신 아빠, 그리고 나를 도와주러 선뜻 먼 길도 마다하지 않고 비행기로 오고 가신 엄마 감사합니다. 그 어떠한 말로도 이 감사함은 표현이 안되리라 생각합니다. 사랑합니다.

Finally, may all glory and honour be to God alone, for You led and will lead my path throughout my life.

Soli Deo Gloria

* *
*

Contents

CHAPTER 1

Introduction

Contents

1.1 Fusion energy on Earth

The worldwide energy consumption has been increasing due to continuous industrialization and way of life sophistication. Statistics show that the vast majority of the world's energy is currently generated from combustion of fossil fuels (Figure 1.1). Indeed, abundance of resource and relative technological simplicity make this process an attractive energy source. However, fossil fuel combustion produces large quantities of greenhouse gases such as carbon dioxide, resulting in acid rain and contributing to global warming. Drastic meteorological events related to climate change have been causing serious human and material damage regardless of country. Moreover, experts make more pessimistic predictions for the future. This sense of urgency has led the government leaders around the world to agree and engage for actions to reduce greenhouse gas emission at the COP21 conference[1].

Active research is ongoing to develop alternative energy sources. Renewable energy sources such as solar, wind and biofuel promise to generate power in a sustainable manner. However, these alternatives are currently far from providing large scale supply to replace fossil fuel consumption. Nuclear energy is interesting in terms of specific energy, which is the energy

[1] United Nations Climate Change Conference (http://www.cop21.gouv.fr)

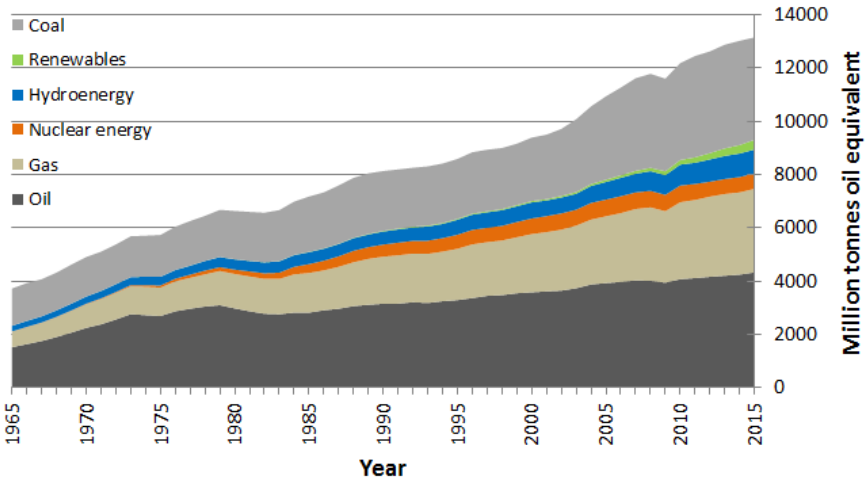

Figure 1.1: World energy consumption since 1965 for different energy sources[2]. The units are in million tonnes for oil and million tonnes oil equivalent for other energy sources. A tonne oil equivalent equals approximatively 12 MWh of electricity.

stored in a system per unit mass. Indeed, the specific energy for conventional nuclear fuels is about a million times larger than other energy sources relying on chemical reactions. Nowadays, nuclear energy is generated by fission which consists in breaking heavy atoms into lighter by-products. Despite its efficiency, issues on radioactive waste and safety are still raised, combined with geopolitical concerns related to the non-proliferation of nuclear weapons. Efforts are concentrated on seeking plausible solutions for these issues.

Another way to generate nuclear energy is by fusing light nuclei to form a heavier atom. Fusion reaction, by which stars are fuelled, is common in the universe. It is a very attractive option due to its inherent safety and the abundance of the fuels on Earth. For these reasons, plasma physicists have been focusing on studying the feasibility of sustained fusion reaction on Earth, in order to supply a significant portion of the energy consumption. The first magnetic confinement device was built in the former USSR at the end of 1950s. An international collaboration is ongoing around the ITER project which is currently under construction at Cadarache (France). Seven member entities are participating in this project - China, the EU, India, Japan, Korea, Russia and the USA. Commercial fusion reactors are expected probably for the next century.

In this section, general principles of fusion are briefly presented in Section 1.1.1. Among different fusion devices which have been developed, tokamaks are currently the most advanced concept in terms of performance. Section 1.1.2 is dedicated to a description of a tokamak, as this thesis deals only with the physics of tokamaks.

1.1.1 General principles

For a nucleus with $\mathcal{A}$ nucleons ($\mathcal{Z}$ protons and $\mathcal{N}$ neutrons, respectively noted p and n), its mass m is smaller than the mass of its constituents $\mathcal{Z}m_{\mathrm{p}} + \mathcal{N}m_{\mathrm{n}}$. The binding energy

[2]Data from BP statistical review of world energy 2016 (http://www.bp.com)

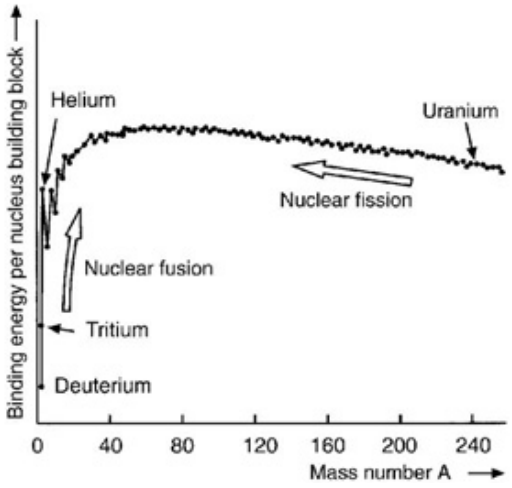

Figure 1.2: Aston's curve which represents binding energy per nucleon versus mass number.

defined as

$$\mathcal{B}(\mathcal{A},\mathcal{Z}) = \mathcal{Z}m_{\mathrm{p}}c^2 + \mathcal{N}m_{\mathrm{n}}c^2 - mc^2 \tag{1.1}$$

where c is the speed of light in vacuum, represents the energy which would be released if a nucleus were formed directly from $\mathcal{A}$ independent nucleons. If the energy balance of a nuclear reaction

$$\Delta\mathsf{E} \equiv \sum_{k\in\text{products}} \mathcal{B}(\mathcal{A}_k,\mathcal{Z}_k) - \sum_{k\in\text{reactants}} \mathcal{B}(\mathcal{A}_k,\mathcal{Z}_k) \tag{1.2}$$

is positive (i.e. if the reaction is exoenergetic), the energy can be extracted. Figure 1.2 shows that mass is converted into energy when light nuclei fuse together, just as it occurs when splitting heavy nuclei in fission.

Choice of D-T fuel

For fusion, the reactions which convert hydrogen and its isotopes, deuterium and tritium, to helium have the greatest energy gain. Some examples of fusion reactions which could potentially be used as the basis for an energy source on Earth are :

$$^2_1\mathrm{D} + {}^3_1\mathrm{T} \longrightarrow {}^4_2\mathrm{He} + \mathrm{n} \qquad \Delta\mathsf{E}_{\mathrm{DT}} = 17.6\,\mathrm{MeV} \tag{1.3}$$

$$^2_1\mathrm{D} + {}^2_1\mathrm{D} \longrightarrow {}^3_2\mathrm{He} + \mathrm{n} \qquad \Delta\mathsf{E}_{\mathrm{DDn}} = 3.3\,\mathrm{MeV} \tag{1.4}$$

$$^2_1\mathrm{D} + {}^2_1\mathrm{D} \longrightarrow {}^3_1\mathrm{T} + \mathrm{p} \qquad \Delta\mathsf{E}_{\mathrm{DDp}} = 4.0\,\mathrm{MeV} \tag{1.5}$$

$$^2_1\mathrm{D} + {}^3_2\mathrm{He} \longrightarrow {}^4_2\mathrm{He} + \mathrm{p} \qquad \Delta\mathsf{E}_{\mathrm{D^3He}} = 18.3\,\mathrm{MeV} \tag{1.6}$$

A fusion reaction takes place when reacting nuclei come into direct contact. Hence, it is necessary to reduce the distance between nuclei in the range of strong interaction, which is of the order 10^{-15} m. This process does not happen very easily because of the repelling Coulomb force, as nuclei are always positively charged. Considerable amounts of kinetic energy allow particles to overcome the repulsive Coulomb force. A simplistic model gives a temperature of

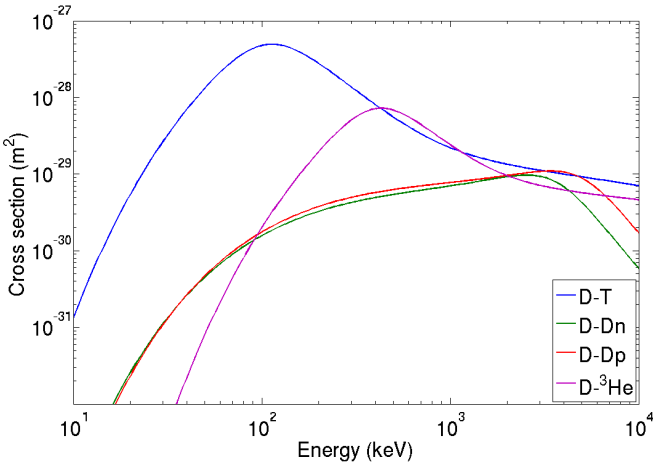

Figure 1.3: Cross sections of the fusion reactions (1.3) to (1.6) as function of energy [Huba, 2011].

the order of MeV. However, the temperature required for fusion reactions is roughly 10 keV ($\simeq 10^8$ Kelvin), thanks to interactions of quantum nature such as the tunnelling effect. This far exceeds the ionization energies of hydrogen and the lighter elements which are of the order 10 eV. This means that matter must be in a plasma state.

The relevant quantity at microscopic scales to quantify the probability of a reaction is the cross section. It represents the effective surface area for interaction. Among the possible fusion reactions on Earth, the D-T fusion reaction (1.3) has by far the largest cross section at relatively low energies (Figure 1.3). As a potential source of energy, D-T fusion is attractive since the reaction generates helium (α-particle) as by-product which is a chemically inert gas with no threat to the environment. Also, deuterium is naturally abundant in nature. It is known that a cubic meter of sea-water contains more than 30 g of deuterium. However, tritium is extremely rare in nature and radioactive with a half-life time of approximatively 12.5 years. It can be produced by neutron bombardment of lithium, which is abundant on Earth, via the reactions

$$^6_3\mathrm{Li} + \mathrm{n} \longrightarrow {}^4_2\mathrm{He} + {}^3_1\mathrm{T} \qquad \Delta E = 4.8\,\mathrm{MeV} \tag{1.7}$$

$$^7_3\mathrm{Li} + \mathrm{n} \longrightarrow {}^4_2\mathrm{He} + {}^3_1\mathrm{T} + \mathrm{n} \qquad \Delta E = -2.5\,\mathrm{MeV} \tag{1.8}$$

Therefore, it is planned to produce tritium *in situ* from lithium covering around the vacuum vessel and neutrons from the D-T reaction. However, the breeding reaction is endoenergetic with the common isotope of lithium $^7_3$Li, of which the abundance is 92.5% compared to 7.5% of $^6_3$Li. Still, $^7_3$Li can be used with beryllium which has a role of neutron multiplier. In addition, recent studies show that a lithium wall in a fusion device improves plasma confinement [Krasheninnikov et al., 2003][Kugel et al., 2008]. In terms of fuel abundance, there is enough deuterium and lithium on Earth to provide energy by fusion for several thousands of years [Cowley, 2016].

Confinement methods

Energy losses (e.g. due to radiation, escaping particles, ...) must be balanced by depositing the produced energy back into the plasma. The α-particle formed by the D-T reaction carries away 3.5 MeV, which is 20% of the energy generated. Helium heats the plasma by redistributing its energy through collisions with cooler particles. The rest of the energy cannot be recovered for the fusion reaction as plasmas are transparent to neutrons. Instead, neutrons are slowed down in the blanket where their kinetic energy is transformed into heat energy and collected by the water coolant. In a fusion power plant, this energy will be used for electrical power production. Ideally, the fusion reactions must be self-sustained thanks to the plasma heating by α-particles. This state is called ignition. In practice, a ratio of the fusion and injected power of about 30 is considered as sufficient for a reactor.

The quality of the confinement is quantified by the confinement time τ_E which measures the characteristic plasma energy decay time. It is defined as a ratio between the thermal energy content $\mathcal{W}_{\text{th}}$ and the power loss $\mathcal{P}_{\text{loss}}$

$$\tau_E \equiv \frac{\mathcal{W}_{\text{th}}}{\mathcal{P}_{\text{loss}}} \tag{1.9}$$

For D-T fuel, the condition for ignition is summarized in the Lawson criterion [Lawson, 1957][Wesson, 2011]

$$NT\tau_E \gtrsim 3 \times 10^{21}\,\text{keV.m}^{-3}\text{.s} \tag{1.10}$$

where N is the particle density of the D-T fuel, T is the plasma ion temperature and τ_E is the energy confinement time. The confinement time is defined as the ratio of stored energy in plasma to the power loss. The product $NT\tau_E$ is called 'triple product'. This condition on the triple product gives three possibilities to trigger thermonuclear fusion reactions.

- Gravitational confinement has been the most natural confinement method since the existence of the universe. Stars give good examples of gravitationally confined thermonuclear reactors. Conditions in the cores are such that all three parameters N, T and τ_E have sufficient values to satisfy the ignition criteria. Meanwhile, the first step of the chain reaction in the Sun involves protons. Two protons fuse to form ${}^{2}_{2}\text{He}$ (or diproton), which then becomes ${}^{2}_{1}\text{D}$ through a beta-plus decay. This first step has an extremely low cross section because one of the proton beta-plus decays into a neutron through weak interaction, and so is extremely slow. Otherwise, the Sun would have burnt its hydrogen much too fast. Some of the stars are even hot and dense enough to fuse elements much heavier than hydrogen isotopes. Nevertheless, it is impossible to perform gravitational confinement in Earth environment. Hence, other solutions are explored by a trade-off between the three parameters N, T and τ_E.

- The idea of inertial confinement to compress a fuel target containing deuterium and tritium, so that temperature and density would be sufficient to reach ignition, even if

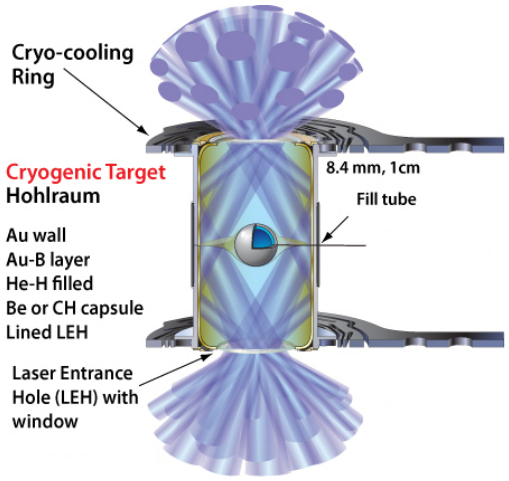

Figure 1.4: A schematic figure of a *hohlraum*[3]. The multiplied laser beams penetrate in the *hohlraum* by the Laser Entrance Hole (LEH) and hit the wall made of gold ($^{197}_{79}$Au). X-ray emission resulting from the laser interaction with $^{197}_{79}$Au wall compresses the D-T fuel capsule homogeneously.

the confinement time is very short ($\tau_E \sim 100\,\text{ps}$). The most advanced technology uses high-power lasers to try and compress the D-T target as quickly and homogeneously as possible. The main inertial fusion facilities in the world are the National Ignition Facility (USA) and the Laser Mégajoule (France) which is under construction. The main challenge of inertial confinement fusion is to compress the target homogeneously. Indeed, fluid instabilities such as the Rayleigh-Taylor instability would occur if a direct impact was made by a finite number of multiplied laser beams. The idea to bypass this difficulty is to insert the D-T fuel capsule inside a *hohlraum* (Figure 1.4). Technology on the homogeneous compression of target is related to the principle of thermonuclear bomb. Such military-level classification prevents the access to this process to most countries.

- So far, the most advanced concept for civil use is magnetic confinement. It aims at maximising the energy confinement time and plasma temperature at the expense of lower densities ($N \simeq 10^{20}\,\text{m}^{-3}$). Quasi-continuous operational use and intrinsic safety are among the advantages of the magnetic confinement. Hence, this method is currently regarded as the best prospect for near-term fusion reactors and will be detailed in Section 1.1.2.

1.1.2 Magnetic confinement

Twisted magnetic field lines

Energy and charged particles of the plasma are confined by strong magnetic fields in a magnetic confinement device. In this way, particles of mass m_a and charge e_a gyrate around

[3]Image from the website of National Ignition Facility (http://lasers.llnl.gov/)

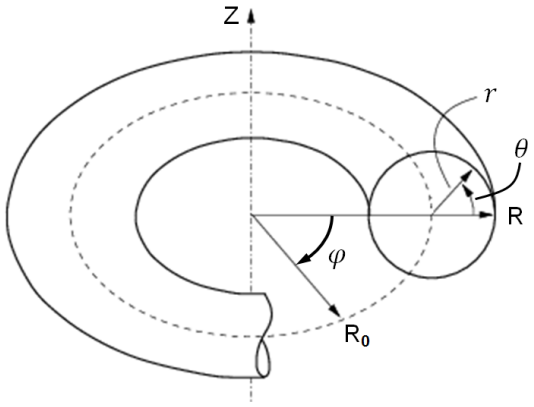

Figure 1.5: Toroidal coordinate system (r,θ,φ). The major radius of this torus is R_0.

the magnetic field line at the cyclotron pulsation $\omega_\mathsf{c} = |e_a|B/m_a$ and with a Larmor radius $\rho_\mathsf{L} = v_\perp/\omega_\mathsf{c}$, where B is the magnetic field strength, $v_\perp$ the velocity transverse to the magnetic field.

The simplest magnetic configuration is a solenoid. Magnetic coils around a long cylinder produce a magnetic field parallel to the cylinder axis. Such a magnetic configuration prevents ions and electrons from being lost radially, but not from being lost at the ends of the solenoid. One solution to this problem is to use magnetic mirrors at the ends of the cylinder, in order to trap particles inside the linear device. In the past, this solution has never been demonstrated to be effective enough. The other way is to eliminate the ends by bending the cylinder to form a torus. In this section, we will focus on toroidal closed configurations (Figure 1.5).

A containment device with a simple toroidal magnetic field would appear to be sufficient to confine a plasma. Nonetheless, closer consideration of the particle orbits reveals that the confinement is poor in this case. In fact, the toroidal magnetic field $\mathbf{B}_t$ is proportional to the inverse of the major radius $1/\mathsf{R}$. Therefore, the Larmor radii of the particles differ as they gyrate, being always smaller in the region of higher field, i.e. towards the centre of the torus. This causes electrons and ions to drift along $\mathbf{B} \times \boldsymbol{\nabla} B$ in opposite directions. The resulting vertical charge separation then produces an electric field $\mathbf{E}$. The plasma drifts horizontally out of the torus in the horizontal $\mathbf{E} \times \mathbf{B}$ direction, so the confinement is poor [Wesson, 2011].

The effects due to drifts can be attenuated with an additional poloidal magnetic field $\mathbf{B}_p$, such that the field lines are bent helically along the plasma column. As a consequence, the $\mathbf{B} \times \boldsymbol{\nabla} B$ drift changes direction as particles move along the magnetic field lines alternately on the low and high field side. Consequently, the net drift effect is averaged to zero. The magnetic field is twisted by different ways.

- The stellarators use shaped toroidal coils so that the two necessary components of the magnetic fields are generated. Large Helical Device (LHD) in Toki (Japan) and Wendelstein-7X in Greifswald (Germany) are currently the largest stellarators.

- In tokamaks, the poloidal magnetic field is induced by a toroidal current in the range of a mega-Ampère (MA). Only tokamak configurations will be considered in this thesis.

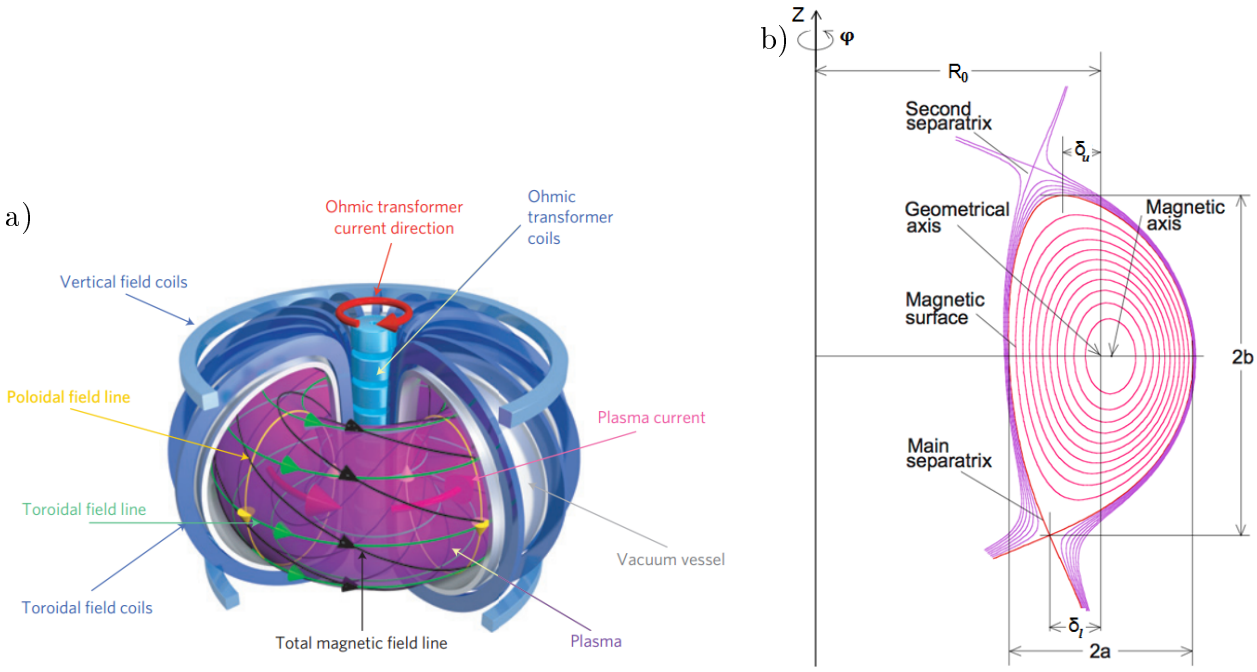

Figure 1.6: (a) A schematic view of a tokamak device[4]. (b) Geometric parameters of a plasma [Luce, 2013].

Presentation of tokamaks

Tokamaks have been the predominant research line worldwide for magnetically confined fusion. It is an axisymmetric device using helical magnetic fields to confine a plasma in a torus shaped vessel. The configuration of a tokamak is shown in Figure 1.6-a. The magenta coloured doughnut shape represents the plasma confined in the vacuum vessel. The plasma chamber is surrounded by the toroidal field coils by which the toroidal magnetic field is produced. The poloidal magnetic field is created by the plasma current generated by the central solenoid and poloidal coils. The combination of the toroidal and poloidal fields results in helical field lines. An additional field produced by an imbalance of poloidal field coils is used to control the vertical position and shape of the plasma. Recent tokamaks are equipped with superconducting coils to prevent ohmic losses.

The induced current provides a heat source to the plasma thanks to the Joule effect. This process is called ohmic heating. The ohmic heating power density is given by

$$\mathcal{P}_{\text{Ohm}} = \eta J^2 \tag{1.11}$$

where η is the plasma resistivity and J is the plasma current density. Hence, the plasma is heated when increasing the plasma current. However, the plasma current (or its density) is limited by the design of the superconducting coils. Also, the plasma resistivity is a decreasing function of the electron temperature T_e, with $\eta \propto T_e^{-3/2}$. Therefore, this method has limitations and additional means of heating must be implemented.

[4]Image from [Ongena et al., 2016]

Plasmas can be heated by injecting high-energy beams of neutral atoms into the core plasma, which is called neutral beam injection (NBI). The injected atoms are typically hydrogen isotopes. The energy of neutral particles is directly transferred to charged plasma particles by collisions. The overall plasma temperature is thus increased. Additional energy can be provided to the plasma by means of electromagnetic waves. Plasma heating by waves coupled to the resonant frequencies of the ion species and electrons are respectively called ion cyclotron resonance heating (ICRH) and electron cyclotron resonance heating (ECRH). These electromagnetic waves can also be used to drive current in the plasma. Depending on the frequency range, one talks about ion cyclotron current drive (ICCD), electron cyclotron current drive (ECCD) and lower hybrid current drive (LHCD).

Parameters of geometry and stability

A tokamak plasma is characterized by a number of quantities. Geometrical parameters are defined by the plasma inside the last closed flux surface (LCFS) as shown in Figure 1.6-b. The major radius R_0 and the minor radius a of the plasma define the aspect ratio R_0/a. In tokamaks, it can be as low as 1.5 for spherical tokamaks, e.g. MAST-Upgrade (Culham Centre for Fusion Energy) and NSTX-Upgrade (Princeton Plasma Physics Laboratory), but typical values are near 3. The ellipticity of the plasma is quantified by the plasma elongation

$$\kappa \equiv \frac{b}{a} \tag{1.12}$$

where b measures the height of the highest LCFS point. The triangularity δ is used to quantify the 'D-shape' of the plasma. It is defined as the relative position of the X-point with respect to the geometrical axis

$$\delta = \frac{\mathsf{R}_0 - \mathsf{R}_\mathsf{X}}{a} \tag{1.13}$$

with R_X the position of the X-point. In a general case, plasma is up-down asymmetric. Thus, upper triangularity δ_u and lower triangularity δ_l are separately defined as shown in Figure 1.6-b. The poloidal shape of the vacuum vessel is a strong constraint on the plasma geometry. As far as TCV (Swiss Plasma Center) is concerned, more exotic plasma shapes can be studied thanks to a very broad range of elongation and triangularity possible (e.g. [Martynov et al., 2005][Marinoni et al., 2009]).

In tokamaks, the magnetic field lines at equilibrium wind around nested toroidal surfaces, called magnetic surfaces. For a given magnetic surface, the safety factor q denotes the number of turns made in the toroidal direction for each turn in the poloidal direction. The formal definition of q is

$$q = \frac{1}{2\pi} \int \frac{\mathbf{B} \cdot \boldsymbol{\nabla}\varphi}{\mathbf{B} \cdot \boldsymbol{\nabla}\theta} \mathrm{d}\theta \tag{1.14}$$

The magnetic surface is resonant if q is a rational number, i.e. the magnetic field lines are closed back on to themselves. Then, $q = \mathsf{m}/\mathsf{n}$ for a mode with poloidal and toroidal mode numbers (m,n).

The parameter β represents the efficiency of the plasma confinement by the magnetic field. It is defined as

$$\beta = \frac{\langle P \rangle_{\mathsf{V}}}{B_0^2/2\mu_0} \tag{1.15}$$

where $\langle P \rangle_{\mathsf{V}} = \int P \mathrm{d}\mathsf{V} / \int \mathrm{d}\mathsf{V}$ is the kinetic pressure $P = NT$ averaged in plasma volume, B_0 is the magnetic field on the geometrical axis and μ_0 is the vacuum permeability. Similarly, the poloidal beta β_p is defined by normalising the kinetic pressure by the poloidal magnetic field B_p

$$\beta_p = \frac{\langle P \rangle_{\mathsf{V}}}{B_p^2/2\mu_0} \tag{1.16}$$

Usually, $\beta \sim 10^{-2}$ and $\beta_p \sim 1$ in tokamaks. The values of β for practical reactor are below the *Troyon limit*, since high-n instabilities such as ballooning modes develop at high-β [Troyon et al., 1984].

1.2 Impurities in tokamak plasmas

1.2.1 Main issues related to impurities

In general, all particles other than fuels for fusion reaction are called impurities. Impurities in tokamak plasmas are inevitable. For D-T fuel, helium ashes are produced by fusion reactions. In addition, other impurities from the edge region pollute the plasma. Either they come from erosion by sputtering of material surfaces in contact with the plasma, or injected in the plasma intentionally in the form of gas puff and pellet. Especially, tokamak divertors are important sources of impurities as they are exposed to high heat fluxes. Consequently, tokamak plasmas rapidly become polluted by impurities from different sources.

The fusion reaction rate is proportional to deuterium density times tritium density. However, the presence of impurities in the core dilutes fusion reactants, and thus decreases the probability of fusion reaction. Apart from fuel dilution, the power radiated by the impurities is a major concern. Indeed, impurities produced by plasma-wall interaction are heavier than hydrogen isotopes, and will be mostly metallic in ITER. More power is radiated out as heavy ions get closer to the plasma center.

Once impurities penetrate the plasma, they get ionized because of the high temperature. Nevertheless, the ions are fully stripped only for atoms lighter than argon ($\mathcal{Z}_{\mathrm{Ar}} = 18$) in the temperature range of typical tokamak plasmas. Heavier impurities, e.g. tungsten ($\mathcal{Z}_{\mathrm{W}} = 74$), are present in partially stripped states. Non-fully stripped ions radiate very significant amounts of power with line emission and radiative recombination. Even fully stripped ions radiate more than hydrogen isotopes through *bremsstrahlung* which scales with the square of the charge. Different radiation mechanisms are detailed in Ref.[Vezinet, 2013].

From these properties, impurities even in very small quantities affect the confinement by cooling down the core plasma and can lead to radiative collapse [Noda et al., 1997].

For tungsten, its concentration has to be maintained below 10^{-4} [Pütterich et al., 2010]. Therefore, impurity transport in the core plasma is an important matter of concern for fusion performance.

1.2.2 Effects of magnetohydrodynamic instabilities on impurities

A plasma can be described as a fluid of charged particles immersed in magnetic fields. This magnetized fluid is the framework of magnetohydrodynamics (MHD). Numerous plasma parameters such as current, pressure gradient or beta can trigger MHD instabilities which degrade the plasma performance and limit the operational domain. They appear at resonant magnetic surfaces where values of q are rational. In the core region, sawteeth and neoclassical tearing modes (NTMs) associated with low mode numbers (m,n) appear.

Sawtooth oscillations

Sawteeth are relaxation oscillations of the core temperature and density profiles [Yamada et al., 1994][Sabot et al., 2006]. They are triggered by the internal kink mode with $(\mathsf{m}, \mathsf{n}) = (1, 1)$. A sawtooth period is characterized by two main phases : the 'ramp' phase and the 'collapse' phase. Looking at the temperature profile, the ramp phase is characterized by a steady rise of the core temperature, followed by a collapse phase, so-called crash, where a sudden drop and a flattening of the temperature occur in the core (Figure 1.7). The amplitude of the drop on core temperature can reach more than 1 keV. The sawtooth crash time is usually of the order $\tau_{crash} \sim 100\,\mu$s [Edwards et al., 1986][Yamada et al., 1994]. It is very short compared to the sawtooth period ranging between 20 ms and 500 ms depending on tokamak experiments [Hastie, 1998]. Hence, the fusion reaction rate is expected to decrease significantly at each crash.

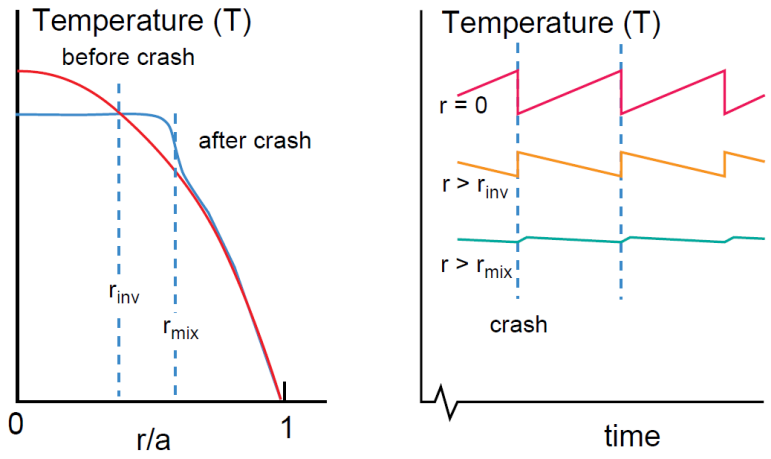

Figure 1.7: Schematic representation of sawtooth oscillations[5].

[5]Image from [ITER Physics Expert Group on Disruptions, Plasma Control, and MHD and ITER Physics Basis Editors, 1999]

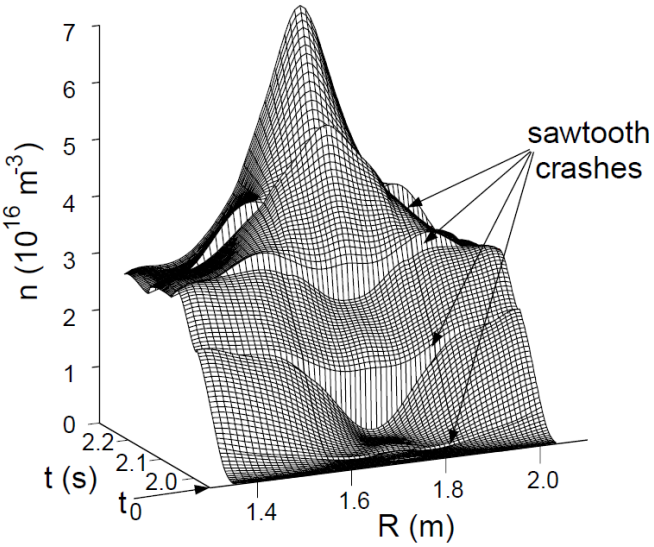

Figure 1.8: Evolution of Argon injected at time $t = t_0$ in presence of sawteeth [Dux et al., 1999]. The density evolution of Ar in the midplane is shown versus major radius R. The magnetic axis is at $R_0 = 1.72\,m$.

The sawtooth mechanism involves magnetic reconnection at the $q = 1$ resonant surface which takes place on a time much smaller than the current resistive time scale. The first reconnection model for sawteeth was proposed by Kadomtsev [Kadomtsev, 1975], based on the works of Sweet [Sweet, 1958] and Parker [Parker, 1957]. However, this reconnection model predicts a reconnection time : $\tau_{rec} \sim \sqrt{\tau_A \tau_R}$, where τ_A and τ_R are the Alfvén and resistive times respectively, which is much larger than the sawtooth crash time measured in tokamaks. Progress in theory [Rosenbluth et al., 1973][Waelbroeck, 1989][Wesson, 1990][Wang and Bhattacharjee, 1993][Zakharov et al., 1993][Rogers and Zakharov, 1995][Porcelli et al., 1996] and numerical studies [Aydemir, 1992][Biskamp and Drake, 1994][Lütjens et al., 2009][Halpern et al., 2011a][Sugiyama, 2014] accounting for non-linear effects have been made to improve the description of the reconnection process. Still, the reconnection time found in simulations differs from measurements.

During sawtooth crashes, particles and energy are rapidly redistributed in the core region. Regarding impurities, it results in a very effective radial transport in the core region during sawtooth crashes. Figure 1.8 from Ref.[Dux et al., 1999] summarizes the impurity behaviour in an ASDEX-Upgrade experiment. A short argon gas puff was injected at time $t = t_0$, and the Ar density profile is then hollow. It can be seen that the impurity penetration is accelerated during sawtooth crashes. However, as soon as the impurity profile becomes peaked, impurities are flushed out of the core region by the sawtooth crashes. The prediction based on the Kadomtsev reconnection model [Ödblom et al., 1996] is qualitatively in agreement with this observation. This process is beneficial, for example, to remove helium ashes produced in the core region and impurities pushed inward by neoclassical transport (see Chapter 5). At the same time, it also allows impurities to penetrate in core plasmas and induce the deleterious effects discussed earlier.

A more advanced impurity transport model is necessary to understand the impurity dynamics during the crash and to explore methods to control the impurity content in the core. This thesis is focused mainly on the impurity behaviour during sawtooth cycles.

Neoclassical tearing modes (NTMs)

Usually, neoclassical tearing modes (NTMs) in core plasmas are associated with $(m, n) = (3, 2)$ or $(2, 1)$ tearing modes. It is often observed that NTMs are seeded by sawtooth crashes [Sauter et al., 2002a][Buttery et al., 2004][Chapman et al., 2010]. These modes cause a reorganization of the magnetic field configuration via the formation of magnetic islands at the corresponding resonant surfaces. Figure 1.9 shows a schematic representation of a chain of magnetic islands. Particles trapped in magnetic islands spans freely the secondary magnetic surfaces. Radial transport is effectively short-circuited across the islands so that the plasma pressure becomes flat inside the island. As a consequence, plasma energy globally decreases and the bootstrap current is reduced. The resulting current hole near the island O-point is destabilizing. Furthermore, an overlap of neighbouring island chains causes the magnetic field lines to become stochastic. This inevitably results in a loss of plasma confinement. The aim of NTM theory consists in predicting the non-linear saturated state of islands. It has been developed to a considerable level of sophistication [Sauter et al., 2002b][Brennan et al., 2005][Popov, 2006][Maget et al., 2014], although discrepancies with experimental observations remain [Rosenberg et al., 2002][Lütjens and Luciani, 2005].

A formation of magnetic islands in the core region also affects impurity transport. Indeed, it was shown that the impurity transport is enhanced inside the islands [Hender et al., 2016]. Thus, accumulation of impurities is accelerated by the presence of NTMs compared to predictions with turbulent and neoclassical models.

1.2.3 Electromagnetic wave injection for impurity control

It has been shown that some heating schemes using radio-frequency (RF) waves are efficient to control impurity accumulation thanks to turbulent effects [Sugai, 1982][Rice et al.,

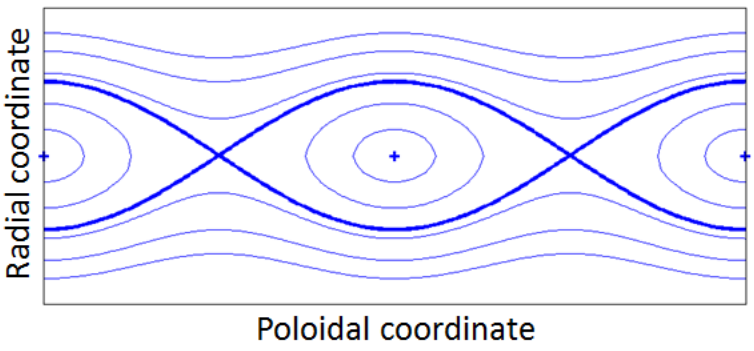

Figure 1.9: Schematic representation of magnetic islands. Each line represents a particle orbit. The separatrix are shown in bold lines and O-points are marked by '+'.

2002][Dux et al., 2003][Carraro et al., 2004][Angioni and Peeters, 2006][Leigheb et al., 2007]. However, the presence of MHD instabilities make impurity transport properties more complex. Thus, a direct control of sawteeth and NTMs could prevent impurity influx by reducing transport processes due to MHD instabilities.

Sawteeth can be avoided in hybrid scenarios, but mostly exist in tokamak plasmas. The sawtooth instability can be controlled by modifying its period between crashes using electromagnetic wave injection. Indeed, fast ions driven by ICRH are shown to stabilize sawteeth [Graves, 2005][Chapman, 2011][Graves et al., 2011][Chapman et al., 2011]. Also, both ECRH [Pietrzyk et al., 1999][Angioni et al., 2003] and ECCD [Mück et al., 2005][Lennholm et al., 2009][Chapman et al., 2012] are good means to control sawteeth. In particular, a change of sawtooth dynamics is observed when ECRH is deposited in the core region [Furno et al., 2001][Yun et al., 2012]. These observations may lead to methods for real time control of the sawtooth period and the crash amplitude for ITER [Kim et al., 2014]. Magnetic islands associated with NTMs can be reduced in size or suppressed by using localised RF waves at electron cyclotron resonant frequencies (ECRF) [Gantenbein et al., 2000][Sauter et al., 2010][Février et al., 2016]. A real-time control of NTMs with EC waves would improve confinement and avoid impurity accumulation [Felici et al., 2012].

As a consequence, the interplay between impurity accumulation, radiation and MHD instabilities needs to be understood to design optimum scenarios for impurity control.

1.3 Motivation

Deuterium-Tritium fusion offers a promising alternative to fossil fuels, to produce electricity in large amounts. However, numerous unresolved issues still have to be addressed and solved in the following decades so that dream becomes reality. Among those, understanding impurity transport in fusion plasmas is a subject of utmost importance. Indeed, impurities in the core region degrade fusion performances due to dilution and radiative cooling. Particularly, heavy impurities produced by plasma-wall interaction radiate a significant amount of power when they penetrate in the core region. In fact, even a small concentration of a metallic impurity may lead to a radiative collapse of the plasma.

Impurity transport results from a competition between different mechanisms : MHD instabilities, collisional and turbulent transport. A complex impurity behaviour is observed in sawtoothing discharges. So far, impurity transport has been mostly studied with neoclassical and turbulent transport codes, which do not take into account MHD instabilities. Indeed, a sudden radial transport is known to occur during sawtooth crashes, which affects significantly the impurity transport dynamics. It appears that transport codes are not able to reproduce the impurity dynamics observed in sawtoothing plasmas. Therefore, it is necessary to develop a predictive model including the combined effects of transport and MHD instabilities. Such a tool should allow the investigation of underlying physical processes, and could be used to devise efficient methods to control impurity accumulation.

1.4 Outline of the thesis

The tools necessary to study sawtooth cycles are presented in Chapter 2. The different sets of MHD equations used to study numerically sawteeth are derived from kinetic theory. The principles of the internal kink mode stability and magnetic field reconnection during sawtooth crashes are briefly presented. The basic numerical tools used in this work are the equilibrium code CHEASE and the non-linear MHD XTOR-2F code. Details on the numerical aspects of the XTOR-2F code are presented at the end of the chapter.

As a preparation for modelling experimental discharges, a scan of rescaled plasma parameters is made in order to simulate sawtoothing bulk plasmas in an elongated geometry with the XTOR-2F code. It turns out that several simulations exhibit features that bear similarities with compound sawteeth reported in experiments. Thus, a detailed analysis of simulated compound sawteeth is made and presented in Chapter 3. XTOR-2F simulations show that, in some situations, the plasma hot core is radially displaced and rotates, but is not fully expelled out of the $q = 1$ surface. The behaviour of this so-called partial crash is consistent with experimental observations. A scan of the $q = 1$ radius shows that partial crashes occur when it exceeds a critical value, at fixed poloidal beta β_p. This critical value depends on the plasma elongation, which is the other control parameter in this work. It can be noticed that the partial crash time is larger than the collapse time of an ordinary sawtooth, likely due to a weaker diamagnetic stabilization. This suggests that partial crashes result from a competition between destabilizing effects such as the $q = 1$ radius and diamagnetic stabilization.

In this thesis, we will refer to experimental observations in ASDEX-Upgrade tokamak, where numerical modelling using the XTOR-2F code was requested for a better understanding of the physics at stake. The behaviour of tungsten in presence of sawteeth observed in ASDEX-Upgrade tokamak discharges is presented in Chapter 4. The soft X-ray (SXR) diagnostic is the main tool used to trace heavy impurities in core plasmas. First, the principle of SXR diagnostic and tomography is presented. Second, several ASDEX-Upgrade discharges are analysed. The objective of these discharges is to study the effects of core deposition of EC waves on the control of tungsten accumulation in presence of sawteeth. It is observed that the impurity behaviour differs from predictions made by transport codes. A numerical tool which models MHD instabilities and includes appropriate impurity transport model is necessary to investigate and understand experimental observations.

The effects of sawteeth on impurity transport are studied in Chapter 5. Basic aspects of transport processes in tokamak plasmas are presented. Then, appropriate fluid equations are derived for impurities in the high collisional (Pfirsch-Schlüter) regime. These equations are implemented in the XTOR-2F code and coupled with the two-fluid MHD equations modelling bulk plasmas. The coupling of equations led to an improvement of the preconditioning matrix, which is a numerical upgrade made in the XTOR-2F code. In the following simulations, impurities are considered as tracers in order to neglect their feedback on bulk plasmas.

XTOR-2F simulations including fluid equations, without MHD instabilities, are consistent with the prediction of the neoclassical theory. Then, it is shown that the presence of regular sawtooth crashes affects the impurity behaviour. First, the temperature screening effect gets weaker in presence of sawteeth, compared to the case without sawteeth. Second, a spatial non-uniformity of 5% in post-crash impurity density profiles persists due to 2-D structures of impurity density which appear during sawtooth crashes. They are shown to be mainly driven by the $\mathbf{E} \times \mathbf{B}$ velocity, and are responsible for the sudden impurity transport in the core plasmas. Finally, sawtooth cycles with a saturated helical state are simulated with the XTOR-2F code by adding an ECCD source. These simulations are reminiscent of ASDEX-Upgrade scenarios. The results show that the presence of longer precursor oscillations keeps the impurity density profile flatter than what it was expected for ordinary sawtooth cycles.

CHAPTER 2

Sawtooth oscillations in the core region

Contents

2.1 Experimental observations

Sawteeth are relaxation oscillations in tokamak core plasmas. In experiments, sawtooth oscillations have first been reported using Soft X-ray (SXR) diagnostics [von Goeler et al., 1974], and can also be observed with other techniques like Electron Cyclotron Emission (ECE) [Yamada et al., 1994] or Fast-Sweep Reflectometry (FSR) measurements [Sabot et al., 2006]. As it can be seen in Figure 2.1, a period of sawteeth is characterized by two main phases : the 'ramp' phase and the 'collapse' phase. The ramp phase is marked by a steady rise of the core temperature and density, followed by a collapse phase where a sudden drop and flattening occur in the core [Yamada et al., 1994]. The sawtooth crash time τ_{crash} is usually of the order of a few tens of microseconds [Edwards et al., 1986] depending on tokamak experiments. During this short time compared to the sawtooth periods, ranging from few tens to several hundreds of ms depending on tokamak experiments [Hastie, 1998],

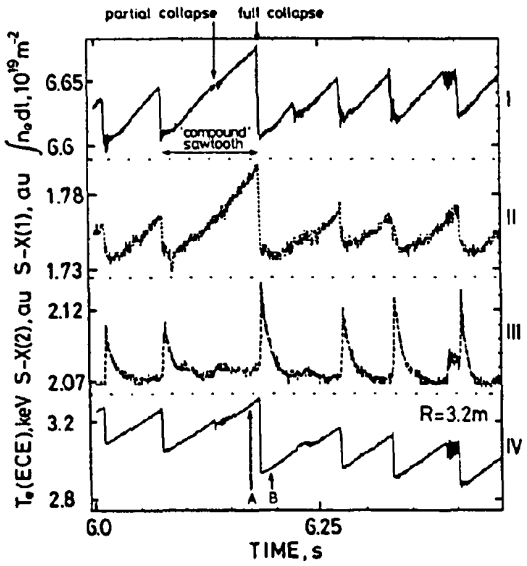

Figure 2.1: Sawtooth oscillations in JET observed by density interferometry, SXR and ECE measurements[1]. Relaxation with smaller amplitude can be noticed between two sawtooth crashes, which defines a 'compound sawtooth'.

energy, particles and impurities are rapidly redistributed in the core region [Wesson et al., 1997]. Also, oscillations of the central temperature are sometimes observed before and after the sawtooth crash [Campbell et al., 1986]. These are called 'precursor' and 'post-cursor' oscillations respectively.

More exotic shapes of sawtooth exist and are frequently observed in experiments.

- A drop of central temperature during the sawtooth ramp phase is frequently observed (Figure 2.1). This drop has a smaller amplitude than the 'ordinary' collapse, and does not terminate the ramp phase. It is referred to as a 'partial collapse'. The onset of these so-called 'compound sawteeth' is discussed in Chapter 3.

- In cases where the ECRF deposition is near the $q = 1$ surface, it is observed that the sawtooth period increases [Angioni et al., 2003]. At the same time, a change of the sawtooth shape has been revealed. Indeed, during the ramp phase, the hot core remains radially displaced and rotates in the poloidal direction. This is called 'hump-back' sawtooth [Furno et al., 2001]. Moreover, it has been observed in some cases that the hot core could split into multiple helical flux tubes [Yun et al., 2012].

- 'Monster' sawteeth have a period much larger than the confinement time and a larger crash amplitude than 'ordinary' sawteeth. They are characterized by a quasi-stationary phase between the sawtooth ramp and crash. They are produced when the ICRH deposition layer is located inside the $q = 1$ surface [Bhatnagar et al., 1989] provided a sufficient power is injected [Chapman et al., 2013]. It has been reported that their large amplitude collapse is more likely to trigger NTMs [Buttery et al., 2004][Maget et al., 2005][Chapman et al., 2010].

[1] Image from [Campbell et al., 1986]

The previous list is of course not complete. The physics of sawtooth is so vast that there are still unanswered open questions, mainly concerning the fast reconnection time. Studying sawtooth physics allows one to investigate magnetic reconnection on a laboratory scale. It is also important for efficient tokamak operation as sawteeth regularly flatten the temperature and redistribute particles in the core region, which affects plasma confinement.

2.2 Magnetohydrodynamics

2.2.1 Magnetic configuration at equilibrium

Magnetic flux surfaces

In cylindrical coordinates (R,φ,Z) the magnetic field $\mathbf{B}$ can be written as

$$\mathbf{B} = B_{\mathsf{R}}\hat{\mathbf{e}}_{\mathsf{R}} + B_{\varphi}\hat{\mathbf{e}}_{\varphi} + B_{\mathsf{Z}}\hat{\mathbf{e}}_{\mathsf{Z}} = \boldsymbol{\nabla} \times \mathbf{A} \tag{2.1}$$

where $\mathbf{A}$ is the vector potential. Here, the unit vectors are such that $\hat{\mathbf{e}}_{\varphi} = \hat{\mathbf{e}}_{\mathsf{R}} \times \hat{\mathbf{e}}_{\mathsf{Z}}$, as shown in Figure 1.5. If we consider an axisymmetric magnetic field, all derivatives with respect to the toroidal angle φ vanish, i.e. $\partial_{\varphi} = 0$. Thus, the poloidal component of the magnetic field $\mathbf{B}_p = B_{\mathsf{R}}\hat{\mathbf{e}}_{\mathsf{R}} + B_{\mathsf{Z}}\hat{\mathbf{e}}_{\mathsf{Z}}$ is

$$\mathbf{B}_p = \frac{\partial A_{\varphi}}{\partial \mathsf{Z}}\hat{\mathbf{e}}_{\mathsf{R}} - \frac{1}{\mathsf{R}}\frac{\partial(\mathsf{R}A_{\varphi})}{\partial \mathsf{R}}\hat{\mathbf{e}}_{\mathsf{Z}} = \boldsymbol{\nabla}\varphi \times \boldsymbol{\nabla}\psi \tag{2.2}$$

where ψ is the poloidal flux function defined as

$$\psi(\mathsf{R}, \mathsf{Z}) \equiv -\mathsf{R}A_{\varphi}(\mathsf{R}, \mathsf{Z}) \tag{2.3}$$

As a consequence, the magnetic field $\mathbf{B}$ is written in the form

$$\mathbf{B} = I(\psi)\boldsymbol{\nabla}\varphi + \boldsymbol{\nabla}\varphi \times \boldsymbol{\nabla}\psi \tag{2.4}$$

as $\mathsf{R}\boldsymbol{\nabla}\varphi = \hat{\mathbf{e}}_{\varphi}$. The toroidal component $I(\psi)$ represents also the poloidal current flux function.

It is clear that $\mathbf{B} \cdot \boldsymbol{\nabla}\psi = 0$, hence ψ is constant along magnetic field lines. The magnetic field vector $\mathbf{B}$ lies on surfaces of constant ψ, called magnetic flux surfaces. In tokamaks, these flux surfaces have a form of nested tori at equilibrium.

The Grad-Shafranov equation

In tokamaks, the magnetic field is set up such that the pressure force is balanced at stationary phase, in order for the plasma to be well confined. Thus the basic equilibrium force balance is

$$\mathbf{J} \times \mathbf{B} = \boldsymbol{\nabla}P \tag{2.5}$$

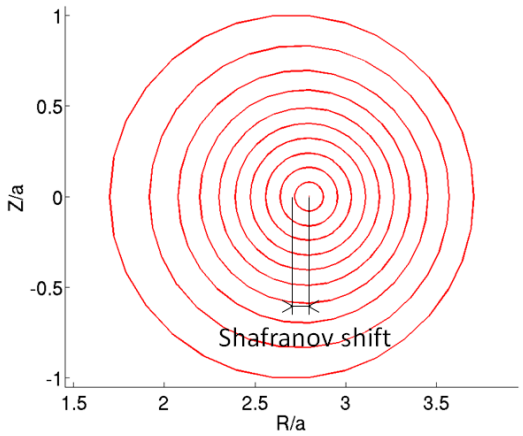

Figure 2.2: Magnetic flux surfaces of a circular equilibrium computed by the CHEASE code. It can be seen that the magnetic axis is shifted to the LFS with respect to the geometric axis.

where $\mathbf{J} = \sum_a N_a e_a \mathbf{V}_a$ is the total current density and $P = \sum_a N_a T_a$ is the total plasma pressure. Consequently,

$$\mathbf{B} \cdot \boldsymbol{\nabla} P = 0 \tag{2.6}$$

and the pressure is constant on flux surfaces, i.e. $P = P(\psi)$.

Since P and I are functions of ψ, the force balance equation (2.5) can be rewritten as

$$\mathsf{R}^2 \boldsymbol{\nabla} \cdot \left(\frac{\boldsymbol{\nabla}\psi}{\mathsf{R}^2} \right) = -\mu_0 \mathsf{R} J_\varphi = -\mu_0 \mathsf{R}^2 P' - II' \tag{2.7}$$

which is called the Grad-Shafranov equation. Knowing the pressure gradient P' and II', the numerical solution for ψ gives the magnetic configuration at equilibrium. The CHEASE code [Lütjens et al., 1996] is used to solve the Grad-Shafranov equation in this thesis. Figure 2.2 shows magnetic surfaces computed for a circular poloidal cross-section.

The magnetic axis is shifted towards large R values with respect to the geometric center of the poloidal cross-section. This is called the Shafranov shift, and it is due to the toroidal geometry of the configuration.

2.2.2 From kinetic to fluid description of plasmas

The kinetic equation

A plasma is a mixture of charged particles (electrons and different ion species), each of them characterized by its position $\mathbf{x}$ and velocity $\mathbf{v}$. Thus each particle can be represented as a point in 6-D phase space ($\mathbf{x}$,$\mathbf{v}$). The distribution function $F_a(\mathbf{x}, \mathbf{v}, t)$ of a species a is defined as the number of particles per unit volume in phase space near the point ($\mathbf{x}$,$\mathbf{v}$) at the time t. Hence, the integration of F_a over the velocity space gives the particle density N_a in real space

$$\int F_a(\mathbf{x}, \mathbf{v}, t) \mathrm{d}^3 v = N_a(\mathbf{x}, t) \tag{2.8}$$

From the conservation equation of the distribution function, the Vlasov equation is deduced

$$\partial_t F_a + \frac{\mathrm{d}\mathbf{x}}{\mathrm{d}t} \cdot \boldsymbol{\nabla}_{\mathbf{x}} F_a + \frac{\mathrm{d}\mathbf{v}}{\mathrm{d}t} \cdot \boldsymbol{\nabla}_{\mathbf{v}} F_a = 0 \tag{2.9}$$

Each particle with charge e_a experiences the electromagnetic force $e_a(\mathbf{E} + \mathbf{v} \times \mathbf{B})$, where $\mathbf{E}$ and $\mathbf{B}$ are the electric and magnetic fields respectively. Thus, the Vlasov equation can be written as

$$\partial_t F_a + \mathbf{v} \cdot \boldsymbol{\nabla} F_a + \frac{e_a}{m_a}(\mathbf{E} + \mathbf{v} \times \mathbf{B}) \cdot \boldsymbol{\nabla}_{\mathbf{v}} F_a = 0 \tag{2.10}$$

The effects of collisions which occur at length scales comparable to the Debye length, are regrouped into the collision operator $\mathcal{C}_a$. Consequently, the kinetic equation in presence of short-range electromagnetic fluctuations reads

$$\partial_t F_a + \mathbf{v} \cdot \boldsymbol{\nabla} F_a + \frac{e_a}{m_a}(\mathbf{E} + \mathbf{v} \times \mathbf{B}) \cdot \boldsymbol{\nabla}_{\mathbf{v}} F_a = \mathcal{C}_a(F_a) \tag{2.11}$$

The evolution of the electric field $\mathbf{E}$ and magnetic field $\mathbf{B}$ is described by the Maxwell equations :

$$\boldsymbol{\nabla} \cdot \mathbf{B} = 0 \qquad \boldsymbol{\nabla} \cdot \mathbf{E} = \frac{\sigma}{\varepsilon_0}$$

$$\partial_t \mathbf{B} + \boldsymbol{\nabla} \times \mathbf{E} = 0 \qquad \boldsymbol{\nabla} \times \mathbf{B} = \frac{1}{c^2}\partial_t \mathbf{E} + \mu_0 \mathbf{J}$$

where ε_0, μ_0 and c are respectively the permittivity, the permeability and the speed of light in vacuum, σ is the charge density.

Solving these coupled equations is very challenging and requires important numerical resources. It is usually done to study small-scale phenomena like plasma turbulence.

Fluid equations

Phenomena such as MHD instabilities have larger space and time scales than those of gyro-motion. In other words, $\rho^* = \rho_{\mathsf{L}}/L \ll 1$ and $\omega/\omega_c \ll 1$ where L and ω^{-1} represent the characteristic length and time scales of MHD instabilities. Also, the fluid closure is valid if Landau resonances are avoided. Indeed, kinetic effects have to be considered at Landau resonances as energy can be transferred between particles and MHD waves. For a MHD mode with wave vector $\mathbf{k}$, the condition to avoid Landau resonances is written $\omega \gg \mathbf{k} \cdot \mathbf{v}$ [Belmont et al., 2013]. In this case, a reduction of the system into 3-D real space is sufficient to describe the macroscopic behaviour of the plasma. Therefore, the distribution function F_a remains Maxwellian, i.e. there are no particular velocities or regions of the velocity space where the charged particles behave differently from the typical thermal particles of that species. The framework of a fluid description of the plasma is known as the magnetohydrodynamics (MHD).

The density N_a, macroscopic fluid velocity $\mathbf{V}_a$ and pressure tensor $\bar{\bar{\mathbf{P}}}_a$ are deduced by

taking moments of the distribution function F_a

$$N_a = \int F_a \mathrm{d}^3 v \tag{2.12}$$

$$N_a \mathbf{V}_a = \int \mathbf{v} F_a \mathrm{d}^3 v \tag{2.13}$$

$$\bar{\bar{\mathbf{P}}}_a = m_a \int \mathbf{v}' \mathbf{v}' F_a \mathrm{d}^3 v \tag{2.14}$$

Here, $\mathbf{v}' \equiv \mathbf{v} - \mathbf{V}_a$ is the difference between the velocity $\mathbf{v}$ of a given particle and the fluid velocity $\mathbf{V}_a$ of the species a. The pressure tensor $\bar{\bar{\mathbf{P}}}_a$ is decomposed into a scalar pressure P_a and a stress tensor $\bar{\bar{\mathbf{\Pi}}}_a$, which contains the anisotropic and off-diagonal terms of the pressure tensor.

$$\bar{\bar{\mathbf{P}}}_a = P_a \mathbf{1} + \bar{\bar{\mathbf{\Pi}}}_a \tag{2.15}$$

The moments of the Vlasov equation (2.10) yield the continuity equation

$$\partial_t N_a + \boldsymbol{\nabla} \cdot (N_a \mathbf{V}_a) = 0 \tag{2.16}$$

the force balance (or momentum) equation

$$m_a N_a \left[\partial_t \mathbf{V}_a + (\mathbf{V}_a \cdot \boldsymbol{\nabla}) \mathbf{V}_a\right] = N_a e_a \left(\mathbf{E} + \mathbf{V}_a \times \mathbf{B}\right) - \boldsymbol{\nabla} P_a - \boldsymbol{\nabla} \cdot \bar{\bar{\mathbf{\Pi}}}_a \tag{2.17}$$

and the pressure equation

$$\partial_t P_a + \mathbf{V}_a \cdot \boldsymbol{\nabla} P_a + \gamma P_a \boldsymbol{\nabla} \cdot \mathbf{V}_a + (\gamma - 1) \left[\boldsymbol{\nabla} \cdot \mathbf{Q}_a + \bar{\bar{\mathbf{\Pi}}}_a : \boldsymbol{\nabla} \mathbf{V}_a\right] = 0 \tag{2.18}$$

where γ is the adiabatic index, the notation $\bar{\bar{\mathbf{\Pi}}} : \boldsymbol{\nabla} \mathbf{V} \equiv \Pi_{ij} \partial_j V_i$ and $\mathbf{Q}_a$ is the microscopic heat flux defined by

$$\mathbf{Q}_a = \int \frac{m_a v'^2}{2} \mathbf{v}' F_a \mathrm{d}^3 v \tag{2.19}$$

2.2.3 MHD equations

Orderings

The fluid velocity $\mathbf{V}_a$ of a species a can be decomposed into components parallel and perpendicular to the magnetic field.

$$\mathbf{V}_a = \mathbf{V}_{\parallel,a} + \mathbf{V}_{\perp,a} \tag{2.20}$$

The momentum equation (2.17) gives the following decomposition of the perpendicular velocity

$$\mathbf{V}_{\perp,a} = \mathbf{V}_E + \mathbf{V}_a^* + \frac{\mathbf{B} \times \boldsymbol{\nabla} \cdot \bar{\bar{\mathbf{\Pi}}}_a}{N_a e_a B^2} + \frac{\mathbf{B} \times m_a N_a \left[\partial_t \mathbf{V}_a + (\mathbf{V}_a \cdot \boldsymbol{\nabla}) \mathbf{V}_a\right]}{N_a e_a B^2} \tag{2.21}$$

where

$$\mathbf{V}_E = \frac{\mathbf{E} \times \mathbf{B}}{B^2} \tag{2.22}$$

is the electric drift and

$$\mathbf{V}_a^* = \frac{\mathbf{B} \times \boldsymbol{\nabla} P_a}{N_a e_a B^2} \tag{2.23}$$

is the diamagnetic velocity.

The MHD theory assumes a large perpendicular electric field, i.e. $V_E/V_T \sim 1$, where V_T is the thermal velocity. It can be noticed that the diamagnetic velocity is small compared to the thermal velocity ($V_a^*/V_T \sim \rho^*$), and the following terms of the expression (2.21) are of a higher order in ρ^*. This implies that the only drift that we retain at the lowest order is the $\mathbf{E} \times \mathbf{B}$ drift.

Single fluid ideal model

Let us consider a plasma with electrons and bulk ions only, whose respective quantities are denoted with the indices e and i. We assume that both ions and electrons verify the continuity equation (2.16), the momentum equation (2.17) and the pressure equation (2.18). In the following, we assume quasineutrality of the plasma, i.e. the electron and ion densities are considered to be locally equal ($N = N_e = N_i$). This assumption is valid if we consider only plasma scales whose characteristic length is larger than the Debye length

$$\lambda_D = \sqrt{\frac{\varepsilon_0 T_e}{N_e e^2}} \tag{2.24}$$

If the plasma is considered as a single fluid, we can define

- The mass density $\rho_m = m_e N_e + m_i N_i \simeq m_i N_i$
- The mass flow velocity $\mathbf{V} = (m_e N_e \mathbf{V}_e + m_i N_i \mathbf{V}_i)/\rho_m \simeq \mathbf{V}_i = \mathbf{V}_{\parallel,i} + \mathbf{V}_E$
- The current density $\mathbf{J} = -Ne(\mathbf{V}_e - \mathbf{V}_i)$
- The plasma pressure $P = P_e + P_i$

Contributions of the pressure anisotropy tensor are neglected since the viscous stress effects are neglected in ideal MHD.

In this framework, the equation for the mass density (2.16) is thus

$$\partial_t \rho_m + \boldsymbol{\nabla} \cdot (\rho_m \mathbf{V}) = 0 \tag{2.25}$$

As the electron mass is very small compared to the ion mass, the electron inertia can be neglected in the momentum equation (2.17) written for the electron. This mass disparity allows us to consider incompressible heat fluxes $\boldsymbol{\nabla} \cdot \mathbf{Q}_a = 0$ for electrons and ions at the

lowest order. Hence, the sum of electron and ion momentum equations reads

$$\rho_m \partial_t \mathbf{V} = -\boldsymbol{\nabla} P + \mathbf{J} \times \mathbf{B} \tag{2.26}$$

and the sum of pressure equations (2.18) written for electron and ion gives

$$\partial_t P + \mathbf{V} \cdot \boldsymbol{\nabla} P + \gamma P \boldsymbol{\nabla} \cdot \mathbf{V} = 0 \tag{2.27}$$

Gauss' law becomes $\boldsymbol{\nabla} \cdot \mathbf{E} = 0$ as plasmas are highly polarizable and quasineutral (thus $\sigma \simeq 0$) fluids. The electric field $\mathbf{E}$ is self-consistently determined from Ohm's law

$$\mathbf{E} + \mathbf{V} \times \mathbf{B} = 0 \tag{2.28}$$

Replacing this relation in Faraday's law gives the time evolution of the magnetic field $\mathbf{B}$

$$\partial_t \mathbf{B} = \boldsymbol{\nabla} \times (\mathbf{V} \times \mathbf{B}) \tag{2.29}$$

Since the MHD theory considers the non-relativistic fluid model of a magnetized plasma, the time variation of the electric field $\mathbf{E}$ is negligible. Hence, Ampere's law becomes

$$\boldsymbol{\nabla} \times \mathbf{B} \simeq \mu_0 \mathbf{J} \tag{2.30}$$

Resistive-diffusive MHD ($\eta\chi$MHD) model

Collisions which are a fundamental aspect of the plasma dynamics are neglected in the ideal MHD model. Now, if we consider the kinetic equation with a collision operator $\mathcal{C}_a(F_a)$, the associated fluid equations for the species a read

$$\partial_t N_a + \boldsymbol{\nabla} \cdot (N_a \mathbf{V}_a) = 0 \tag{2.31}$$

$$m_a N_a \left[\partial_t \mathbf{V}_a + (\mathbf{V}_a \cdot \boldsymbol{\nabla}) \mathbf{V}_a\right] = N_a e_a \left(\mathbf{E} + \mathbf{V}_a \times \mathbf{B}\right) - \boldsymbol{\nabla} P_a - \boldsymbol{\nabla} \cdot \bar{\bar{\boldsymbol{\Pi}}}_a + \boldsymbol{\mathcal{R}}_a \tag{2.32}$$

$$\partial_t P_a + \mathbf{V}_a \cdot \boldsymbol{\nabla} P_a + \gamma P_a \boldsymbol{\nabla} \cdot \mathbf{V}_a + (\gamma - 1) \left[\boldsymbol{\nabla} \cdot \mathbf{Q}_a + \bar{\bar{\boldsymbol{\Pi}}}_a : \boldsymbol{\nabla} \mathbf{V}_a\right] = (\gamma - 1) \mathcal{H}_a \tag{2.33}$$

where $\boldsymbol{\mathcal{R}}_a$ and $\mathcal{H}_a$ are respectively the friction force and the energy exchange between the species a with other species. This framework, known as the resistive-diffusive MHD or $\eta\chi$MHD, adds dissipation in the form of resistivity, diffusion, viscosity and anisotropic heat transport.

Ohm's law then reads

$$\mathbf{E} + \mathbf{V} \times \mathbf{B} = \eta \mathbf{J} \tag{2.34}$$

where η is the plasma resistivity. Therefore, Faraday's law gives

$$\partial_t \mathbf{B} = \boldsymbol{\nabla} \times (\mathbf{V} \times \mathbf{B}) - \boldsymbol{\nabla} \cdot (\eta \mathbf{J}) \tag{2.35}$$

The pressure equation becomes

$$\partial_t P + \mathbf{V} \cdot \boldsymbol{\nabla} P + \gamma P \boldsymbol{\nabla} \cdot \mathbf{V} = -(\gamma - 1) \boldsymbol{\nabla} \cdot (\mathbf{Q}_e + \mathbf{Q}_i) \tag{2.36}$$

with

$$\mathbf{Q}_a = -\chi_{\parallel,a} N_a \boldsymbol{\nabla}_\parallel T_a - \chi_{\perp,a} N_a \boldsymbol{\nabla}_\perp T_a \tag{2.37}$$

representing the anisotropic heat transport for the species a. Details of this model can be found in Ref.[Braginskii, 1965].

Two-fluid MHD model

If we consider now a small electric field so that $V_E/V_T \sim \rho^*$, the diamagnetic velocities are taken into account. Therefore,

$$\mathbf{V}_i = \mathbf{V} + \mathbf{V}_i^* \tag{2.38}$$

$$\mathbf{V}_e = \mathbf{V} + \mathbf{V}_e^* - \frac{J_\parallel}{N_e e}\mathbf{b} \tag{2.39}$$

by writing $\mathbf{V} \equiv \mathbf{V}_{\parallel,i} + \mathbf{V}_E$.

Using this expansion, the continuity equation reads

$$\partial_t \rho_m + \boldsymbol{\nabla} \cdot (\rho_m \mathbf{V}_a) + \frac{m_i}{e_i} \boldsymbol{\Xi} \cdot \boldsymbol{\nabla} P_i = 0 \tag{2.40}$$

with $\boldsymbol{\Xi} \equiv \boldsymbol{\nabla} \times (\mathbf{B}/B^2)$.

It is shown that the several terms on the left-hand side of the momentum equation are cancelled by a part of the stress tensor [Hazeltine and Meiss, 2003]. Thus, the momentum equation reads

$$\rho_m \left[\partial_t \mathbf{V} + (\mathbf{V}.\boldsymbol{\nabla})\, \mathbf{V} + (\mathbf{V}_i^* \cdot \boldsymbol{\nabla}) \mathbf{V}_\perp\right] = \mathbf{J} \times \mathbf{B} - \boldsymbol{\nabla} P \tag{2.41}$$

In this ordering, the cross-field heat flux $\mathbf{Q}_a^\times$ has to be considered in addition to a purely diffusive heat flux $\mathbf{Q}_a$

$$\mathbf{Q}_a^\times = \frac{5}{2} P_a \frac{\mathbf{B} \times \boldsymbol{\nabla} T_a}{e_a B^2} \tag{2.42}$$

Therefore, the pressure equation becomes

$$\begin{aligned} \partial_t P + \mathbf{V} \cdot \boldsymbol{\nabla} P + \gamma P \boldsymbol{\nabla} \cdot \mathbf{V} + \frac{\gamma}{e_i} \boldsymbol{\Xi} \cdot (T \boldsymbol{\nabla} P_i + P_i \boldsymbol{\nabla} T_i + P_e \boldsymbol{\nabla} T_e) \\ = -(\gamma - 1) \boldsymbol{\nabla} \cdot (\mathbf{Q}_e + \mathbf{Q}_i) \end{aligned} \tag{2.43}$$

where $T = P/N$.

Finally, Ohm's law reads

$$\mathbf{E} + \mathbf{V} \times \mathbf{B} = \eta \mathbf{J} - \frac{\nabla_{\parallel} P_e}{N_e e} \mathbf{b} \tag{2.44}$$

A more detailed derivation of the $\eta\chi$MHD or two-fluid MHD equations, as well as a discussion on the approximation done to derive them can be found in Ref.[Nicolas, 2013].

2.3 Sawtooth oscillations

2.3.1 The internal kink mode

Sawtooth oscillations are associated with the MHD instability called internal kink mode. This mode has poloidal and toroidal mode numbers $\mathsf{m} = \mathsf{n} = 1$, which define a $q = 1$ resonant surface. The energy principle is a powerful method for testing ideal MHD stability in 3-D magnetic confinement configurations. Its derivation in toroidal geometry is discussed in e.g. [Bussac et al., 1975][Ara et al., 1978] and is summarized in [Nicolas, 2013].

Usually, $q < 1$ in the core region due to a peaked plasma current density profile. The internal kink mode is unstable when the minimum value of the safety factor q is below unity and the poloidal beta β_p is above a certain critical value $\beta_{p,c}$ in the ideal model [Bussac et al., 1975]. It has been shown that the critical value $\beta_{p,c}$ depends strongly on the plasma geometry as it affects magnetic field line bending [Coppi and Coppi, 1992][Lütjens et al., 1992][Martynov et al., 2005]. Indeed, the internal kink mode is destabilized by the plasma elongation, and stabilized by the plasma triangularity. Also, the internal kink mode stability is sensitive to the shear profile i.e. the details of the q-profile [Hastie et al., 1987][de Blank and Schep, 1991][Lütjens et al., 1992][Porcelli et al., 1996]. Particularly, the internal kink mode is destabilized when increasing the radial position of the $q = 1$ surface [Bussac et al., 1975][Turnbull and Troyon, 1989]. Indeed, Ref.[Bussac et al., 1975] shows that, for an equilibrium with a parabolic q-profile, the critical value $\beta_{p,c}$ decreases by a third, when the $q = 1$ radius is increased from $r_{q=1}/a \ll 1$ to $r_{q=1}/a \simeq 0.4$.

The growth rate of the internal kink mode depending on the MHD model (ideal, resistive or two-fluid) is well detailed in Ref.[Ara et al., 1978]. As the internal kink mode instability grows, the plasma center is helically displaced.

2.3.2 Magnetic reconnection

The displacement of the hot core leads to a compression of magnetic surfaces towards the $q = 1$ surface, forming a current sheet [Waelbroeck, 1989][Biskamp, 2005]. The piled-up magnetic flux surfaces break due to the plasma resistivity or other non-ideal effects leading to a reorganization of the magnetic topology, called 'magnetic reconnection'.

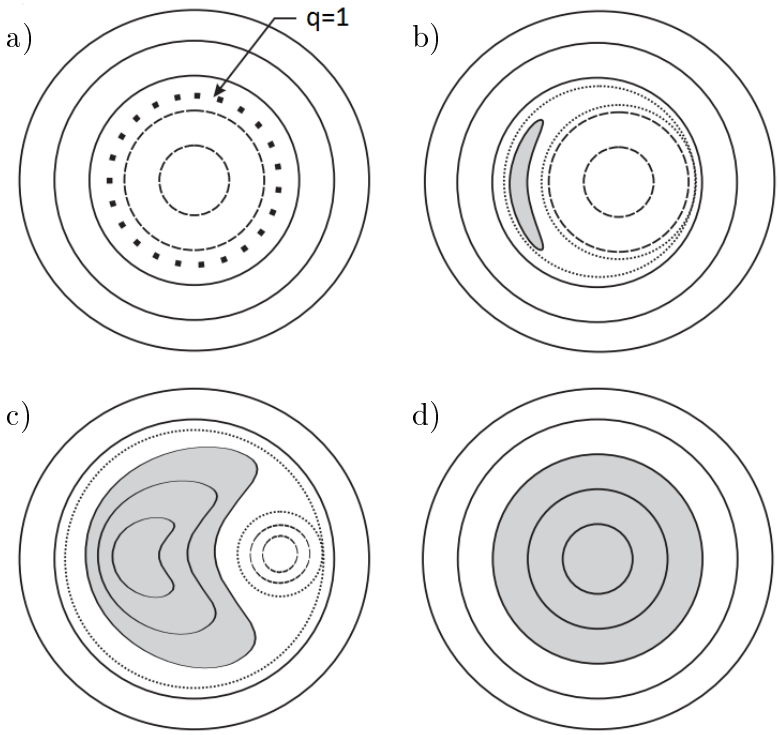

Figure 2.3: Schematic representation of the Kadomtsev reconnection model during sawtooth crash. After the collapse, the core region is replaced by a cooler island.

The first reconnection model for sawtooth crash was proposed by Kadomtsev [Kadomtsev, 1975], based on the works of Sweet [Sweet, 1958] and Parker [Parker, 1957]. It is based on helical flux conservation (for details see Refs.[Kadomtsev, 1975][Porcelli et al., 1996][Furno et al., 2001]), and predicts a complete expulsion of the hot core out of the $q = 1$ resonant surface during the sawtooth collapse (Figure 2.3). In this scheme, the core region is replaced by a cooler island formed during the magnetic reconnection process.

Indeed, the helical flux is maximum at the $q = 1$ radius, and the magnetic surfaces with the same helical flux value reconnect. Hence, magnetic reconnection during a sawtooth crash affects the plasma from the magnetic axis up to the 'mixing' radius, which is larger than the inversion radius (cf. Figure 1.7). This model is also called 'complete' reconnection model, as all the magnetic surfaces with safety factor $q < 1$ reconnect. As a consequence, the initially peaked temperature profile is flattened in the core region. Also, the q-profile becomes flat with values larger than unity in the core region when $q \leq 1$ before the reconnection. This model is qualitatively consistent with the dynamics of the hot core observed during the sawtooth relaxation.

Kadomtsev's reconnection model predicts a Sweet-Parker reconnection time which scales as $\tau_{rec} \sim \sqrt{\tau_A \tau_R}$, where τ_A and τ_R are the Alfvén and resistive times respectively [Sweet, 1958][Parker, 1957]. However, these reconnection times computed from the plasma parameters are much larger than the sawtooth crash times measured in tokamaks. Non-linear effects, such as the compressibility [Sugiyama, 2014], the electron inertia [Wesson, 1990] and two-fluid effects [Aydemir, 1992][Zakharov et al., 1993][Wang and Bhattacharjee, 1993] are shown

to accelerate the reconnection process. Still, the reconnection time found in simulations differs from measurements. Different theories on the magnetic reconnection during sawtooth crash can be found in Ref.[Biskamp, 2005].

2.4 Numerical methods

2.4.1 The XTOR-2F code

The initial equilibrium

The toroidal MHD equilibrium is computed with the CHEASE code [Lütjens et al., 1996] which solves the Grad-Shafranov equation (2.7) using a Hermite bicubic finite element discretization. The profiles of P' and II' must be provided as inputs to the code. These profiles can rather be analytical functions or read from experimental data. Different options are detailed in Ref.[Lütjens et al., 1996].

As far as the internal kink mode is concerned, it is important to determine an appropriate value of poloidal beta β_p so that the mode is ideally stable. Therefore, it is necessary to start by determining the critical value $\beta_{p,c}$ for given P' and II' profiles. This critical value is deduced from the study of the ideal linear growth rate of the $\mathsf{n} = 1$ mode by varying the initial pressure profile at a fixed current profile at equilibrium. By this, $\beta_{p,c}$ which corresponds to the marginal stability point of the internal kink mode in the ideal MHD can be deduced (Figure 3.3). For sawtooth simulations, the value of β_p is scaled such that the initial equilibrium is linearly stable in the ideal MHD and unstable in presence of the resistivity [Halpern et al., 2011a][Ahn et al., 2016a].

The CHEASE code computes the magnetic equilibrium and the corresponding toroidal metrics and mesh-grids which are used in the XTOR-2F code as inputs.

Normalization in the XTOR-2F code

The quantities in the XTOR-2F code are normalized according to the following convention. Here, B_0 and R_0 are respectively the magnetic field magnitude and the major radius at the geometric axis.

- The basic length unit is the minor radius a.
- The basic time scale is the Alfvén time $\tau_A = \mathsf{R}_0/V_A$, where V_A is the Alfvén velocity $V_A = B_0/\sqrt{\mu_0\rho_m} = B_0/\sqrt{\mu_0 m_i N_i}$.
- The mass density is normalized to its value on axis $\bar{\rho}_m = N_i/N_i(0)$.
- The normalized pressure is $\bar{P} = \mathsf{R}_0^2\mu_0 P/(a^2 B_0^2)$.
- The normalized magnetic field is $\bar{\mathbf{B}} = \mathsf{R}_0/(aB_0)\mathbf{B}$.

- The velocity is normalized to $\bar{\mathbf{V}} = (\tau_A/a)\mathbf{V}$
- The normalized current density is $\bar{\mathbf{J}} = (\mu_0 \mathsf{R}_0/B_0)\mathbf{J}$.

The two-fluid effects are scaled by the diamagnetic parameter $\bar{d}_i = \mathsf{R}_0/(a\tau_A\omega_{\mathsf{c},i}) = V_A/(a\omega_{\mathsf{c},i})$. Note that $\bar{d}_i$ characterizes the amplitude of the diamagnetic terms. The Lundquist number S is defined as $S = \tau_R/\tau_A = 1/\eta$ where $\tau_R = \mu_0 a^2/\eta$ is the resistive time.

Non-linear two-fluid MHD model

The XTOR-2F code [Lütjens and Luciani, 2010] is a non-linear and two-fluid full 3D MHD code. The toroidal MHD equilibrium is computed with the CHEASE code [Lütjens et al., 1996], which solves the Grad-Shafranov equation. The defined equilibrium and the associated mesh-grids are used as inputs to the XTOR-2F code. The following set of normalized MHD equations is modelled in the XTOR-2F code

$$\partial_t N + \boldsymbol{\nabla}\cdot(N\mathbf{V}) + \bar{d}_i\boldsymbol{\Xi}\cdot\boldsymbol{\nabla}P_i = \boldsymbol{\nabla}\cdot(D_\perp\boldsymbol{\nabla}N) + S_N \tag{2.45}$$

$$N\left[\partial_t\mathbf{V} + (\mathbf{V}.\boldsymbol{\nabla})\,\mathbf{V} + \bar{d}_i(\mathbf{V}_i^*\cdot\boldsymbol{\nabla})\mathbf{V}_\perp\right] = \mathbf{J}\times\mathbf{B} - \boldsymbol{\nabla}P + \mu\boldsymbol{\nabla}^2\left(\mathbf{V}+\mathbf{V}_i^*\right) \tag{2.46}$$

$$\begin{aligned}\partial_t P + \mathbf{V}\cdot\boldsymbol{\nabla}P + \gamma P\boldsymbol{\nabla}\cdot\mathbf{V} + \bar{d}_i\gamma\boldsymbol{\Xi}\cdot(T\boldsymbol{\nabla}P_i + P_i\boldsymbol{\nabla}T_i + P_e\boldsymbol{\nabla}T_e)\\ = (\gamma-1)\left[\boldsymbol{\nabla}\cdot\left(N\chi_\parallel\boldsymbol{\nabla}_\parallel T\right) + \boldsymbol{\nabla}\cdot(N\chi_\perp\boldsymbol{\nabla}_\perp T)\right] + S_H\end{aligned} \tag{2.47}$$

$$\partial_t\mathbf{B} = \boldsymbol{\nabla}\times(\mathbf{V}\times\mathbf{B}) + \bar{d}_i\boldsymbol{\nabla}\times\left(\frac{\nabla_\parallel P_e}{Ne}\right) - \boldsymbol{\nabla}\times(\eta\mathbf{J}) \tag{2.48}$$

Here, S_N and S_H are the particle and heat sources, $D_\perp$ is the normalized perpendicular particle diffusion coefficient, $\chi_\parallel$ and $\chi_\perp$ are the normalized parallel and perpendicular heat diffusivities and μ the normalized plasma dynamic viscosity. Also, $N = N_e = N_i$ is considered for the quasi-neutrality constraint.

The resistivity η varies in time with the plasma temperature, following Spitzer's resistivity law $\eta \propto T^{-3/2}$. The effect of the source terms S_N and S_H in Equations (2.45) and (2.47) is also to restore the density and pressure profiles within their characteristic diffusion times thanks to the perpendicular diffusion operators.

Numerical scheme

The system of MHD equations can be summarized into a matrix differential equation

$$\partial_t\mathbf{x} = \mathcal{F}(\mathbf{x}) \tag{2.49}$$

where $\mathbf{x}$ regroups all physical quantities (N, $\mathbf{V}$, P, $\mathbf{B}$). With a time discretization denoted with an index n, this equation is solved using a fully implicit scheme

$$\mathbf{x}_{n+1} - \mathbf{x}_n = \Delta t \mathcal{F} \left[\frac{\mathbf{x}_{n+1} + \mathbf{x}_n}{2} + \Theta(\mathbf{x}_{n+1} - 2\mathbf{x}_n + \mathbf{x}_{n-1}) \right] \tag{2.50}$$

where Δt is the time step of the discretization and Θ is a constant for numerical stabilization. This equation can be rewritten as

$$\mathbf{G}(\mathbf{\Delta}_n, \bar{\mathbf{x}}_n) \equiv \mathbf{\Delta}_n - \Delta t \mathcal{F} \left[\left(\frac{1}{2} + \Theta \right) \mathbf{\Delta}_n + \bar{\mathbf{x}}_n \right] = 0 \tag{2.51}$$

with $\mathbf{\Delta}_n \equiv \mathbf{x}_{n+1} - \mathbf{x}_n$ and $\bar{\mathbf{x}}_n \equiv (1 - \Theta)\mathbf{x}_n + \Theta \mathbf{x}_{n-1}$.

Finally, the equation (2.51) is solved at each iteration using a Newton-Krylov method

$$\mathbf{M}^{-1}\mathbf{G}'(\mathbf{\Delta}_n^k, \bar{\mathbf{x}}_n)(\mathbf{\Delta}_n^{k+1} - \mathbf{\Delta}_n^k) + \mathbf{M}^{-1}\mathbf{G}(\mathbf{\Delta}_n^k, \bar{\mathbf{x}}_n) = 0 \tag{2.52}$$

where $\mathbf{M}$ is the preconditioner matrix, k is the number of iterations of the Newton-Krylov method and $\mathbf{G}'$ is the derivative of $\mathbf{G}$ with respect to $\mathbf{\Delta}_n$. For the current version of XTOR-2F the Newton-Krylov method is provided either by the NITSOL-library or the PETSc-library. The preconditioning matrix $\mathbf{M}$ is applied to the system, in order to optimize the efficiency of the method. This matrix is chosen from the linearized MHD equations, and contains the coupling of the $\mathsf{n} = 0$ mode with the other toroidal modes. Also, the XTOR-2F code has been upgraded in order to improve the preconditioning matrix when additional equations to model the impurity transport [Ahn et al., 2016b] or the propagation of current sources [Février et al., 2016] have to be solved along with MHD equations that model bulk plasmas.

The XTOR-2F code uses a finite difference method in the radial direction, and a pseudo-spectral method in the poloidal and toroidal directions. Time-steps are automatically adjusted for an optimum resolution of the Newton-Krylov solver. The plasma dynamics such as sawtooth crashes, which occur during a very short time scale compared to the confinement time, can then be studied with an appropriate time resolution [Nicolas et al., 2012][Nicolas et al., 2014][Ahn et al., 2016a][Ahn et al., 2016b].

2.4.2 Sawtooth simulations with the XTOR-2F code

Parameter rescaling

It is necessary to rescale the plasma parameters in the simulations to avoid excessive simulation times. In particular, large resistive times correspond to the Lundquist number in tokamaks of the order $S \sim 10^8 - 10^9$, which is numerically demanding. Hence, the plasma resistivity is rescaled by orders of magnitude in the simulations. Usually, $S \sim 10^7$ is used in the simulations presented in this thesis. Other plasma parameters are rescaled so as to preserve the ratios between different time scales with respect to experimental values.

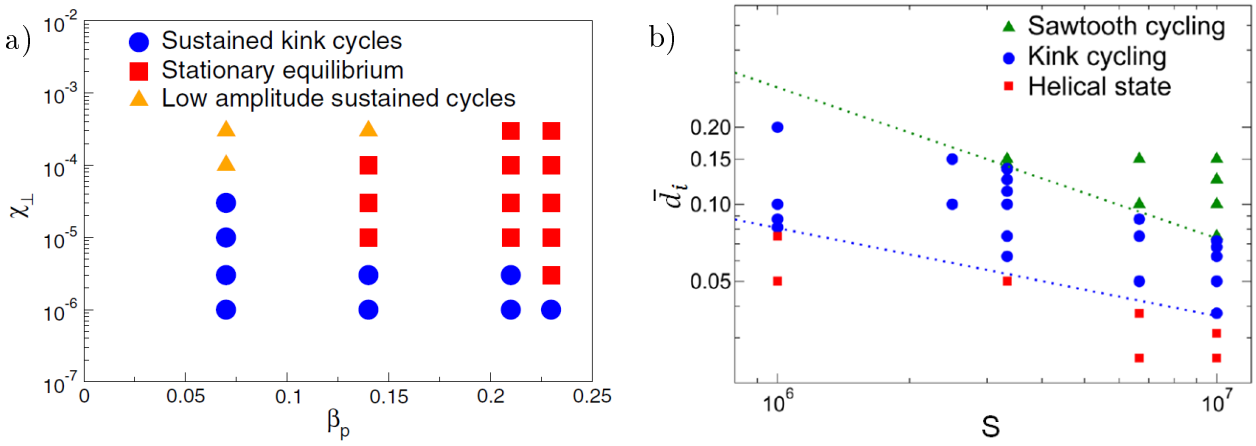

Figure 2.4: (a) Dependence on β_p and $\chi_\perp$ of kink cycling and helical state regimes for a 'low shear' equilibrium [Halpern et al., 2011a]. (b) Different regimes of cycling when varying S and $\bar{d}_i$ [Halpern et al., 2011b].

In addition, different regimes of the internal kink mode instability have already been identified by Halpern *et al.* for a circular plasma shape [Halpern et al., 2011a][Halpern et al., 2011b] : saturated helical equilibrium, kink cycling and sawtooth oscillations. For a defined initial equilibrium, the transitions between different regimes occur while varying the rescaled plasma parameter values such as the perpendicular heat diffusivity $\bar{\chi}_\perp$, the poloidal beta β_p, the Lundquist number S and the diamagnetic parameter $\bar{d}_i$ (Figure 2.4).

Grids and convergence

The width of the current sheet w during the reconnection roughly varies as $w \propto S^{-1}$. Therefore, the radial resolution is chosen such that the current sheet at the reconnection layer can be accurately computed, for a chosen Lundquist number.

The toroidal and poloidal mode resolutions used in the simulations are a sensitive subject. Increasing the mode resolution is numerically demanding as a spectral method is used for the poloidal and toroidal directions. A signature of an insufficient resolution is a saturation of the mode energies at the same level [Aydemir et al., 2015]. This is not observed in the XTOR-2F simulations of sawteeth. A discussion on the mode resolution used in the XTOR-2F simulations to describe sawtooth cycles can be found in Refs.[Lütjens and Luciani, 2010][Halpern et al., 2011b][Ahn et al., 2016a].

2.5 Summary

In this chapter, we have explored basic concepts and modelling tools necessary to understand the sawtooth phenomenon. Sawteeth are due to the unstable internal kink mode with poloidal and toroidal mode numbers $(\mathsf{m}, \mathsf{n}) = (1, 1)$. The internal kink mode is characterized by a shift of the core region inside the resonant $q = 1$ surface in the radial direction. The

inner core is rigidly pushed towards this surface, creating a current sheet where non-ideal effects cause magnetic reconnection.

The MHD framework is adopted to model sawteeth. The numerical tools presented in Section 2.4 are used throughout this thesis. The CHEASE code provides the MHD equilibrium, and the XTOR-2F code is used to solve the set of two-fluid MHD equations. The plasma parameters are rescaled in order to prevent excessive numerical costs while maintaining physical aspects.

These tools are used in the following chapters to study compound sawteeth (Chapter 3) and the transport of heavy impurities during sawtooth cycles (Chapter 5).

CHAPTER 3

Non-linear dynamics of compound sawteeth

Contents

Sustained sawtooth cycles are simulated with the XTOR-2F code in an elongated plasma geometry as the majority of tokamaks have a non-circular poloidal cross-section. This will allow one to model experimental scenarios and compare with measurements via synthetic diagnostics which have been implemented in the XTOR-2F code. An appropriate set of rescaled plasma parameters is necessary to simulate sawteeth. While performing a parameter scan, several simulations in an elongated plasma geometry contained sawtooth cycles which exhibit features similar to compound sawteeth reported in experiments. These simulations are analysed in this chapter, in order to understand the onset of the partial crash during the sawtooth ramp phase. The main results presented in this chapter are published in Ref.[Ahn et al., 2016a]

3.1 Partial crashes during sawtooth ramp phase

A drop of the central temperature or density value during the sawtooth ramp phase is frequently observed in plasma discharges [Pfeiffer, 1985][Campbell et al., 1986][Nagayama

et al., 1996]. This phenomenon is called 'partial crash' as its amplitude is smaller than the one observed during a 'full' sawtooth crash (Figure 2.1). It should be noted that the terminology 'partial crash' is associated to the previously described phenomenon, and does not imply any hypothesis whether the reconnection is complete or not. These sawteeth are then designated as 'compound' sawteeth.

It has been reported from ECE measurements that during the partial crash, the electron temperature drops only in an off-axis region [Taylor et al., 1986][Campbell et al., 1986]. Also, SXR tomographic inversions of discharges in Tokamak de Varennes [Janicki et al., 1990] and in EAST [Xu et al., 2014], show that the hot core is preserved during the partial crash. Indeed, the hot core is radially displaced and rotates in the poloidal direction, inside the $q = 1$ surface. At the end of the partial crash, the displaced hot core regains its equilibrium position before the precursor oscillations of the following sawtooth full crash appear. The partial crash is thus clearly different from the sawtooth crash described in the previous paragraph, which is characterized by a complete expulsion of the hot core out of the $q = 1$ surface (Figure 2.3). It has also been reported that the partial relaxation is frequently observed after a sawtooth collapse followed by post-cursor oscillations [Campbell et al., 1986].

Theoretical models to understand the partial crash usually rely on 'partial' (or incomplete) reconnection. In contrast to complete reconnection, the magnetic surfaces that reconnect are in a region off the initial magnetic axis during the partial reconnection [Porcelli et al., 1996]. Hence, q_0 remains below unity throughout the partial reconnection process for an initial q-profile with $q < 1$ in the core region. A possible explanation for partial reconnection is the existence of a critical island width [Biskamp and Sato, 1997]. In that model, the magnetic reconnection occurs as the Kadomtsev reconnection model in the beginning, until the cooler island reaches its critical width where the reconnection process stops. Also, the existence of multiple $q = 1$ surfaces was proposed to understand the partial crash [Pfeiffer, 1985][Parail and Pereverzev, 1980][Denton et al., 1986][Aydemir et al., 1989]. The reconnecting magnetic surfaces are those around the region where q is below unity, which is located off the initial magnetic axis. Hence, multiple reconnection processes may explain the preserved hot core during the partial crash.

Resistive MHD simulations were able to reproduce compound sawteeth when using a heat diffusivity that depends on the temperature gradient in cylindrical geometry [Denton et al., 1986], or on pressure in toroidal geometry [Aydemir et al., 1989]. The heat transport coefficients thus defined generate a locally higher current density in the off-axis region, which lead to the onset of multiple $q = 1$ surfaces. Hence, multiple reconnection processes offer a possible explanation for compound sawteeth. Still, the precise conditions which dictate the onset and dynamics of partial crashes remain poorly understood.

This chapter presents the main results published in Ref.[Ahn et al., 2016a], which illustrates and analyzes non-linear full 3D MHD simulations of compound sawteeth with the XTOR-2F code [Lütjens and Luciani, 2010].

3.2 Set up of parameters for XTOR-2F simulations

3.2.1 Physical parameters rescaling

For the present study, the Lundquist number is rescaled to $S = 10^7$ for the XTOR-2F sawtooth simulations. The diamagnetic parameter is then set to $\bar{d}_i = 0.15$, which is about two or three times larger than the experimental values. Also, the normalized perpendicular heat diffusivity of $\bar{\chi}_{\perp 0} = 3 \times 10^{-6}$ is chosen on axis and $\bar{\chi}_\perp \propto \eta$. Thus, the products $S\bar{d}_i$ and $S\bar{\chi}_\perp$ are about a third of those expected from the experiments. The characteristic time for particle diffusion is chosen to be 10 times larger than the heat diffusion time. As far as the viscosity is concerned, measurements of the plasma viscosity in experiments are not available yet. For the following simulations, the normalized plasma viscosity is set to $\bar{\mu} = 7.5 \times 10^{-6}$, so that the magnetic Prandtl number is $Pr_m = S\bar{\mu} = 75$.

The parameter $\tau \equiv P_i/P_e$ becomes $\tau = T_i/T_e$ under the quasi-neutrality constraint $N_e = N_i$. This parameter thus accounts for the difference between the electron and ion temperatures. In the following simulations, electron and ion temperature are equal, i.e. $\tau = 1$.

3.2.2 Choice of the initial equilibrium and its stability

The rescaling of the plasma parameters has to be performed for each initial equilibrium. The toroidal MHD equilibrium is computed with the CHEASE code [Lütjens et al., 1996] with the chosen set of initial pressure and current profiles. A number of parameters play an important role in the internal kink mode stability.

- First, for a given current profile, which determines the corresponding q-profile, the internal kink mode stability is determined by the value of the poloidal beta β_p. In the following, the poloidal beta is a volume averaged quantity computed by the CHEASE code

$$\beta_p = \frac{8\pi}{I_{tot}^2 \mathsf{R}_0} \int_\Omega P \mathcal{J} \mathrm{d}\psi \mathrm{d}\theta \tag{3.1}$$

  where I_{tot} is the total toroidal current, R_0 the major radius, Ω the plasma cross section, $\mathcal{J}$ the Jacobian and P the kinetic pressure.

- Second, the q-profile plays a very important role. Indeed, the internal kink mode stability depends on the current profile which determines the shear, the on-axis safety factor value q_0 and the radial position of the $q = 1$ surface [Bussac et al., 1975][Lütjens et al., 1992]. For instance, it has been shown that the internal kink mode is unstable even for a plasma pressure equal to zero for a sufficiently large inversion radius [Turnbull and Troyon, 1989]. Experimental observations in Tokamak de Varennes [Janicki et al., 1990] clearly show that compound sawteeth are obtained when increasing the total current value i.e. decreasing the safety factor value q_a at the edge (Figure 3.1). The

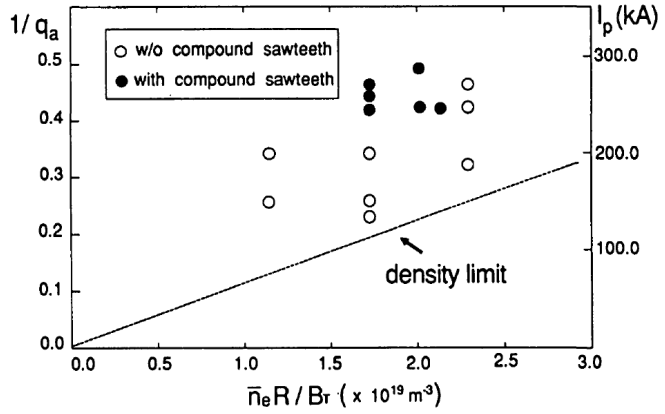

Figure 3.1: Experimental conditions on the electron density and total current to obtain compound sawteeth in Tokamak de Varennes discharges [Janicki et al., 1990]. It shows that, for a fixed value of electron density, compound sawteeth are observed when the total current value is above a threshold.

flattening of the q-profile is likely to push the inversion radius toward the edge. Hence, the inversion radius is chosen as a control parameter for this study.

- Finally, it is well known that the shape of the magnetic surfaces plays an important role in the internal kink mode stability threshold [Lütjens et al., 1992][Coppi and Coppi, 1992][Martynov et al., 2005]. The internal kink mode is strongly destabilized by the elongation κ. Indeed, the plasma elongation κ significantly lowers $\beta_{p,c}$, and above a certain elongation κ_c, the internal kink mode is unstable even for a vanishing plasma pressure [Martynov et al., 2005]. For this reason, the plasma elongation offers a second control parameter different from the radial position of the $q = 1$ surface.

Two cases of sawtooth simulations without partial crash are presented. One has an elongation at separatrix $\kappa_a = 1.6$ and the $q = 1$ radius is at $r_s = 0.4\,a$, and the other has an elongation $\kappa_a = 1.8$ and $r_s = 0.32\,a$. The case with an elongation $\kappa_a = 1.6$ and the inversion radius at $r_s = 0.4\,a$ will be the reference case throughout this work (Figure 3.2-a). Also, two cases of compound sawtooth simulations are obtained from the reference case : one by increasing the elongation to $\kappa_a = 1.8$ with a fixed $q = 1$ position at $r_s = 0.4\,a$ (Figure 3.2-b), and the other by increasing the inversion radius to $r_s = 0.47\,a$ at a fixed geometry. The triangularity at separatrix is set to $\delta_a = 0.4$ for all the cases. The inverse aspect ratio for theses simulations is set to $a/R_0 = 0.37$, which is close to actual values in tokamaks.

The critical value $\beta_{p,c}$ is deduced from the study of the ideal linear growth rate of the $\mathsf{n} = 1$ mode by varying the initial pressure profile at fixed current profile at equilibrium. Indeed, $\beta_{p,c}$ corresponds to the marginal stability point of the internal kink mode in the ideal MHD (Figure 3.3). For the reference case with $\kappa_a = 1.6$ and $\delta_a = 0.4$, it is found that $\beta_{p,c} \simeq 0.15$. In the simulations, the value of β_p is chosen to be approximately $2/3\,\beta_{p,c}$ in order to obtain an initial equilibrium linearly stable in the ideal MHD and unstable in presence of the resistivity [Halpern et al., 2011a]. From this equilibrium, sustained sawtooth oscillations are then obtained with the XTOR-2F code by rescaling the plasma parameters as described

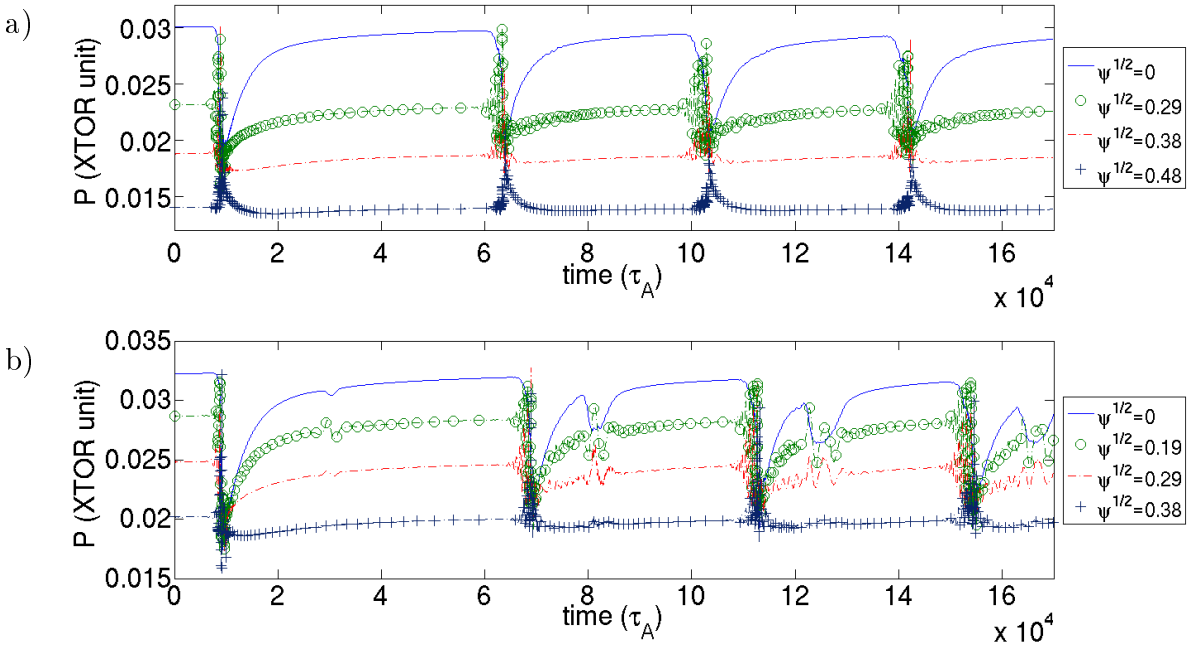

Figure 3.2: Time evolution pressure at different radii during sawtooth cycles in the cross section geometry (a) $\kappa_a = 1.6$, (b) $\kappa_a = 1.8$. For both cases, $\delta_a = 0.4$ and the $q = 1$ surface is at $r_s = 0.4\,a$. The difference between the initial equilibrium and the asymptotic equilibrium is marked by the difference on the sawtooth period.

κ_a	δ_a	β_p	S	$\bar{d}_i$	r_s/a	partial crash
1.6	0.4	0.1	10^7	0.15	0.4	no
1.6	0.4	0.1	10^7	0.15	0.47	yes
1.8	0.4	0.1	10^7	0.15	0.4	yes
1.8	0.4	0.1	10^7	0.15	0.32	no

Table 3.1: Summary of the rescaled plasma parameters used in this work, for different cases. $\bar{\chi}_\perp = 3 \times 10^{-6}$, $\bar{\mu} = 7.5 \times 10^{-6}$ are the same for all simulations.

in Section 3.2.1. The geometry and rescaled plasma parameters used in the XTOR-2F code for different plasma cross sections are summarized in Table 3.1.

It is stressed that the equilibrium during the sustained sawtooth oscillations differs from the initial equilibrium. Indeed, during the sustained sawtooth cycles, the internal kink mode is destabilized before the initial equilibrium is regained. Hence, the change of the equilibrium state is marked by the difference of the q-profiles corresponding to the respective equilibria (Figure 3.4). In the XTOR-2F code, the safety factor q is computed from the quantity $B_\phi/(\mathcal{J}B_\theta)$, averaged along the initial magnetic surface. Here, B_θ and B_ϕ are respectively the poloidal and toroidal components of the magnetic field. The computed q-profile gives $q_0 \simeq 0.94$ and $r_s \simeq 0.35\,a$ for the asymptotic equilibrium, whereas $q_0 \simeq 0.77$ and $r_s = 0.4\,a$ for the initial equilibrium. Also, this can be seen in Figure 3.2, where the first sawtooth cycle has a larger period ($\tau_{ST} \simeq 5 \times 10^4\,\tau_A$) than the sustained sawtooth cycles ($\tau_{ST} \simeq 3.5 \times 10^4\,\tau_A$) for the reference case.

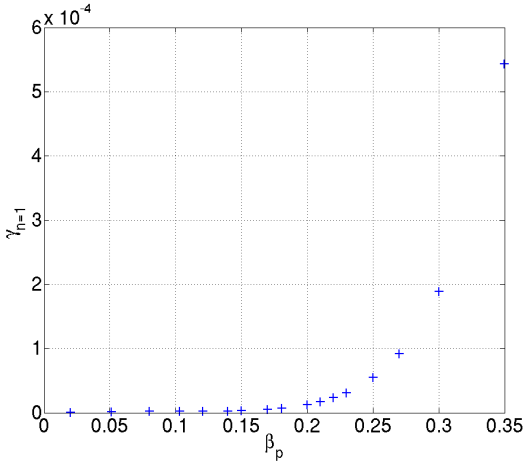

Figure 3.3: The linear growth rate of the internal kink mode in ideal MHD for different values of β_p in an elongated plasma cross section ($\kappa_a = 1.6$, $\delta_a = 0.4$) and the $q = 1$ surface at $r_s = 0.4\,a$. In this case, $\beta_{p,c} \simeq 0.15$.

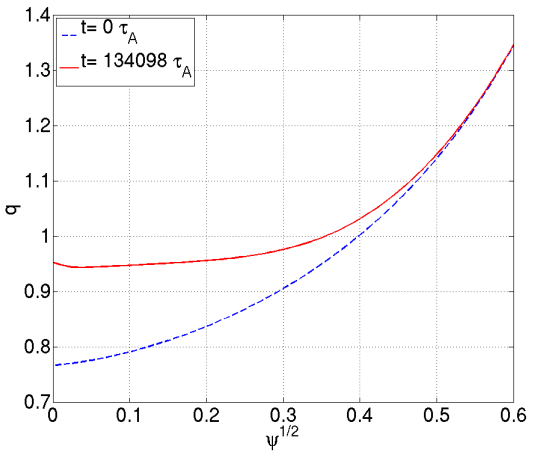

Figure 3.4: q-profiles of the initial (*dashed line*) and the asymptotic (*solid line*) equilibria for the geometry $\kappa_a = 1.6$, $\delta_a = 0.4$ and the $q = 1$ surface at $r_s = 0.4\,a$. The $q = 1$ radius is changed from $r_s = 0.4\,a$ to $r_s \simeq 0.35\,a$, as the initial equilibrium is not regained.

3.3 XTOR-2F simulation results

3.3.1 q-profile after a sawtooth full relaxation

Before studying partial crashes, the plasma behaviour during the ramp phase of an ordinary sawtooth is investigated in order to understand the crash onset. For this purpose, sustained sawtooth oscillations without partial crash are simulated with the XTOR-2F code. Sustained sawtooth oscillations are computed for the following sets of elongation κ_a, triangularity δ_a and normalized inversion radius r_s/a : (κ_a, δ_a, r_s/a)=(1.6, 0.4, 0.4) and (1.8, 0.4, 0.32). The following analysis focuses on the reference case with (κ_a, δ_a, r_s/a)=(1.6, 0.4, 0.4).

A flat q-profile slightly above unity after a sawtooth crash is predicted by the Kadomtsev complete reconnection model and is reproduced by the XTOR-2F simulations (Figure 3.5). In the simulations, the q-profile remains flat for a while after a sawtooth relaxation, during

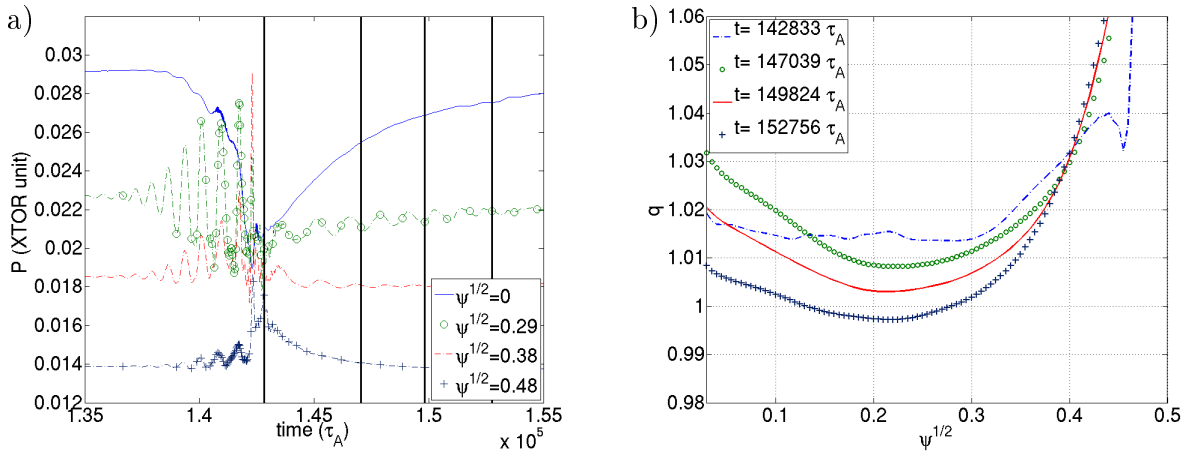

Figure 3.5: (a) Time evolution of the pressure at different radii for sawtooth simulations with the case $\kappa_a = 1.6$, $\delta_a = 0.4$ and$r_s = 0.4\,a$. (b) Evolution of q-profiles after the sawtooth crash, each time point is marked by a vertical line in (a). The q-profile is flat at the sawtooth crash and becomes non-monotonic during the ramp phase.

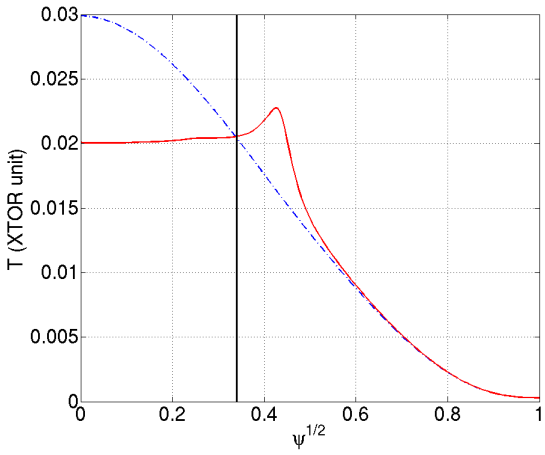

Figure 3.6: Temperature profiles before (*dashed line*) and after (*solid line*) the sawtooth crash. The inversion radius is represented by the vertical line.

the ramp phase, before recovering the pre-crash equilibrium state. The safety factor in the core region after a crash is very close to unity ($|q-1| < 3\%$). Also, non-monotonic q-profiles are observed during the ramp phase, leading to the formation of two $q = 1$ surfaces at $t = 1.53 \times 10^5\,\tau_A$. The temperature after the sawtooth crash is locally higher between the inversion and mixing radii compared to the flattened profile in the core region (Figure 3.6), which is also predicted by the complete reconnection model. As a consequence, the toroidal current density is locally enhanced in the off-axis region. That is observed due to a lower plasma resistivity which enhances the hollow profile of the safety factor.

It has been shown that the internal kink mode can be ideally unstable even with $q > 1$. Analytical studies show that the internal kink mode can be unstable for ultra-flat ($|q-1| \ll 1$) [Hastie and Hender, 1988] and non-monotonic q-profiles [de Blank and Schep, 1991], although $q > 1$. Moreover, for a given MHD energy δW_T, the growth rate is enhanced by

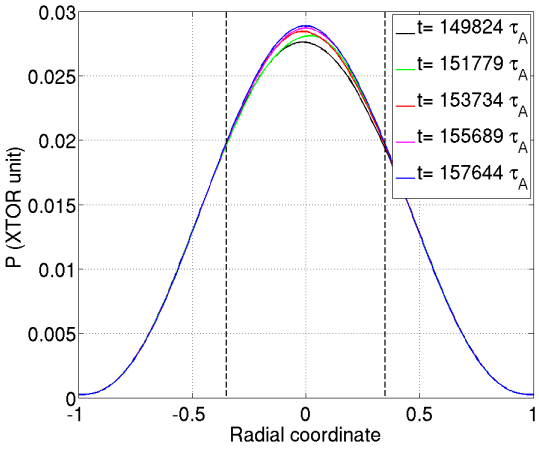

Figure 3.7: Time evolution of the pressure profiles (at $\theta = 0$) during the ramp phase for the case $\kappa_a = 1.6$, $\delta_a = 0.4$ and $r_s = 0.4\,a$. The times corresponds to Poincaré plots in Figure 3.8. The inversion radius is represented by dashed vertical lines.

low shear values [Hastie et al., 1987] and the internal kink mode is destabilized at the radius corresponding to the lowest shear value [Lütjens and Luciani, 1997]. However, the q-profile is difficult to determine after the sawtooth crash due to the remaining structures which take some time to reorganize. Poincaré plots are then more relevant in order to get indications on the evolution of the magnetic topology. Poincaré plots are used to identify magnetic surfaces, when they exist, by tracking field lines during several hundreds of toroidal turns. This tool is useful when visualizing complex magnetic structures such as islands and stochastic regions.

The present analysis focuses on the time interval between the end of the sawtooth crash post-cursor and the time needed for recovering an asymptotic equilibrium. These cases are defined as sawteeth 'without partial crash' as the time evolution of the pressure does not show any drop of central pressure value (Figures 3.7, 3.8-a). However, a reorganization of the magnetic surfaces is visible in the Poincaré plots during the sawtooth ramp phase from sawtooth simulations without partial crash (Figure 3.8). Indeed, the magnetic reorganization is mainly localized in the off-axis region where the shear is equal to zero (Figure 3.5). Magnetic structures with multiple helicities such as (2,2), (3,3) are also visible in the Poincaré plots (e.g. in Figure 3.8-d).

3.3.2 Stability of the $\mathsf{n} = 1$ mode during a sawtooth cycle

Methodology

It is useful to assess the linear stability of the modes at different moments during a sawtooth cycle, in order to elucidate the mechanisms that underlie the observations presented in Section 3.3.1. For this purpose, the equilibria which correspond to 'snapshots' of the plasma at the times of interest are reconstructed. The plasma state regarding the mode stability, at different moments of the sawtooth cycle, is then deduced with precision from the non-

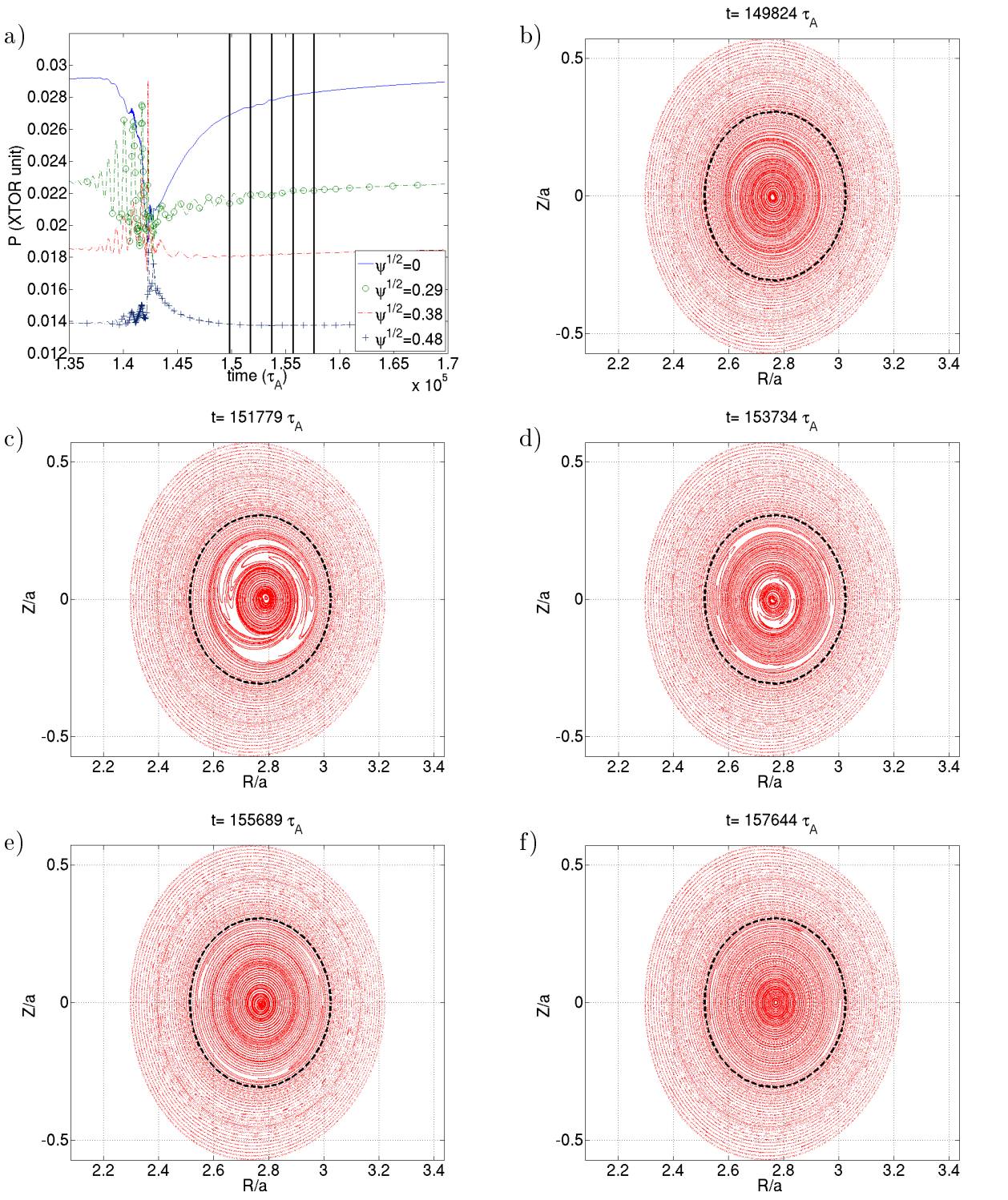

Figure 3.8: (a) Time evolution of the pressure at different radii. (b)-(f) Poincaré plots of the core region ($r < 0.6\,a$) after post-cursor oscillations during the time interval marked by vertical lines in (a), for the case without partial crash in the geometry $\kappa_a = 1.6$, $\delta_a = 0.4$ and the $q = 1$ surface at $r_s = 0.4\,a$. The dashed lines in the Poincaré plots represent the $q = 1$ surface at equilibrium.

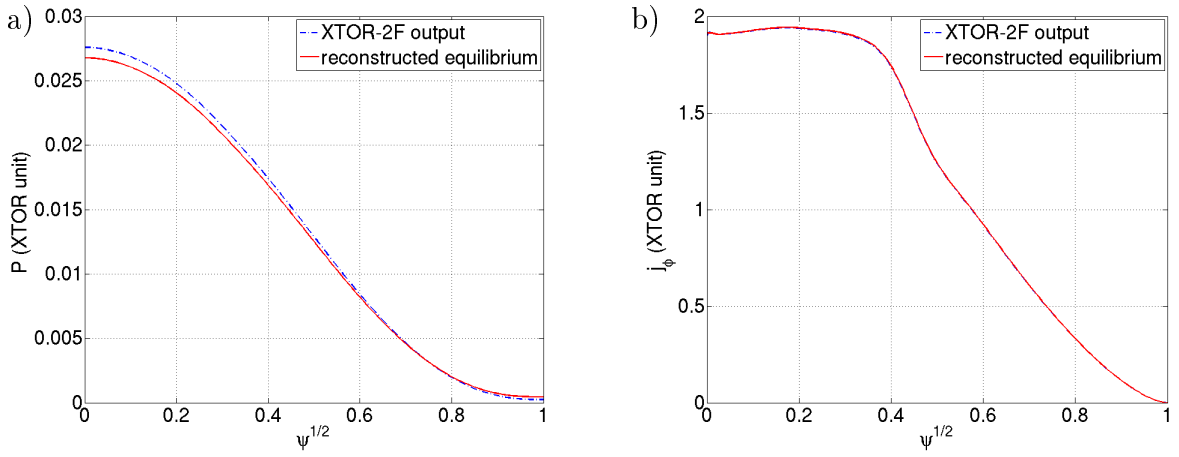

Figure 3.9: Comparison of (a) the pressure profile and (b) the toroidal current density j_ϕ profile between the reconstructed equilibrium by CHEASE (*solid line*) and the XTOR-2F output (*dashed line*). The snapshot corresponds to the elongated geometry $\kappa_a = 1.6$, $\delta_a = 0.4$ and the $q = 1$ surface at $r_s = 0.4\,a$, at $t = 1,50 \times 10^5\,\tau_A$.

linear simulations with the reconstructed equilibria. These equilibria are reconstructed by the CHEASE code [Lütjens et al., 1996], which solves the Grad-Shafranov equation (2.7). It is necessary to define P' and II' as inputs of the CHEASE code in order to solve the Grad-Shafranov equation. However, the function II' is unknown at the time of interest.

The $\mathsf{m} = \mathsf{n} = 0$ components of the pressure P and the toroidal component of current density J_φ are extracted from the sawtooth simulations with the XTOR-2F code, at different moments. The CHEASE code then reconstructs the equilibria with precision (Figure 3.9), in order to be used as input for determining the plasma stability at the selected times. This computation supposes that the flux surfaces of the snapshot are identical to the initial flux surfaces. From the reconstructed toroidal equilibria, non-linear MHD simulations with the XTOR-2F code are performed to study the energy evolution of the $\mathsf{n} = 1$ mode with the same mode resolutions and plasma parameters as Table 3.1.

Results

For the reference simulation of sawteeth without partial crash ($\kappa_a = 1.6$, $\delta_a = 0.4$, $r_s = 0.4\,a$), the $\mathsf{n} = 1$ mode energy behaviour is represented in Figure 3.10 from the reconstructed equilibria. The two time points, where the previously described method is applied, correspond respectively to $t = 1.50 \times 10^5\,\tau_A$ and $t = 1.58 \times 10^5\,\tau_A$. It can be noticed that the magnetic surfaces, represented in the corresponding Poincaré plots (Figures 3.8-b and 3.8-f), are close to the asymptotic equilibrium.

In Figure 3.10, it is observed that the $\mathsf{n} = 1$ mode is unstable for the time slice $t = 1.50 \times 10^5\,\tau_A$ just after the end of the sawtooth crash post-cursor. The instantaneous growth rate of the $\mathsf{n} = 1$ mode amplitude reads $\gamma \simeq 1.2 \times 10^{-4}$ before the non-linear saturation at $t = 4.9 \times 10^4\,\tau_A$. In contrast, the growth rate of the $\mathsf{n} = 1$ mode instability is almost

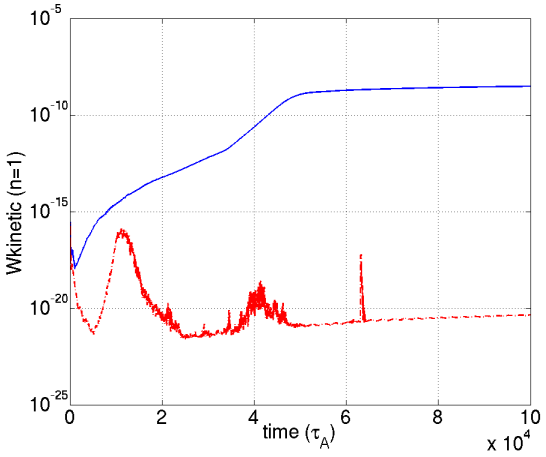

Figure 3.10: Time evolution of the kinetic energy of the $\mathsf{n} = 1$ mode from reconstructed equilibria at $t = 1.50 \times 10^5\,\tau_A$ (*solid line*) and $t = 1.58 \times 10^5\,\tau_A$ (*dashed line*). The two times correspond respectively to the Poincaré plots in Figures 3.8-b and 3.8-f. For the latter case (*dashed line*), the energy is below the noise level of the solver.

vanishing for the latter time $t = 1.58 \times 10^5\,\tau_A$. These growth rates are smaller than the $\mathsf{n} = 1$ mode growth rate for a full sawtooth crash $\gamma \simeq 4.7 \times 10^{-4}$. Moreover, the energy saturates at $W_{sat} \sim 10^{-9}$ in normalized value, which is several orders of magnitude smaller than $W_{sat} \sim 10^{-4}$ for the reconstructed equilibrium just before the sawtooth full crash. The analysis of the poloidal mode spectra shows that the energy content of the $\mathsf{n} = 1$ mode is dominant for the poloidal mode number $\mathsf{m} = 1$. This means that the internal kink mode $(\mathsf{m}, \mathsf{n}) = (1, 1)$ is unstable during the sawtooth ramp phase, although it does not impact the central pressure values (Figure 3.8-a) and the magnetic surfaces in the core region (Figures 3.8-b to 3.8-f).

The origin of this destabilization can be explained by the q-profiles in the core region, during the sawtooth ramp (Figure 3.5). It is shown that the internal kink mode can be unstable even for $q > 1$ when q is very close to unity [Hastie and Hender, 1988][de Blank and Schep, 1991][Hastie et al., 1987]. Indeed, for flat q-profiles, the magnetic shear $\hat{s} \ll 1$. In the analytical expressions of the linear growth rate, small values of the magnetic shear $\hat{s}$ enhance the growth rate [Hastie et al., 1987]. Also, it can be noticed that the radial position of the minimum safety factor value at $t = 1.50 \times 10^5\,\tau_A$ (Figure 3.5) corresponds to the radius where the magnetic activity occurs (Figure 3.8-c). Hence, the internal kink mode is weakly unstable during the sawtooth ramp phase, and saturates to a low level. As a consequence, the instability is not sufficient to trigger a pressure drop in the core region (Figure 3.7).

3.3.3 The partial crash during the sawtooth ramp phase

In this section, XTOR-2F simulation results of compound sawteeth are described. From the reference case ($\kappa_a = 1.6$, $\delta_a = 0.4$, $r_s = 0.4\,a$), sustained sawtooth cycles with partial relaxations are obtained by increasing the elongation to $\kappa_a = 1.8$ at fixed $q = 1$ radius in

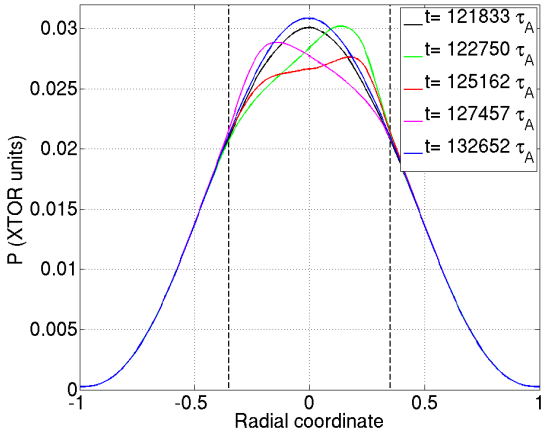

Figure 3.11: Time evolution of the pressure profiles (at $\theta = 0$) during the ramp phase for the case $\kappa_a = 1.8$, $\delta_a = 0.4$ and $r_s = 0.4\,a$. The times correspond to pressure contour plots in Figure 3.12. The inversion radius is represented by dashed vertical lines.

one case, and increasing the inversion radius to $r_s = 0.47\,a$ at fixed geometry for the other case. In this section, the case with the geometry $\kappa_a = 1.8$, $\delta_a = 0.4$ and the $q = 1$ position at $r_s = 0.4\,a$ is analysed. Figure 3.2-b and Figure 3.11 show that a drop of the central pressure occurs during the sawtooth ramp phase, at about $10^4\,\tau_A$ after a sawtooth full crash. The amplitude of this drop is much smaller than the ordinary sawtooth crash. This relaxation, which occurs during the sawtooth ramp phase, is characteristic of the experimental observations of compound sawteeth [Pfeiffer, 1985][Janicki et al., 1990][Xu et al., 2014][Campbell et al., 1986].

The 2-D pressure evolution during the partial crash is represented in Figure 3.12. Different time points during the partial crash process are chosen and indicated with dashed vertical lines in Figure 3.12-a. The evolution of the pressure contours during the partial relaxation shows that the hot core is preserved during the whole process. It is radially displaced and rotates in the poloidal direction, in a core region located inside the $q = 1$ surface (Figures 3.12-b to 3.12-f). The evolution of the magnetic topology during a partial crash at the time points marked in Figure 3.12-a is represented in the Poincaré plots (Figure 3.13). The dynamics of the hot core described in the contour plots of pressure, is also observed in the Poincaré plots. The magnetic structure corresponding to the hot core is radially displaced and rotates poloidally, without disappearing completely, even during the partial crash. The magnetic topology during the partial crash is modified only in the core region inside the $q = 1$ surface represented with a dashed curve in the Poincaré plots. Also, a significant magnetic activity is observed in the very core region near the center of the plasma, while the hot core is radially displaced with the magnetic axis (Figure 3.13-c). These observations are reminiscent of a saturated helical state of an internal kink mode preserved in the core region.

The q-profile before the partial relaxation is flat in the core region, similar to the case presented in Section 3.3.1. Again, the internal kink mode is unstable during the sawtooth

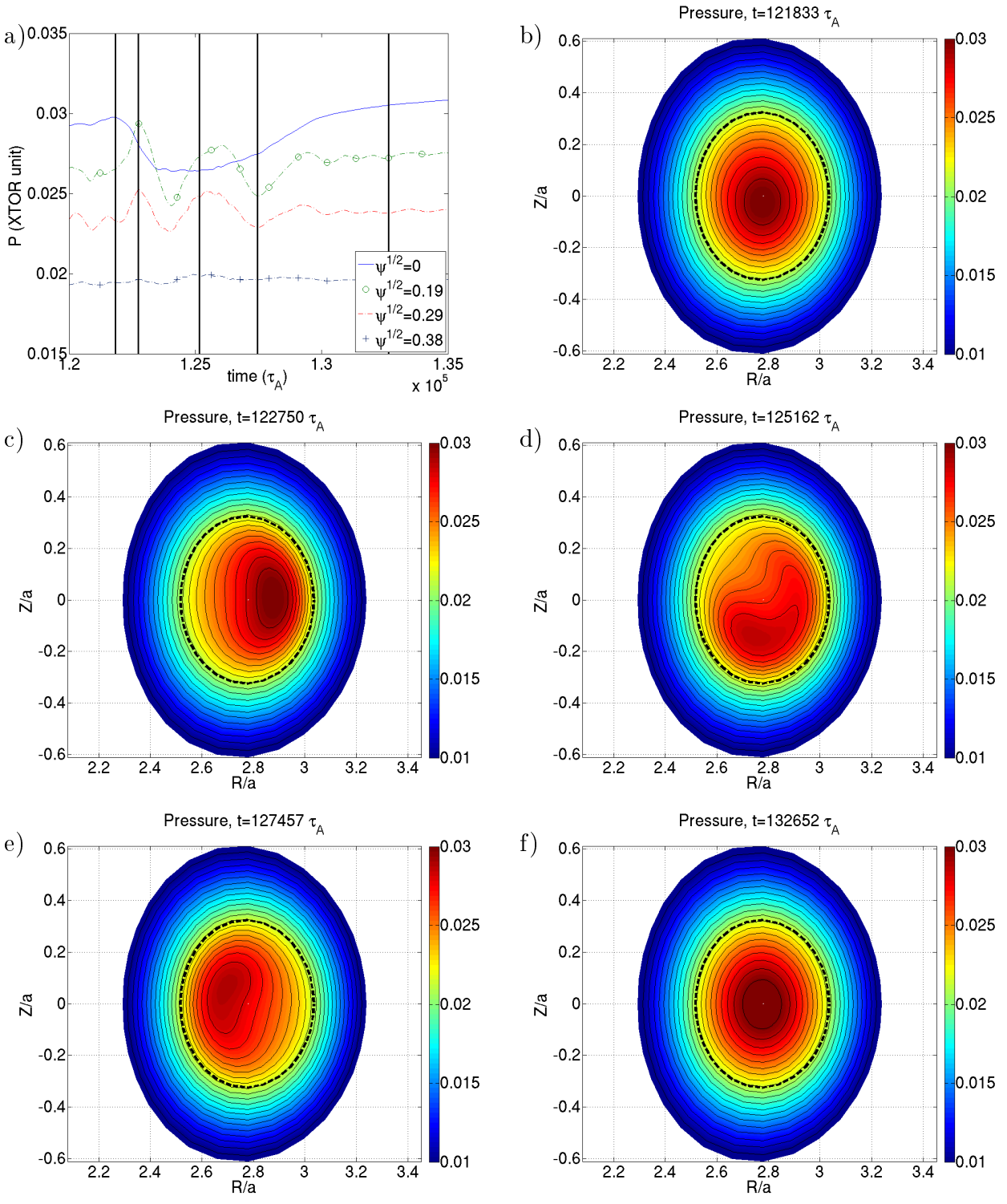

Figure 3.12: (a) Time evolution of pressure at different radii, zoomed at the time interval where the partial crash occurs. (b)-(f) The pressure contours of the core region ($r < 0.6\,a$) at different time points marked by vertical lines in (a). In the contour plots, some of the flux surfaces and the $q = 1$ surface at equilibrium are represented respectively by thin solid lines and dashed lines.

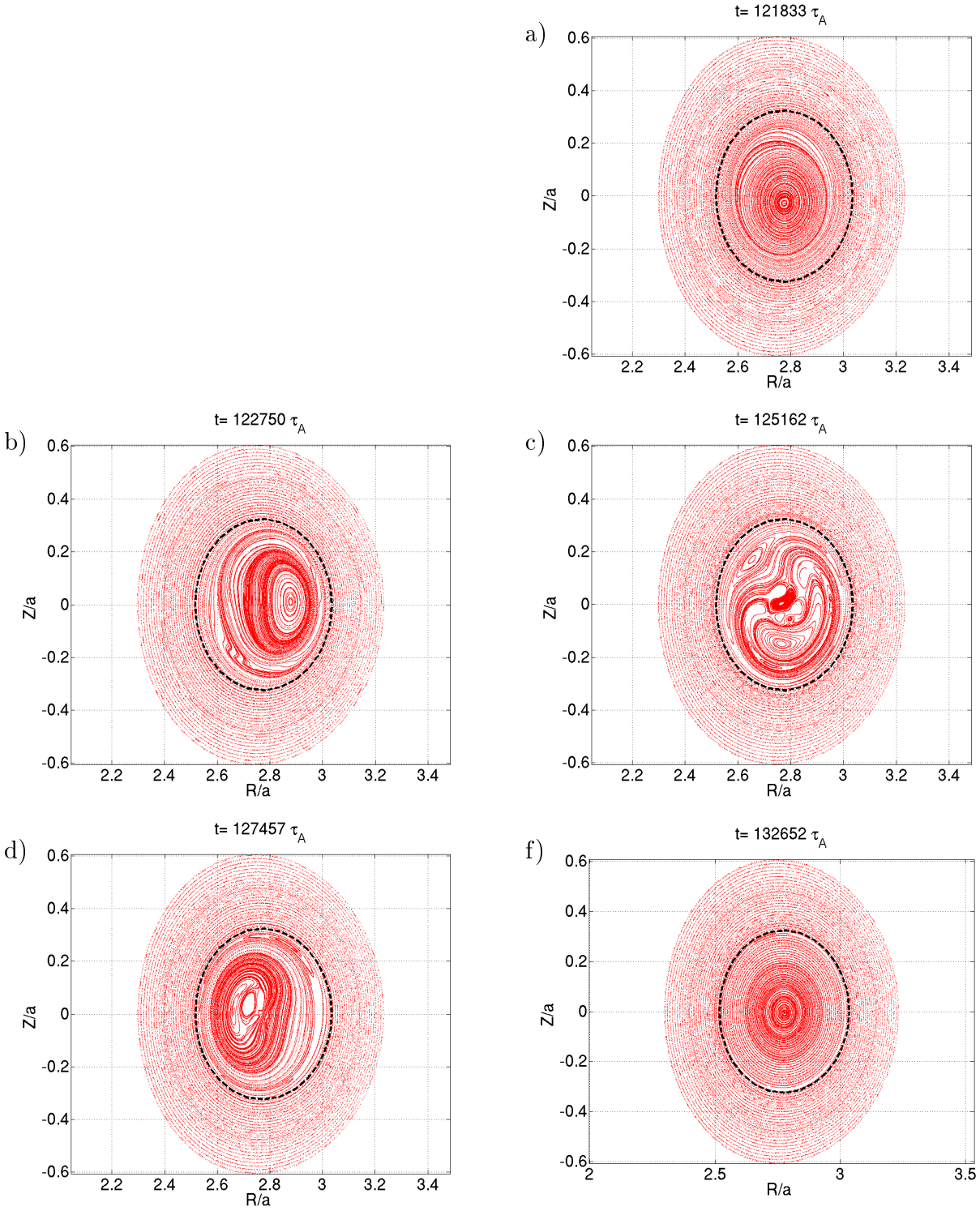

Figure 3.13: (a)-(e) Poincaré plots of the core region ($r < 0.6\,a$) during the partial crash. Each time point corresponds respectively to the contour plots of Figures 3.12-b to 3.12-f. The dashed lines in the Poincaré plots represent the $q = 1$ surface at equilibrium.

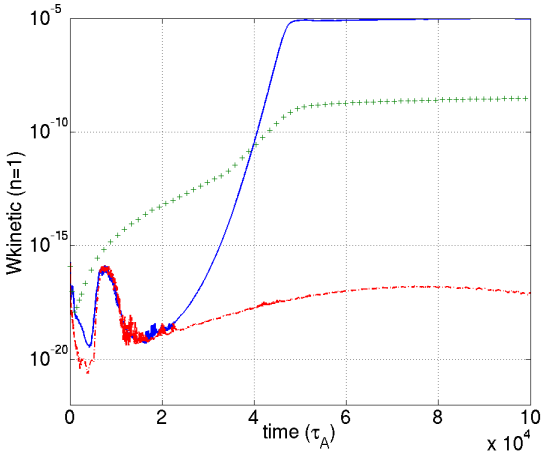

Figure 3.14: In solid lines, the time evolution of the kinetic energy of the $\mathsf{n} = 1$ mode from reconstructed equilibria before ($t = 1.22 \times 10^5\,\tau_A$, *solid line*) and after ($t = 1.33 \times 10^5\,\tau_A$, *dashed line*) the partial crash ($\kappa_a = 1.8$, $\delta_a = 0.4$ and $r_s = 0.4\,a$). The two times correspond respectively to the Poincaré plots in Figures 3.13-a and 3.13-e. In dashed line, the same plot as Figure 3.10 ($\kappa_a = 1.6$, $\delta_a = 0.4$ and $r_s = 0.4\,a$) is represented for comparison (+).

ramp phase due to the flat q-profiles in the core region, but the growth rate is larger. In Figure 3.14, the time evolutions of the kinetic energy corresponding to the $\mathsf{n} = 1$ mode for the reconstructed equilibria before and after the partial crash are represented with the same plot as Figure 3.10 in the case of a smaller elongation ($\kappa_a = 1.6$). The growth rate of the $\mathsf{n} = 1$ mode energy for the reconstructed equilibria before the partial crash ($t = 1.22 \times 10^5\,\tau_A$) reads $\gamma \simeq 8.5 \times 10^{-4}$ until the saturation at $t = 4.9 \times 10^4\,\tau_A$. This growth rate is about 6 times larger than the case without partial crash, represented with the green dotted line. Also, the energy saturates at $W_{sat} \sim 10^{-5}$, which is about 4 orders of magnitude larger than $W_{sat} \sim 10^{-9}$ for the case without kink with elongation $\kappa_a = 1.6$. Still, the saturated level for the partial crash is an order smaller than the reconstructed equilibrium before a full sawtooth crash.

From the set of simulations described in Table 3.1, it is shown that the increase of the $q = 1$ radius triggers partial crashes. Also, the critical $q = 1$ position depends on the plasma elongation. Hence, the plasma elongation which is used as one of the control parameters, allows the internal kink mode to become sufficiently unstable to radially displace the hot core for the case of compound sawteeth at an elongation $\kappa_a = 1.8$, in contrast to the case without partial crash at smaller elongation ($\kappa_a = 1.6$). This radial displacement of the hot core leads to a drop of the core pressure value (Figure 3.11), which induces a partial crash very similar to what is observed in experiments (Figure 3.12a).

3.4 Discussion

The reconnection model proposed by Kadomtsev [Kadomtsev, 1975][Porcelli et al., 1996] addresses scenarios with monotonic q-profiles. The model predicts that the q-profile is flat-

tened in the core region after the sawtooth crash with $q \gtrsim 1$, then q decreases below unity during the sawtooth ramp phase while the plasma recovers its initial shape. However, the magnetic topology appears to be quite complex during the recovery phase. Several theoretical models have suggested in the past that the partial reconnection or the effect of multiple $q = 1$ surfaces are responsible for the partial crash [Pfeiffer, 1985][Parail and Pereverzev, 1980][Denton et al., 1986][Aydemir et al., 1989].

In the XTOR-2F simulations of sawteeth without partial crash, the q-profile remains very flat and close to unity in the core region during the sawtooth ramp phase (Figure 3.5). Analytical studies of the ideal stability show that the internal kink mode can be unstable even for $q > 1$ in this case [Hastie and Hender, 1988][de Blank and Schep, 1991][Hastie et al., 1987]. Indeed, the study of the $\mathsf{n} = 1$ mode energy growth rate shows that the internal kink mode is unstable during the sawtooth ramp phase (Figure 3.10) although $q > 1$ at the times of interest. Also, more than one $q = 1$ surface appear due to the skin current formed at a finite radius during the ramp phase. This behavior was already observed in previous simulations of compound sawteeth using heat diffusivity that depend on the temperature or its gradient [Denton et al., 1986][Aydemir et al., 1989]. This class of transport model allows the current profile to be locally peaked in an off-axis region. Multiple q=1 surfaces appear due to the development of a hollow current density profile, and lead to a partial crash. In the present XTOR-2F simulations, the perpendicular heat diffusivity also depends on the temperature, $\chi_\perp \propto \eta$, and produces a hollow current profile during the sawtooth simulations. Thus multiple $q = 1$ surfaces and reconnection are generic during the sawtooth ramp phase following a 'full' crash. A reorganization of the magnetic surfaces is observable in the Poincaré plots (Figures 3.8-b to 3.8-f) in the region of the skin current sheet until the equilibrium is recovered. However, no pressure drop occurs in the core region during the ramp phase (Figures 3.7, 3.8-a). Hence, the presence of multiple $q = 1$ surfaces is a necessary but not sufficient condition for a partial crash.

In the compound sawtooth cycles simulated with a more elongated cross section ($\kappa_a = 1.8$, $\delta_a = 0.4$, $r_s = 0.4\,a$) or a larger inversion radius ($\kappa_a = 1.6$, $\delta_a = 0.4$, $r_s = 0.47\,a$), the internal kink mode instability has a larger growth rate due to the destabilizing effects (Figure 3.14). The internal kink mode then becomes sufficiently unstable to trigger a radial displacement of the hot core during the recovery phase. This radial displacement of the hot core leads to a substantial drop of the central pressure value (Figures 3.11 to 3.13). The amplitude of the drop is smaller than that of the full sawtooth crash, which characterizes a partial crash (Figure 3.2-b). In experiments, partial crashes with amplitudes smaller than the full sawtooth crash are frequently observed [Pfeiffer, 1985][Nagayama et al., 1996]. Also, SXR diagnostics show that the maximum emissivity point is radially displaced and remains in the core region inside the $q = 1$ surface at equilibrium during the partial crash [Janicki et al., 1990][Xu et al., 2014]. The SXR emissivity is a monotonic function of the plasma density and temperature in absence of highly radiating impurities in the plasma. This dynamics of the hot core is also observed in the 2D electron density reconstructions from the FSR measurements of the

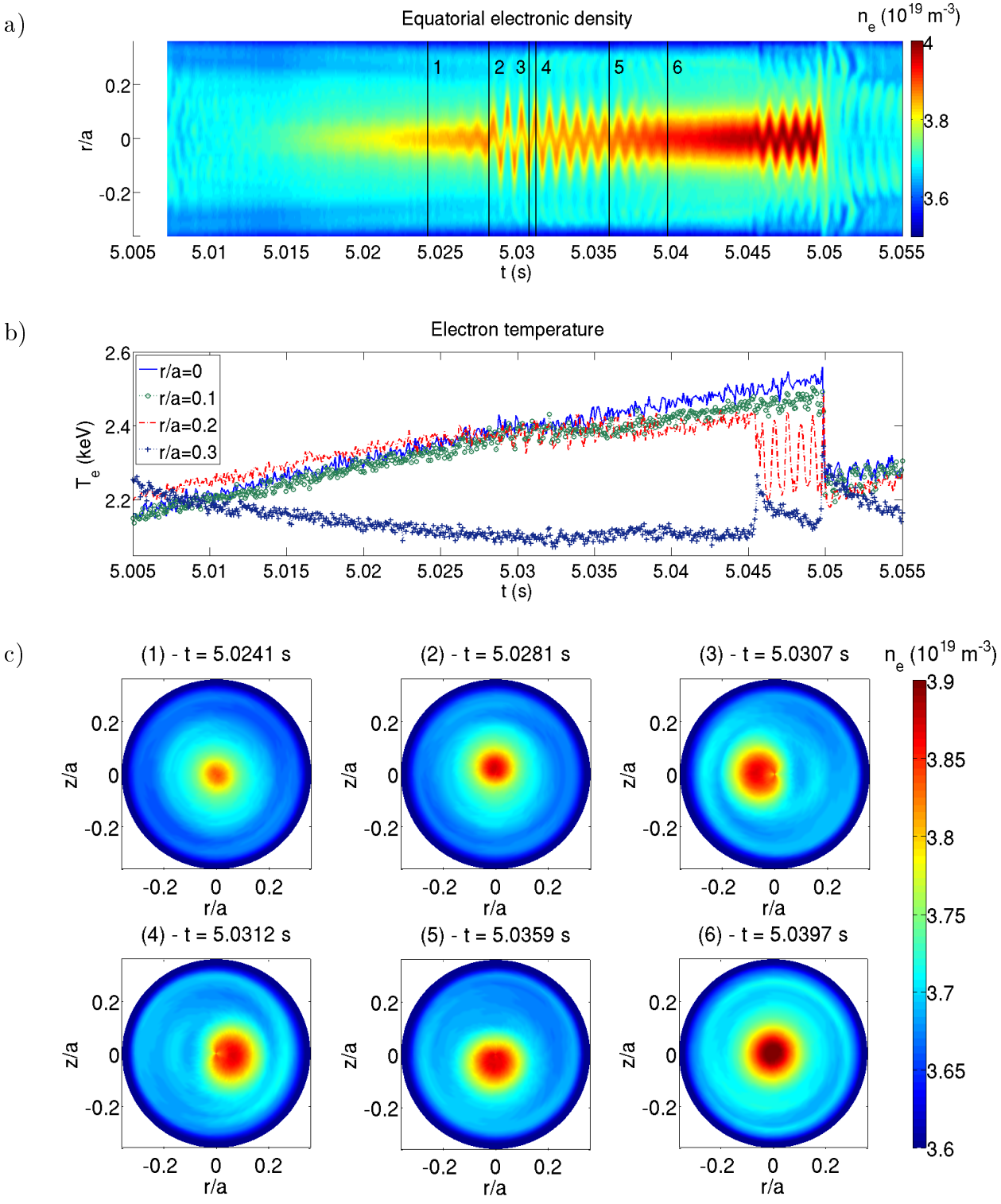

Figure 3.15: (a) FSR and (b) ECE measurements in the equatorial plane during a compound sawtooth of the Tore Supra discharge #44634. (c) The 2D electron density reconstructions in the core region, which correspond to the time points marked by vertical lines in (a), again shows that the hot core is partially expelled during the partial crash.

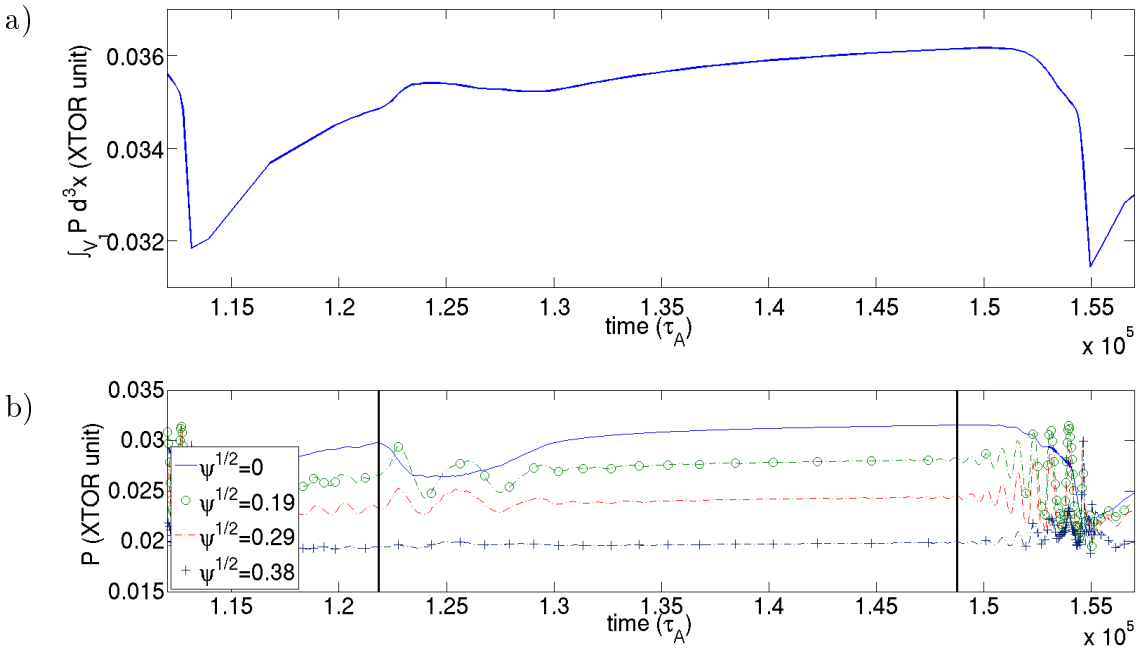

Figure 3.16: Time evolution of (a) the energy content inside the volume $\mathcal{V}_1$ delimited by the $q = 1$ surface at equilibrium and (b) the corresponding the pressure at different radii during the compound sawteeth ($\kappa_a = 1.8$, $\delta_a = 0.4$, $r_s = 0.4\,a$).

Tore Supra discharge #44634 (Figure 3.15-c). Thus, the pressure contours simulated with the XTOR-2F code are in qualitative agreement with the experimental observations using SXR tomographic inversions.

It can be remarked that the partial crash time is larger than the sawtooth full crash time. In the compound sawtooth of the Tore Supra discharge #44634 (Figure 3.15), the characteristic time of reconnection can be assimilated to the duration of the oscillating phase as measured by reflectometry. The oscillating phase during the partial crash lasts $\tau_{rec} \simeq 8\,\text{ms}$, which is larger than $\tau_{rec} \simeq 5\,\text{ms}$ for the sawtooth full crash. Also, it can be noticed that the sawtooth crash phase during the time interval $t = 5.045 - 5.05\,\text{s}$ corresponds to the 'second kind' crash according to the definition in Ref.[Udintsev et al., 2005]. In the simulated compound sawteeth (Figure 3.16), the duration for the drop of the energy content inside the $q = 1$ surface during a partial crash is $\tau_{rec} \simeq 5.5 \times 10^3\,\tau_A$, which is about 1.5 times larger than $\tau_{rec} \simeq 3.6 \times 10^3\,\tau_A$ for a full sawtooth crash. In fact, the characteristic times of sawtooth crashes τ_{rec} represents the duration needed for the energy content inside the $q = 1$ surface to be expelled, which is quantified by the integral of the pressure inside the volume delimited by the $q = 1$ surface (Figure 3.16-a). For the diagnostics with fixed measurement points the characteristic times for the crashes are deduced from the evolution of the central pressure. In this case, amplitudes of the collapse are more pronounced and the characteristic times are shorter (Figure 3.16-b) than the evolution of the energy content in the core region. Hence, the characteristic time of the energy evolution in the core region is a more relevant parameter to quantify the energy exchange due to the reconnection.

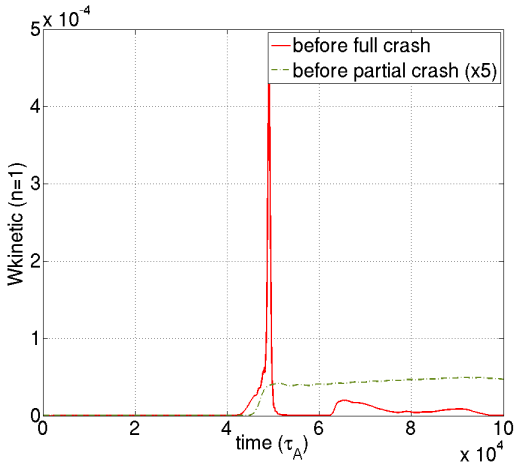

Figure 3.17: Time evolution of the kinetic energy of the $\mathsf{n} = 1$ mode from reconstructed equilibria before the partial crash at $t = 1.22 \times 10^5\,\tau_A$ (*dashed line*, multiplied by 5 for visibility) and the full crash at $t = 1.49 \times 10^5\,\tau_A$ (*solid line*). cf. Figure 3.16b

This difference of the crash times can be explained by a weaker diamagnetic effect during the sawtooth ramp phase, where the pressure gradient is small due to the preceding sawtooth full crash. Indeed, diamagnetic effects play an important role in the internal kink mode stability, thus on the island growth rate. The two-fluid effects are stabilizing the internal kink mode in the linear phase [Ara et al., 1978]. However, they are strongly destabilizing in the non-linear phase [Aydemir, 1992][Zakharov et al., 1993][Wang and Bhattacharjee, 1993]. The scan of the diamagnetic parameter $\bar{d}_i$ with the XTOR-2F code also shows that at the sawtooth crash, which is a non-linear phenomenon, the collapse time decreases as diamagnetic effects increase [Halpern et al., 2011b]. The non-linear evolution of the $\mathsf{n} = 1$ mode energy from the reconstructed equilibria corresponding to times before the partial crash ($t \simeq 1.22 \times 10^5\,\tau_A$) and the ordinary crash ($t \simeq 1.49 \times 10^5\,\tau_A$) is represented in Figure 3.17. A non-linear saturation of the $\mathsf{n} = 1$ mode occurs for the equilibrium reconstructed from a time slice before the partial crash.

This is in contrast with the time evolution of an equilibrium reconstructed before a full crash. In that case, a collapse is observed. The various saturation scenarios were investigated in Ref.[Halpern et al., 2011b]. The first evolution (partial crash) corresponds to a so-called 'saturated helical equilibrium' while the second (full crash) is identified as a sawtoothing regime. Saturated helical states are typically observed when diamagnetic stabilization is weak (small values of $\bar{d}_i$ in Ref.[Halpern et al., 2011b]) while the sawtooth regime corresponds to strong diamagnetic stabilization. This picture is also consistent with a local Lundquist number that is lower before a partial crash then before a full crash.

As a consequence, a partial crash can be interpreted as a result of a competition between the unstable internal kink mode and the diamagnetic stabilization effect during the sawtooth ramp phase.

3.5 Summary

In this chapter, compound sawteeth have been studied with the XTOR-2F code. Non-linear 3-D simulations of sawtoothing cycles show that q-profiles are flat in the core region after a sawtooth crash, with $q \gtrsim 1$. The q-profile remains flat during the beginning of the ramp phase, and becomes hollow due to a plasma that is slightly hotter between the inversion and mixing radii right after the crash. This class of q-profiles is unstable with respect to the internal kink mode, due to the low magnetic shear. The growth of the resulting weakly unstable internal kink mode leads to a localized and modest reorganization of the magnetic topology. However, no temperature drop is observed during this reorganization phase. This picture is changed when increasing the radial position of the $q = 1$ surface, which is known to be destabilizing. Above a critical $q = 1$ radius, a relaxation of the central pressure, i.e. a partial crash, is observed. The amplitude of the pressure drop is nevertheless smaller than a full crash. The pressure drop is triggered by the helical displacement of the hot core which rotates poloidally inside the $q = 1$ surface at equilibrium during the partial crash. The displaced hot core is only partially expelled out of the $q = 1$ surface at equilibrium. Partial crashes are also observed when increasing the elongation. Indeed, the critical value of the inversion radius depends on the plasma elongation. Hence, the onset of a partial crash is closely related to an overall more unstable internal kink mode. Also, it is found that the partial crash time is longer than a full crash time. This is attributed to a weaker diamagnetic stabilizing effect during the sawtooth ramp phase, due to a low pressure gradient. The onset of a partial crash is therefore understood as the conjunction of enhanced instability due to elongation and weak diamagnetic stabilization.

It is known that partial crashes are observed in circular devices such as Tokamak de Varennes or Tore Supra. So far, no partial crashes have been obtained in circular geometry with the XTOR-2F code, setting a parabolic q-profile in the initial equilibrium. This is in contrast with previous MHD simulations [Denton et al., 1986][Aydemir et al., 1989]. Differences are the initial current profiles and the heat transport model, which plays an important role to control the temperature profile, and thus the current profile. Still, several features of the simulations agree with experimental observations: radial displacement and helical rotation of the hot core during the partial crash, smaller amplitude of the pressure drop compared to a full sawtooth crash. Partial crashes are observed in Tokamak de Varennes at large values of the plasma current, therefore presumably large values of the inversion radius r_s. This picture is also consistent with the present XTOR-2F simulations. Thus, the predictive capability of the XTOR-2F code is once more verified. This will allow one to rely on the study of the impurity behaviour in sawtoothing plasmas simulated by the XTOR-2F code.

Hence, the main conclusion is that the onset of partial crash is related to the competition between the strength of the instability and diamagnetic stabilization, and is also very sensitive to the details of the q-profile after a full crash.

CHAPTER 4

Impurity behaviour in tokamak discharges

Contents

Metallic impurities resulting from plasma-wall interaction are always present even in small quantities. Indeed, they may be produced by plasma facing components (PFCs) due to sputtering (e.g. C, Mo or W), radio-frequency (RF) antennas (e.g. Fe, Ni or Cu) and diagnostic elements. Particularly, tungsten ($\mathcal{Z}_W = 74$) has been identified as the best candidate for the ITER divertor thanks to its capability to handle large heat fluxes and avoid tritium retention [Kaufmann and Neu, 2007][Pitts et al., 2011]. In addition to metallic impurities, gases such as Ar or Ne are intentionally seeded into the plasma as a potential solution to mitigate edge-localized modes (ELMs) at pedestal region [Strachan et al., 2000] and reduce heat loads on PFCs.

Impurities in core plasmas not only dilute the D-T fuel, but may also radiate significant amounts of energy. The total radiated power is one of the main components of the power balance of a tokamak discharge. It dictates the final energy content for given heat sources and confinement time. Severe limitations on tolerable concentrations are imposed for high $\mathcal{Z}$ impurities as they drastically cool down the core region even in a small concentration [Noda

et al., 1997]. When this limit is exceeded, the core plasma loses more energy by radiation than it gains from heating, and this leads to a radiative collapse [Ongena et al., 2004]. In the particular case of tungsten, tokamak operation is jeopardized when its concentration N_W/N_e is above 10^{-4} [Pütterich et al., 2010]. Hence, it is crucial to understand how impurities are transported in tokamak plasmas. In general, intrinsic impurities are stationary or evolve with the bulk plasma. It is then difficult to determine impurity transport coefficients. Therefore, for impurity transport studies, trace impurities are injected in the plasma by gas puff for gas impurities, or laser blow-off (LBO) for metallic impurities.

Dedicated experimental campaigns were held in ASDEX-Upgrade and TCV. The objective of the discharges was to investigate heavy impurity transport in the presence of sawteeth and the effects of electron cyclotron (EC) waves on controlling its accumulation. In this chapter, the principle of soft X-ray (SXR) measurements and tomographic inversions, which are mainly used to trace impurities, are briefly introduced in Section 4.1. Then, different discharge scenarios performed to investigate the impurity behaviour are presented in Section 4.2.2. Several discharges among the performed scenarios are analysed in Section 4.2.3 to deduce different impurity behaviour depending on the experimental set-up. Finally, possible explanations to the observations are discussed in Section 4.2.5.

4.1 Impurity tracing in experiments

4.1.1 Radiation in the core plasmas

It is necessary to know the spatial distribution of the radiation in order to assess the impurity behaviour in the core plasma. Impurities are ionized in the plasma edge. Charged particles radiate in the plasma through *bremsstrahlung*, radiative recombination, dielectronic recombination, line radiation. Details on different radiative processes can be found in Ref.[Vezinet, 2013].

Light impurities (e.g. Be, C or N) are fully ionized in a tokamak core plasma. However, several tokamaks have now metallic plasma-facing components. Plasmas are thus contaminated by heavier impurities (e.g. Fe, Cu, Mo or W) which are not fully stripped in most of the plasma volume. The atomic physics for such ions is more complicated than for light ions. Therefore, emission coefficients associated with each process are calculated numerically and stored in databases (e.g. ADAS[1]).

In general, the total emissivity of a species a of density N_a can be written as

$$\mathcal{E}_a = N_e N_a \sum_{k=0}^{Z_a} f_{a,k} \left(K_{a,k}^{ff} + K_{a,k}^{fb} + K_{a,k}^{bb} \right) \tag{4.1}$$

Here, $N_a = \sum_k N_{a,k}$ is the total density of species a in the plasma volume, with $N_{a,k}$ the

[1] Atomic Data and Analysis Structure (see http://www.adas.ac.uk/)

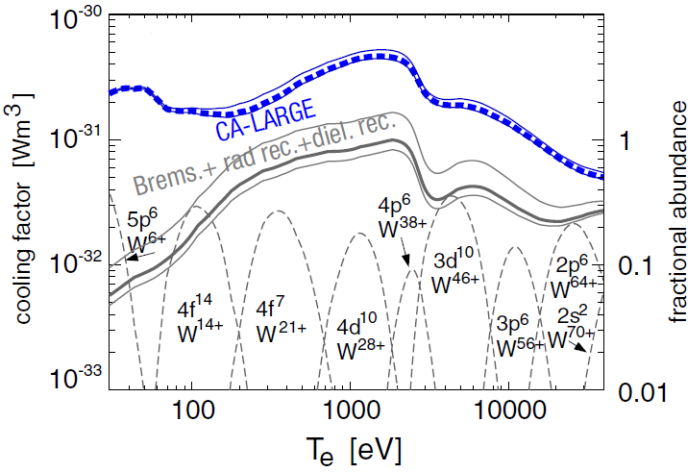

Figure 4.1: The cooling factor (*blue dashed line*) and fractional abundance (*gray dashed lines*) of tungsten as a function of electron temperature. Contributions of emission process other than line radiation is plotted for information (*gray solid line*). This figure is taken from Ref.[Pütterich et al., 2010], where details on computations can be found.

density of its ionization state k. A fractional abundance $f_{a,k}$ is then defined as $f_{a,k} = N_{a,k}/N_a$. The quantities $K^{ff}_{a,k}$, $K^{fb}_{a,k}$ and $K^{bb}_{a,k}$ are the emission rate coefficients resulting from free-free, free-bound, bound-bound interactions respectively, for an ionization state k. Approximate analytic expressions of these coefficients are summarized in Refs.[Ingesson, 1995][Vezinet, 2013].

Since numerous ionization states exist at the same temperature for heavy ions, it is more practical to regroup fractional abundances of different ionization states and their corresponding emission coefficients in a total cooling factor $\mathcal{L}_a$. It has been shown that the effect of transport on the ionisation balance is small for heavy elements [Vezinet et al., 2014]. As an example, the cooling factor computed for tungsten [Pütterich et al., 2010] is shown in Figure 4.1. The total emissivity then has a simpler form

$$\mathcal{E}_a = N_e N_a \mathcal{L}_a(T_e) \tag{4.2}$$

It can be noticed that the cooling factor is a function of the electron temperature T_e. Therefore, the spatial distribution of a species a can be deduced from its measured emissivity distribution knowing the electron density and temperature. However, an important amount of impurities might cool down the plasma by radiation and affect the bulk plasma properties. Therefore, only a trace of metallic impurities is injected by LBO.

4.1.2 Soft X-ray diagnostics

Measurements of radiation

In experiments, bolometer measurements are used to estimate the total plasma radiated power [Huber et al., 2007][Ingesson et al., 2008]. However, they are often dominated by radiation at the plasma edge and near the limiter or divertor. Therefore, the radiated power

due to impurities in the core is difficult to extract from bolometer measurements. Otherwise, spectroscopy provides valuable information on ions from line-integrated measurements with high spectral resolution. In particular, charge-exchange recombination spectroscopy (CXRS) diagnostics provide local measurements from which light impurity (up to Ar) densities in the core can be deduced. It is usually used in connection with neutral beam injection [Boileau et al., 1989]. However, most spectroscopy diagnostics lack spatial sampling due to a limited number of lines of sight.

As a compromise, a diagnostic with poorer spectral resolution but high spatial and temporal resolution is a useful complement to the lack of spatial and/or temporal resolution of some spectroscopy diagnostics. Soft X-ray (SXR) diagnostics in tokamaks usually detect photons with energy in the approximate range from 1 keV to 20 keV. Its measurements are spectrally-integrated quantities compensated by good time and spatial resolution. A tomographic reconstruction of the total emissivity can then be performed in a poloidal cross-section thanks to a large number of lines of sight (Figure 4.2). In addition, the SXR emissivity is not only dependent on electron temperature and density but also on impurity densities [Hutchinson, 1987][de Michelis and Mattioli, 1981]. Therefore, tomographic inversions of SXR measurements can deliver local values of the plasma SXR emissivity which is proportional to impurity densities.

These features make the SXR diagnostics complementary to spectroscopy in that they provide information about MHD instabilities and impurity transport in core plasmas.

Soft X-ray detection method

The most common SXR detectors are semi-conducting diodes which are placed behind a pin hole to form just as many lines of sight. Each detector views a plasma volume with a certain solid angle, on which SXR emissivity is integrated. In tokamak tomography, the cone is commonly considered 'thin' enough so that the volume integral can be approximated to a line integral. A discussion on limitations and justifications of this approximation is detailed in Ref.[Ingesson et al., 1999]. More sophisticated algorithms are used in order to take into account the exact geometry of the lines of sight [Vezinet, 2013].

A beryllium filter is installed in front of each detector set acting as a high-pass filter. Saturation of signals is prevented by varying thickness of Be filters. It typically ranges between 25 μm and 200 μm. The measured signals are spectrally and spatially-integrated data. In a poloidal cross-section described by the (R,Z) coordinates, the signal measured by each line of sight l can be written as

$$y_l = \int_{h\nu \in \mathsf{E}_l} \mathrm{d}\nu \int_{\mathsf{R},\mathsf{Z}} \mathcal{E}_\nu(\mathsf{R},\mathsf{Z}) \mathrm{d}s_l(\mathsf{R},\mathsf{Z}) \tag{4.3}$$

where E_l is the energy range of the measured signal and $\mathrm{d}s_l$ is the unit length of the line of sight.

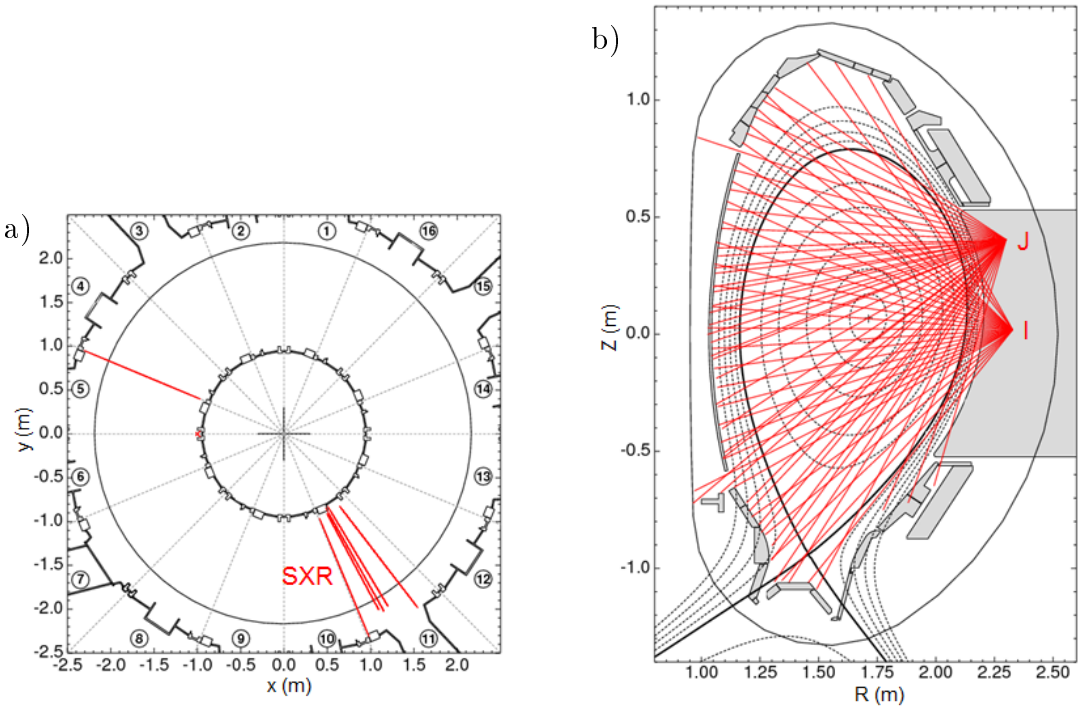

Figure 4.2: Lines of sight of the SXR detectors in a) toroidal and b) poloidal cross-sections. In a), the lines of sight of SXR cameras H, I, J, K, L, M, F are shown. Only those of cameras I and J are represented in b) for visibility. An example of magnetic flux surfaces computed by EFIT is shown in b). The last closed flux surface (LCFS) is shown in bold solid line.

Figure 4.2 shows the lines of sight of SXR detectors installed in ASDEX-Upgrade. Thanks to a sufficient number of lines of sight and projections, a 2-D SXR emissivity map can be reconstructed with tomographic inversion. Such tomographic inversion is now routinely available on most tokamaks [Mazon et al., 2012].

4.1.3 Tomographic reconstruction

Tomographic inversion : an ill-posed problem

A tomographic inversion consists in recovering the initial shape of an object from detected signals which are integrals of the plasma emission along the different lines of sight. This method is widely used in different fields (e.g. geophysics, medical imaging, etc.), and particularly in fusion research, to diagnose tokamak plasmas. For SXR diagnostics, the 'object' to be reconstructed is the spatial distribution of local emissivity. In a poloidal cross-section described by (R, Z) coordinates, the local emissivity can be represented as a function $\mathcal{E}_0(\mathsf{R}, \mathsf{Z})$. For an equipment with N_L lines of sight, the tomography problem consists in resolving the system

$$y_l = \int \mathcal{E}_0(\mathsf{R}, \mathsf{Z}) \mathrm{d}s_l \tag{4.4}$$

for each $1 \leq l \leq N_L$, where y_l is the line-integrated power detected, s_l is the curvilinear abscissa of the line of sight. This system of equations which is known as the Fredholm

integral equations of the first kind [Twomey, 1963], is always under-determined. Indeed, an infinite number of y_l would be needed to determine exactly the initial $\mathcal{E}_0(\mathsf{R},\mathsf{Z})$. However, the number of lines of sight is usually limited to less than 200 in tokamaks, as a result of a trade-off between various operational factors (e.g. available space, price *etc.*).

One solution to the tomography problem is to reduce degrees of freedom by writing the solution as a series of orthogonal functions. An example of basis functions is found by expanding the solution's poloidal component into a Fourier series and its radial component into a series of Zernike polynomials [Cormack, 1964]. This method was used in the past for the SXR tomography, for example, in Alcator C-Mod [Camacho and Granetz, 1986] and JET [Granetz and Smeulders, 1988]. Another possibility is to divide the poloidal cross-section into a finite element grid on which the emissivity is reconstructed. The size of the pixels has to be small enough so that the emissivity can be considered as constant, but at the same time, not too small as it defines the number of unknowns. Shapes for the pixels are not restricted to rectangular pixels. The method described in this section is the one used for analysing the ASDEX-Upgrade discharge that will be discussed in the following sections.

In a matrix format, the system of equations (4.4) is written as

$$\mathbf{X} * \boldsymbol{\mathcal{E}}_0 = \mathbf{y} \tag{4.5}$$

where $*$ denotes the usual matrix multiplication. The matrix $\mathbf{X}$ is an integral operator where information on the geometry of every line of sight in the poloidal cross-section grid is regrouped. The size of the matrix $\mathbf{X}$ is $N_L \times N_p$, where N_p is the total number of pixels used to subdivide the poloidal cross section. The emissivity distribution is represented by the vector $\boldsymbol{\mathcal{E}}_0$ of length N_p. The vector $\mathbf{y}$ has N_L elements which correspond to the line integrated values for each line of sight.

The inversion of the matrix $\mathbf{X}$ is in practice intractable. This is mainly due to the fact that the system has a lot more unknowns N_p than equations N_L. Even if there is a large number of lines of sight so that $N_L = N_p$, the matrix X is ill-conditioned. Hence, a solution $\boldsymbol{\mathcal{E}}$ has to be chosen among the infinity of solutions to the under-determined problem. The parameter χ^2, defined as

$$\chi^2 = (\mathbf{X} * \boldsymbol{\mathcal{E}} - \mathbf{y})^T * (\mathbf{X} * \boldsymbol{\mathcal{E}} - \mathbf{y}) = \|\mathbf{X} * \boldsymbol{\mathcal{E}} - \mathbf{y}\|_2^2 \tag{4.6}$$

where the exponent T denotes a matrix transposition and $\|.\|_2$ denotes the Euclidean norm, gives the quadratic measure of the mismatch between the solution found $\boldsymbol{\mathcal{E}}$ and the expected solution $\boldsymbol{\mathcal{E}}_0$, which corresponds to the initial object.

Methods for regularization

An infinite number of solutions $\boldsymbol{\mathcal{E}}$ gives $\chi^2 = 0$, but they are mostly erroneous solutions resulting from an over-fit. Therefore, to obtain the closest solution $\boldsymbol{\mathcal{E}}$ to the expected solution

$\boldsymbol{\mathcal{E}}_0$, the relevant quantity to minimize is the functional Φ, defined as

$$\Phi = \frac{1}{2}\chi^2 + \lambda R \tag{4.7}$$

Here, R is a regularizing functional reflecting the expected properties of the physical solution $\boldsymbol{\mathcal{E}}_0$ (e.g. continuity, derivability, smoothness, *etc.*). The regularization parameter λ determines the weighting between the minimization of χ^2 and the satisfaction of conditions imposed by the functional R. Hence, to solve a tomography problem : first, appropriate functional R and parameter λ are chosen, then, a solution $\boldsymbol{\mathcal{E}}$ for the corresponding λ is computed.

The functional R can be built according to the Tikhonov regularization method [Tikhonov, 1963]. A solution $\boldsymbol{\mathcal{E}}$ of the Tikhonov regularization verifies the relation

$$\left(\mathbf{X}^T * \mathbf{X} + \lambda \mathbf{H}\right) * \boldsymbol{\mathcal{E}} = \mathbf{X}^T * \mathbf{y} \tag{4.8}$$

where $\mathbf{H}$ is a regularization matrix associated to R with the relation $R = \boldsymbol{\mathcal{E}}^T * \mathbf{H} * \boldsymbol{\mathcal{E}}$. As soon as the regularization matrix has been chosen, the "L-curve" method can be used to find the optimum regularization parameter λ [Hansen, 2001].

A linear regularization of n-th order consists in defining the matrix $\mathbf{H}$ as $\mathbf{H} = \mathbf{L}^T * \mathbf{L}$, where the matrix $\mathbf{L}$ represents a n-th order spatial derivative. For example, the simplest form of the matrix $\mathbf{L}$ for the linear regularizations of 0-th, 1-st and 2-nd order would be respectively the identity matrix $\mathbf{I}$, the gradient matrix $\boldsymbol{\nabla}$ and the laplacian matrix $\boldsymbol{\Delta}$. Hence, the corresponding functional R requires a solution such that respectively the Euclidean norm, the gradient and the curvature are minimum.

For the SXR diagnostics in ASDEX-Upgrade, the minimum Fisher regularization (MFR) algorithm is used [Odstrcil et al., 2015]. The MFR algorithm was first introduced in [Anton et al., 1996], and has a similar principle to the linear regularization, but the requirement for the solution $\mathcal{E}$ is the minimization of Fisher information $\mathcal{I}_F$ defined as

$$\mathcal{I}_F = \int \frac{\mathcal{E}'(\zeta)}{\mathcal{E}(\zeta)} d\zeta \tag{4.9}$$

where ζ is a spatial variable and the prime stands for the derivative with respect to ζ. This constraint allows the algorithm to find a solution with inhomogeneous smoothing. Indeed, a stronger smoothing is applied in low emissivity regions. Thus, structures of high emissivity, usually located in the core plasmas, are recovered more efficiently than with linear regularization methods. In a matrix format, the iterative process of the MFR algorithm has three main steps. Every p-th iteration :

- First, a diagonal matrix $\mathbf{W}^{(p)}$ which contains preponderation of pixels for the Fisher information, is defined as

$$W_{ij}^{(p)} = \begin{cases} \delta_{ij} & \text{for } p = 0 \\ \delta_{ij}/\mathcal{E}_i^{(p)} & \text{for } p > 0 \end{cases} \tag{4.10}$$

with $1 \leq i \leq N_L$, $1 \leq j \leq N_L$ and δ_{ij} the Kronecker delta.

- Second, the regularizing matrix $\mathbf{H}^{(p)}$ is calculated. Here, the linear regularization of 1-st order is chosen as an example.

$$\mathbf{H}^{(p)} = \boldsymbol{\nabla}^T * \mathbf{W}^{(p)} * \boldsymbol{\nabla} \tag{4.11}$$

- Finally, the system is solved with the Tikhonov regularization method

$$\left(\mathbf{X}^T * \mathbf{X} + \lambda^{(p)}\mathbf{H}^{(p)}\right) * \boldsymbol{\mathcal{E}}^{(p+1)} = \mathbf{X}^T * \mathbf{y} \tag{4.12}$$

In general, there are little differences between $\boldsymbol{\mathcal{E}}^{(p)}$ and $\boldsymbol{\mathcal{E}}^{(p+1)}$ after a few iterations (typically below 5 iterations). Hence, the MFR is adapted for real-time analysis of discharges [Mazon et al., 2012]. Also, the MFR method is shown to be efficient, in terms of precision and numerical costs, compared to linear regularizations and the maximum entropy (ME) method [Anton et al., 1996].

In tokamaks, plasma emissivity gradients are expected to be low along the magnetic surfaces. Optimum solutions for tokamak plasmas are thus those obtained by smoothing emissivities preferentially along magnetic flux surfaces [Ingesson et al., 1998][Odstrcil et al., 2012]. For this method, the magnetic equilibrium is supposed to be known. The regularization matrix $\mathbf{H}$ then reads

$$\mathbf{H} = \mathsf{S}(\varsigma)\boldsymbol{\nabla}_{\parallel}^T * \mathbf{W} * \boldsymbol{\nabla}_{\parallel} + \mathsf{S}(-\varsigma)\boldsymbol{\nabla}_{\perp}^T * \mathbf{W} * \boldsymbol{\nabla}_{\perp} \tag{4.13}$$

where $\mathsf{S}(x) = 1/(1+e^{-x})$ for $x \in \mathbb{R}$, is a logistic sigmoid function. The matrices $\boldsymbol{\nabla}_{\parallel}$ and $\boldsymbol{\nabla}_{\perp}$ represent respectively the gradients along and across magnetic surfaces. A positive value of ς gives more weight to smoothness along magnetic surfaces. However, artificial patterns along magnetic surfaces are obtained for a high value of ς. Hence, a trade-off on the value of ς is necessary to take into account the anisotropic smoothing. For the following analysis of ASDEX-Upgrade discharges, this tomographic inversion method is applied to the SXR diagnostic of which different lines of sight are represented in Figure 4.2.

4.2 ASDEX-Upgrade measurements

4.2.1 Motivation

The electron cyclotron resonance heating (ECRH) deposition in the core plasma is found to control central impurity accumulation and thus is routinely used in experiments [Dux et al., 2003][Puiatti et al., 2006][Leigheb et al., 2007]. Numerical computations show that the impurity pinch velocity is directed outwards when the electron temperature gradients are large [Angioni and Peeters, 2006].

When a $q = 1$ surface is present in the central region of tokamak plasmas, ECRH triggers a strong MHD activity, typically an internal kink mode with mode numbers $(\mathsf{m}, \mathsf{n}) = (1, 1)$. The shape of the sawtooth cycles is then modified [Furno et al., 2001][Bierwage et al., 2015]. During the recovery phase, the hot core rotates in the poloidal direction until the next crash. It is usually called 'saturated (1,1) mode'. Also, the relative positions of the ECRH deposition radius and the $q = 1$ radius are shown to change the sawtooth period [Pietrzyk et al., 1999][Angioni et al., 2003][Chapman et al., 2012]. Thus, the ECRH located in the core plasma also modifies the overall shape and period of sawteeth.

The modified sawtooth dynamics affects the impurity transport in the core region [Sertoli et al., 2015a]. The physical reasons for the effectiveness of ECRH in mitigating tungsten accumulation or its connection with MHD activity are still unclear. In view of ITER operation with a tungsten divertor, it is vital to understand if sawtooth tailoring to prevent impurity accumulation should be rethought. We have thus designed a series of experiments in the ASDEX-Upgrade tokamak aiming at explaining the various forms of sawtooth activity and their parametric dependences.

4.2.2 Experimental set-ups

A series of discharges in ASDEX-Upgrade is designed and performed in order to study the role of the EC power. In this section, 3 of these H-mode ASDEX-Upgrade discharges, #31114, #32409 and #32410, are analysed. A gyrotron can either heat electrons or drive current, depending on the angle of the EC beam with respect to the plasma current. Indeed, if the beam is injected perpendicularly to the plasma current, the gyrotron beam heats the electrons. Otherwise, it mainly drives current. An ECCD deposition is called 'co-current' if the gyrotron beam is injected in the direction of the toroidal plasma current, and 'counter-current' if the injection is in the opposite direction. The main idea of these discharges was to use gyrotrons to heat the plasma (ECRH) near the magnetic axis ($\rho_{RF} \simeq 0.1$) to prevent impurity accumulation and drive current (ECCD) in order to trigger the (1,1) mode by directly modifying the magnetic shear. Different sawtooth shapes are obtained by scanning the ECCD deposition radius ρ_{RF} throughout the discharges. The impurity behaviour dependence on sawtooth shapes is studied.

A summary of auxiliary power sources used in these discharges is shown in Table 4.1. Detailed scenarios are presented in the following paragraphs.

ASDEX-Upgrade discharge #31114

In the discharge #31114, a total of 7.5 MW of NBI heating and 1.4 MW of EC waves is injected (Figure 4.3-a). Two gyrotrons are used in this scenario, each providing 0.7 MW. One gyrotron is used for heating and the other gyrotron drives EC current (co-current). The time evolution of the deposition radius ρ_{RF} for each EC beam is shown in Figure 4.3-b. The ECRH deposition radius is maintained at $\rho_{RF} \simeq 0.2$ throughout the discharge, in order to

discharge no.	NBI (MW)	Gyrotron	ρ_{inv}
31114	7.5	0.7 MW of ECRH and 0.7 MW of ECCD	0.35
32409	7.5	1.0 MW of ECRH ($t < 2.5$ s) then 0.2 MW of ECCD ($t > 2.5$ s)	0.35
32410	7.5	1.0 MW of ECRH ($t < 2.5$ s) then 0.4 MW of ECCD ($t > 2.5$ s)	0.35

Table 4.1: Auxiliary power sources injected in ASDEX-Upgrade discharges #31114, #32409 and #32410. The inversion radii measured from the electron temperature profiles are approximatively $\rho_{inv} \simeq 0.35$.

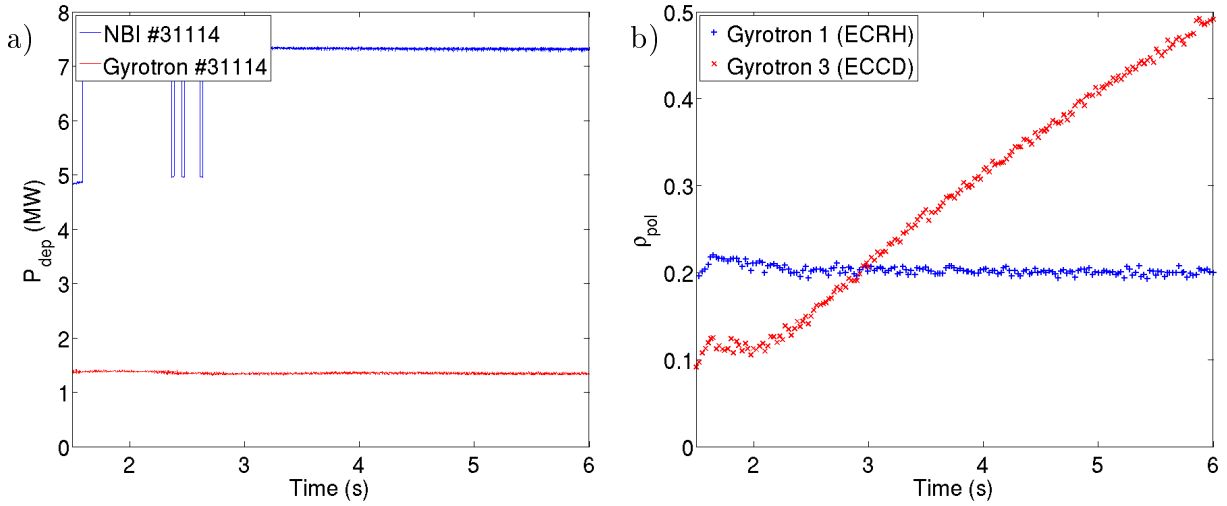

Figure 4.3: a) Auxiliary power in the ASDEX-Upgrade discharge #31114. A total power of 7.5 MW of NBI heating and 1.4 MW of EC waves is injected in the plasma. b) Deposition radii of the 2 gyrotrons used during the discharge #31114. One gyrotron is used for heating and the other for current drive with 0.7 MW per gyrotron.

prevent impurity accumulation in the plasma core. Meanwhile, the radial position ρ_{RF} of the ECCD beam is scanned from the core to the outer region.

The inversion radius ρ_{inv} can be measured from the evolution of the electron temperature profile during sawtooth crashes. In this discharge, it is located at $\rho_{inv} \simeq 0.35$. This is close to the $q = 1$ radius computed by the equilibrium reconstruction with the CLISTE code [McCarthy et al., 1999]. Thus, the ECCD deposition radius is scanned from the interior to the outer region of the $q = 1$ radius.

ASDEX-Upgrade discharges #32409 and #32410

The effect of EC waves is illustrated by the discharges #32409 and #32410. These two scenarios are the same except for the injected gyrotron power. In both discharges, a total of 7.5 MW of NBI heating is injected (Figure 4.4-a). As shown in Figure 4.4-b, a sweep of the ECCD deposition radius ρ_{RF} is made from the core to the edge, while crossing the $q = 1$ radius, similarly to the discharge #31114.

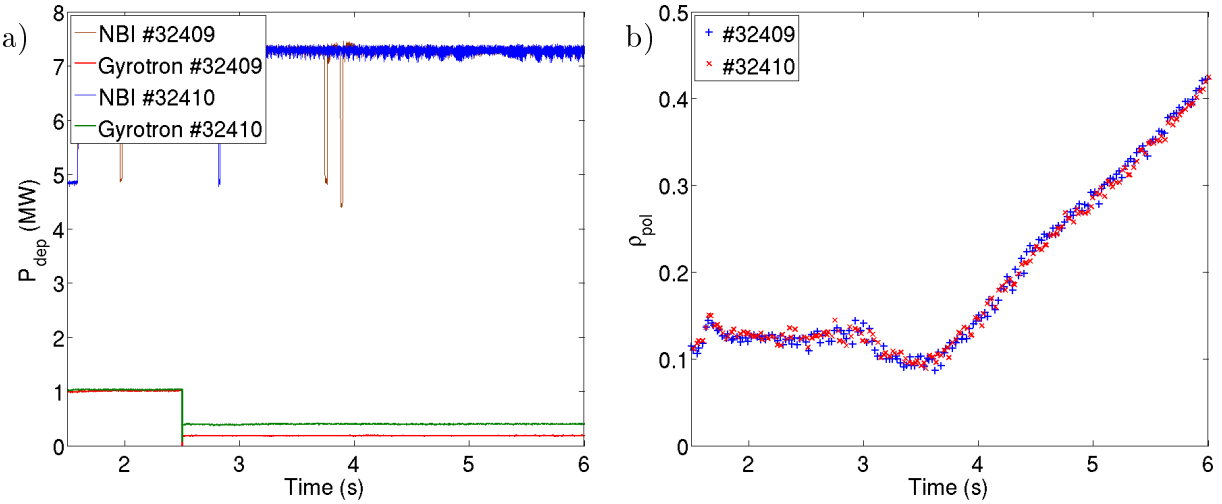

Figure 4.4: a) Auxiliary power in ASDEX-Upgrade discharges #32409 and #32410. For both discharges, 7.5 MW of NBI heating is injected. The gyrotron power after $t = 2.5$ s is 0.2 MW and 0.4 MW for the discharges #32409 and #32410 respectively. b) ECCD deposition radius ρ_{RF} during the ASDEX-Upgrade discharges #32409 and #32410.

A total of 1 MW of ECRH is injected in the core region at $\rho_{RF} \simeq 0.1$ until $t = 2.5$ s, in order to prevent impurity accumulation in the center and to avoid a disruption before the ramp-up is completed. Then from $t > 2.5$ s on, heating is turned off and is replaced by 0.2 MW of co-ECCD for the discharge #32409, and 0.4 MW for #32410.

Evaluation of impurity density from measurements

It is necessary to evaluate a 2-D map of the tungsten density, in order to investigate its behaviour during MHD instabilities. The 2-D SXR emissivity map is reconstructed by the tomographic inversion method described in Section 4.1.3. The SXR emissivity of tungsten can be isolated by subtracting the background plasma contribution. However, the contributions of each ionisation state cannot be disentangled as the measured SXR signal is the sum of the emissivity of all species in the plasma. Therefore, in the method described above, tungsten is considered as an ion with an effective electric charge

$$Z_{W,eff} = \sum_{k=0}^{Z_W} k f_{W,k}$$

where $f_{W,k}$ is the fractional abundance of the ionization state k.

The 2-D electron density distribution is evaluated from fast-sweep reflectometry measurements [Sabot et al., 2006]. In addition, a method for the reconstruction of the time dependent 2-D electron temperature map from 1-D ECE measurements has been developed in ASDEX-Upgrade [Sertoli et al., 2013]. Thus, the overall concentration of tungsten is evaluated combining SXR, electron density and temperature measurements, using the cooling

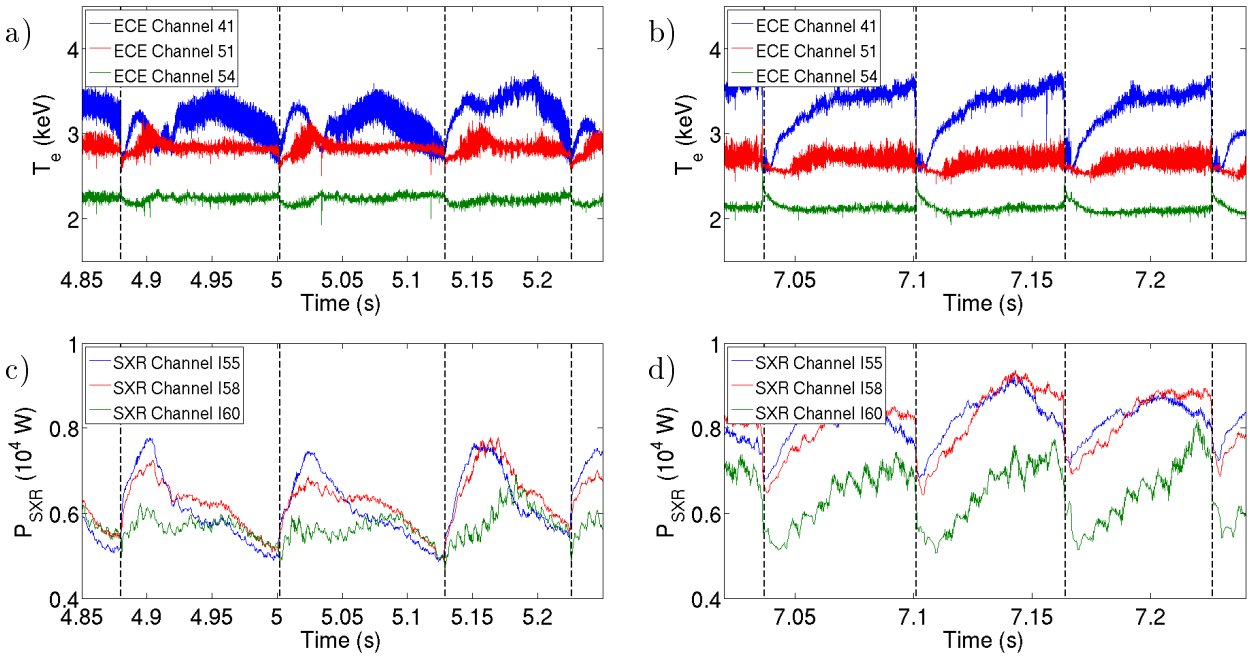

Figure 4.5: The a-b) electron temperature and c-d) line-integrated SXR measurements of the ASDEX-Upgrade discharge #31114 during the time intervals $4.85\,\mathrm{s} < t < 5.25\,\mathrm{s}$ and $7.02\,\mathrm{s} < t < 7.24\,\mathrm{s}$, where the ECCD deposition is at $\rho_{RF} \simeq \rho_{inv}$ and $\rho_{RF} > \rho_{inv}$ respectively. The displayed measurements correspond to $\rho_{pol} \simeq 0$ (*blue*), $\rho_{pol} \simeq 0.2$ (*red*) and $\rho_{pol} \simeq 0.4$ (*green*) (cf. Figure 4.6-a). Sawtooth crashes are marked with dashed vertical lines.

factor as shown in Figure 4.1

$$N_W(\rho,\theta,t) \propto \frac{\mathcal{E}^{SXR}(\rho,\theta,t)}{N_e(\rho,\theta,t)\mathcal{L}_W^{SXR}(T_e(\rho,\theta,t))} \tag{4.14}$$

4.2.3 Effect of ECCD deposition radius

Impurity flush out from the hot core in presence of a saturated (1,1) mode

The ASDEX-Upgrade discharge #31114 is analysed in this section. Especially, two time intervals corresponding to two different ECCD deposition radii ρ_{RF} with respect to the inversion radius $\rho_{inv} \simeq 0.35$ are studied :

- $4.85\,\mathrm{s} < t < 5.25\,\mathrm{s}$, where $\rho_{RF} \simeq \rho_{inv}$
- $7.02\,\mathrm{s} < t < 7.24\,\mathrm{s}$, where $\rho_{RF} > \rho_{inv}$

In Figure 4.5, the electron temperature and SXR measurements are displayed at different radii (Figure 4.6-a). The measurements made near the magnetic axis ($\rho_{pol} \simeq 0$), inside the $q = 1$ surface ($\rho_{pol} \simeq 0.2$) and outside the $q = 1$ surface ($\rho_{pol} \simeq 0.4$) are shown in blue, red and green respectively. It should be noted that the SXR measurements shown in Figure 4.5-c,d are integrated values along the lines of sight which are tangential to the respective flux surfaces.

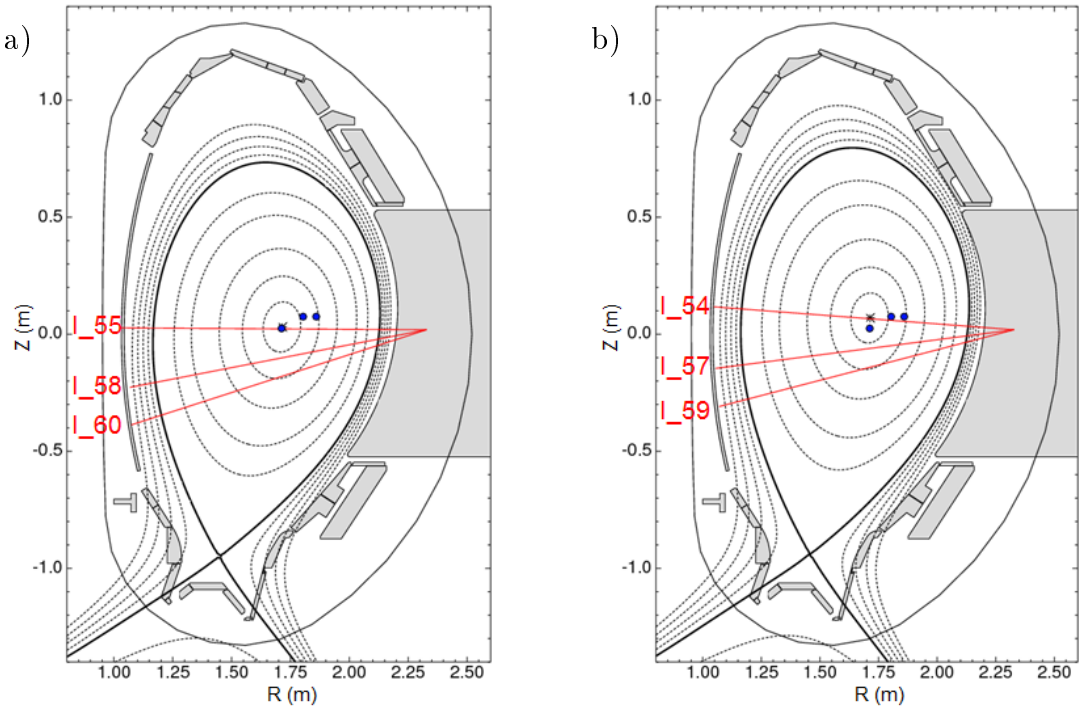

Figure 4.6: Lines of sight of the SXR detectors (*red lines*) and ECE channels (*blue dots*) of which measurements are shown in Figures 4.5 and 4.13. The equilibria which correspond to ASDEX-Upgrade discharges a) #31114 at $t \simeq 5.0\,\mathrm{s}$ and b) #32409 at $t \simeq 2.5\,\mathrm{s}$ are shown in the background. The displayed magnetic flux surfaces (*dashed lines*) from the magnetic axis (+) to the separatrix (*bold lines*) correspond to $\rho_{pol} = 0.2$, 0.4, 0.6, 0.8 and 0.9 respectively.

A change of sawtooth shape depending on the position of ECCD is seen in the ECE measurements (Figure 4.5-a,b). Indeed, so-called 'humpback' sawteeth with a period of about 120 ms are observed when the ECCD deposition is located near the $q = 1$ surface. However, sawteeth have an ordinary shape with an approximate period of 70 ms when $\rho_{RF} > \rho_{inv}$. These modifications are visible in the SXR measurements (Figure 4.5-c,d). Meanwhile, the dynamics of the impurity can be roughly estimated from integrated SXR signals.

The 2-D impurity density map is recovered from the SXR lines of sight, electron density and temperature measurements as explained in Section 4.2.2 and detailed in Ref.[Sertoli et al., 2015b]. This method is applied when the internal kink mode saturates at $t \simeq 4.982\,\mathrm{s}$, where $\rho_{RF} \simeq 0.38$ (Figure 4.3-b). The ECCD deposition is then close to the inversion radius $\rho_{inv} \simeq 0.35$. Figure 4.7-a shows the 2-D electron temperature map reconstructed from the ECE measurements. The 2-D isothermal surfaces show that the hot core is located near the magnetic axis at the beginning of the sawtooth cycle ($t_1 \simeq 4.882\,\mathrm{s}$). This unperturbed state is considered as a reference to determine the effects due to the $(1,1)$ mode. The variation of T_e with respect to this state $\Delta T_e(t) \equiv T_e(t) - \langle T_e(t = t_1) \rangle$ where the brackets $\langle \cdot \rangle$ represent a flux surface average, is shown in Figure 4.7-b. The displaced hot core and the island that forms due to reconnection are clearly visible in this figure. It is observed that the displaced hot core remains inside the inversion radius marked by thick white lines, and rotates in the poloidal direction. A dark spot in the 2-D SXR emissivity map (Figure 4.7-c) can be observed, and

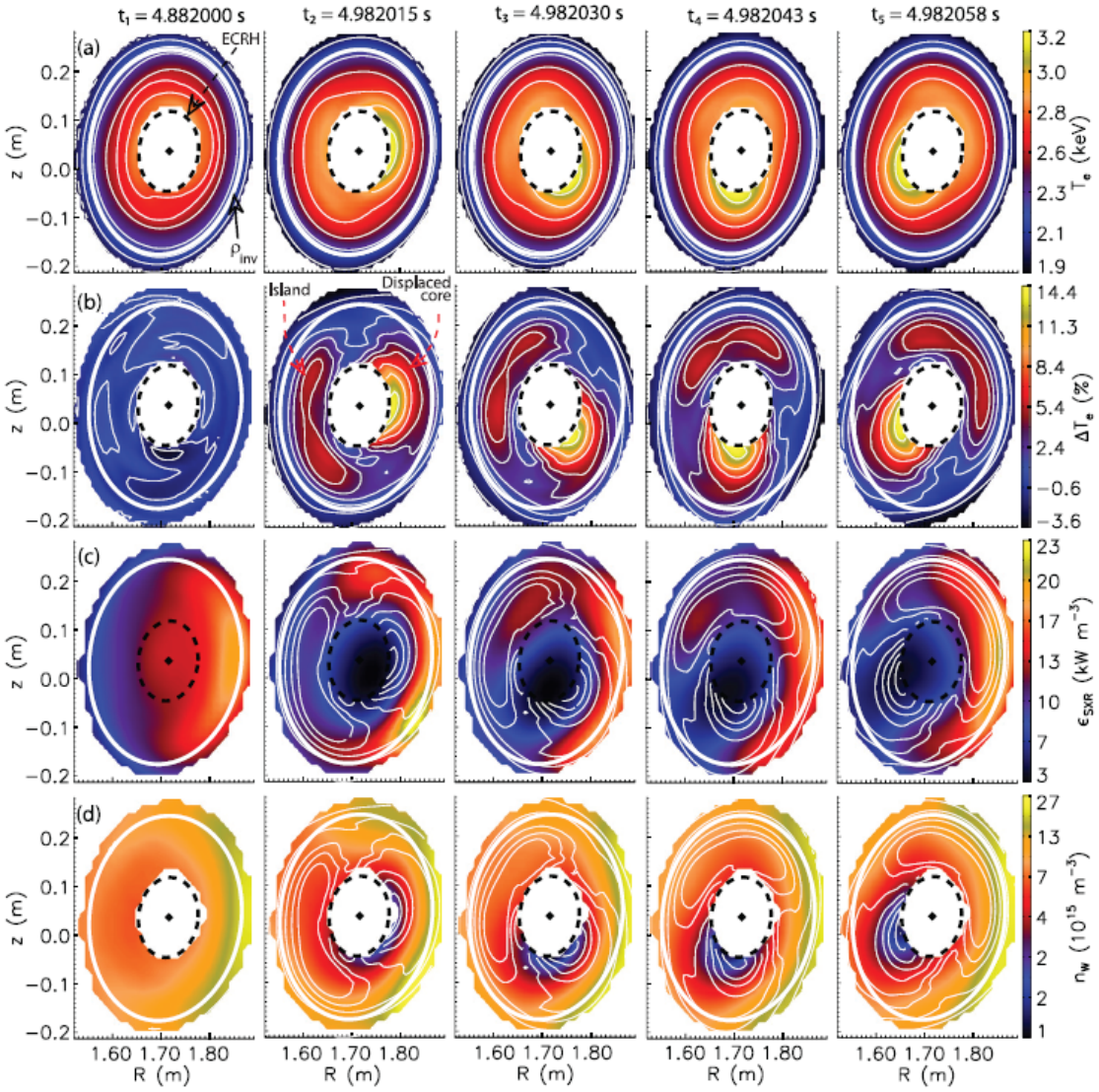

Figure 4.7: 2-D maps of a) the electron temperature T_e, b) its variation $\Delta T_e(t) \equiv T_e(t) - \langle T_e(t = t_1)\rangle$ with respect to the start of the sawtooth cycle $t = t_1$, c) SXR emissivity and d) tungsten density [Sertoli et al., 2015b]. The ECRH deposition at $\rho_{RF} \simeq 0.1$ is represented by dashed black lines and the inversion radius is marked by thick white lines. Contours of $\Delta T_e(t)$ are over-plotted on c)–d) for correlation of the quantities with the mode structure.

is correlated with the displacement of the hot core. It is consistent with the hollow tungsten density profile shown in Figure 4.7-d. This shows that tungsten is continuously expelled from the displaced hot core and redistributed in the core region. Before the next crash, a state is reached where tungsten is depleted in the displaced core.

Figure 4.8 shows the evolution of this dark spot during the sawtooth crash at $t \simeq 5.00\,\mathrm{s}$. The dark spot which was continuously rotating in the poloidal direction is progressively expelled across the $q = 1$ surface. As soon as the initial dark spot is expelled, another dark spot appears near the magnetic axis. The complex behaviour observed in the 2-D SXR emissivity map during sawtooth crash is likely due to impurity redistribution. The probable explanation to this behaviour is that the impurities are transported by the convection due to the MHD instability while magnetic reconnection occurs [Nagayama et al., 1991][Ahn et al.,

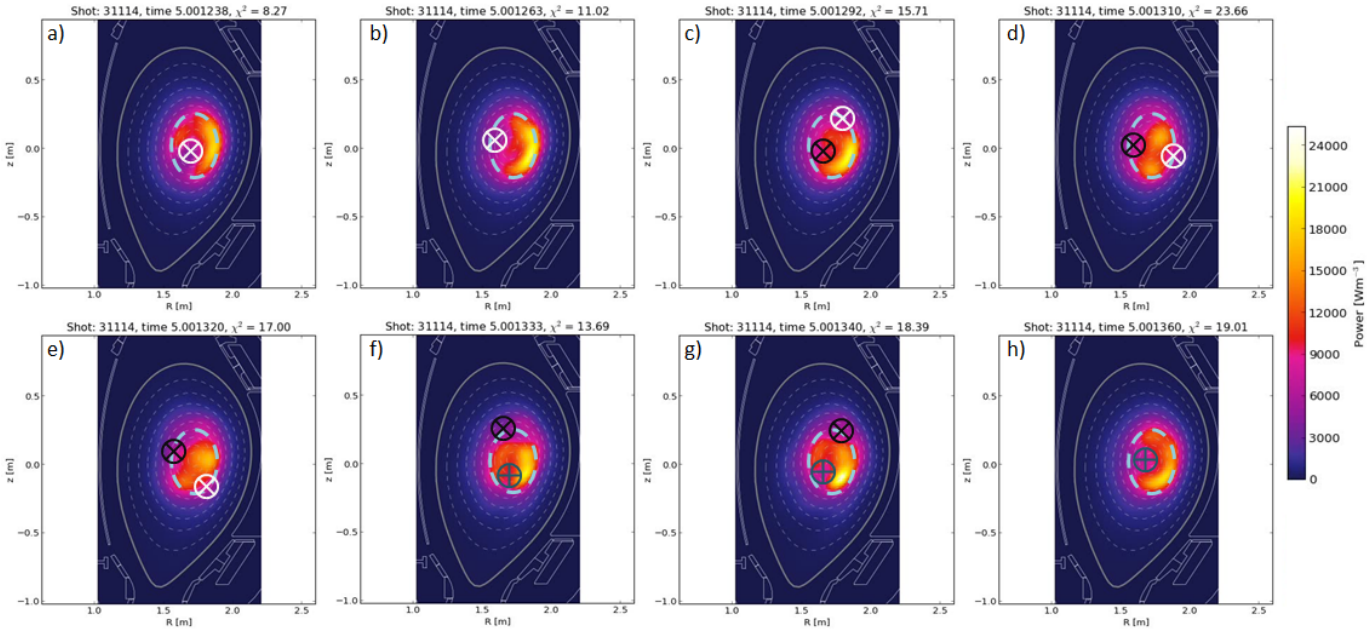

Figure 4.8: a)-h) Reconstructed 2-D SXR emissivity during a sawtooth crash at $t \simeq 5.00\,\mathrm{s}$ of the ASDEX-Upgrade discharge #31114 [Odstrcil, private comm.]. The $q = 1$ surface is marked by dashed green lines. A dark spot marked by a cross, is progressively expelled out of the $q = 1$ surface. As soon as the initial dark spot is expelled, another dark spot is observed in the core.

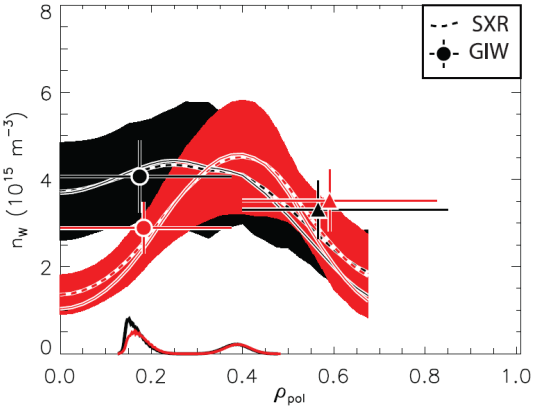

Figure 4.9: Tungsten profiles before (*red line*) and after (*black line*) a sawtooth crash when $\rho_{RF} \simeq \rho_{inv}$ [Sertoli et al., 2015b]. The post-crash tungsten density profile is in a good agreement with Kadomtsev's model.

2016b]. Still, it is necessary to compare these observations with numerical computations for further investigations.

Tungsten density profiles before and after sawtooth crash are displayed in Figure 4.9. As seen in Figure 4.7, the tungsten density profile is hollow during the (1,1) mode saturation. The post-crash tungsten density profile is flattened inside the inversion radius located at $\rho_{pol} \simeq 0.35$. This picture is in a good agreement with Kadomtsev's model [Ödblom et al., 1996]. Indeed, impurity density profile is flattened after a sawtooth crash. Therefore, it is essential to investigate why the impurity profile is hollow during the helical equilibrium.

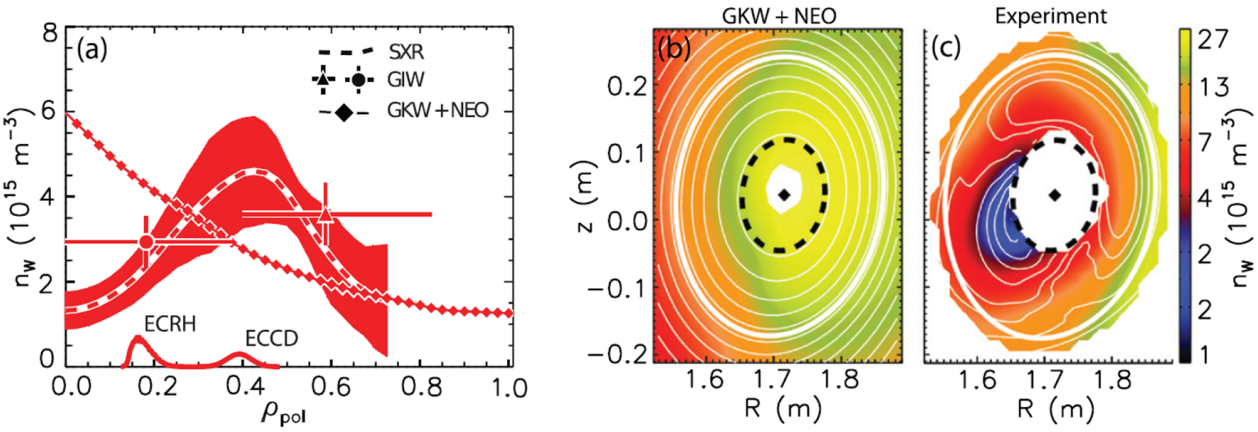

Figure 4.10: Comparison of the tungsten density distribution at $t \simeq 4.97$s of the ASDEX-Upgrade discharge #31114 with predictions from transport codes [Sertoli et al., 2015b]. a) The model predicts a peaked surface averaged tungsten density profile, whereas the measured profile is hollow. b)-c) The comparison of the 2-D tungsten density maps shows clear discrepancy.

Comparison with transport codes

The tungsten behaviour in the ASDEX-Upgrade discharge #31114 is modelled with transport codes [Sertoli et al., 2015b], using experimental data and neglecting the effects of MHD activity. The temperature and density profiles from IDA (Integrated Data Analysis) used as inputs of the transport codes, correspond to the time $t \simeq 4.97$ s where the $(1,1)$ mode is saturated. The modelling was performed by combining the neoclassical and gyrokinetic codes NEO [Belli and Candy, 2012] and GKW [Casson et al., 2010]. Further details on the comparison are presented in Ref.[Sertoli et al., 2015b].

Figure 4.10 clearly shows that the transport models themselves are not able to reproduce the observed tungsten behaviour. The flux surface averaged tungsten density profile evaluated from the measurements is peaked at an off-axis radius $\rho_{pol} \simeq 0.45$ and hollow inside the inversion radius $\rho_{pol} \simeq 0.35$ (Figure 4.10-a). Meanwhile, the transport codes predict a tungsten profile peaked at the magnetic axis. Indeed, the computed impurity pinch velocity is directed inward. The discrepancy between the observation and the prediction is clearly visible in the 2-D tungsten density maps (Figure 4.10-b,c). The HFS/LFS asymmetry due to rotation is recovered by the transport model. However, the depletion of tungsten inside the inversion radius is not recovered.

It can be inferred from this comparison that the sawtooth instability which is present throughout the discharge is responsible for the difference of tungsten profiles obtained between the measurements and the values predicted by transport codes. Indeed, during the (1,1) mode saturation, the usual assumption on an axisymmetric magnetic equilibrium to model neoclassical and turbulent transport is not valid. Moreover, neoclassical transport properties are shown to be strongly modified in a 3-D helical equilibrium [Helander and Sigmar, 2005]. Thus, the impurity transport has to be considered based on 3-D magnetic equilibrium [Garcìa-Regaña et al., 2013].

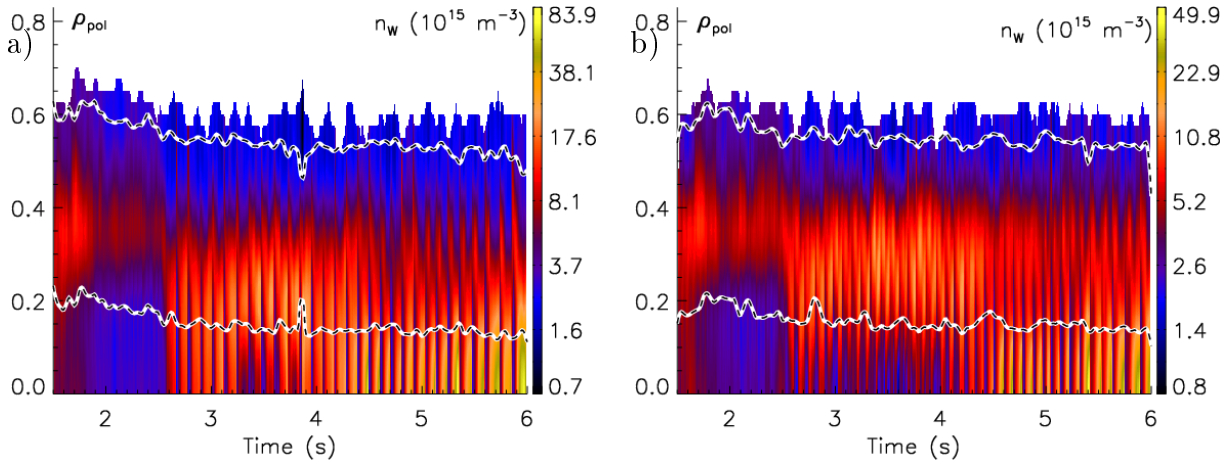

Figure 4.11: Time evolution of the tungsten density profiles during the discharges a) #32409 and b) #32410 [Sertoli, private comm.] where the radial position of ECCD is scanned. The gyrotron power injected after $t = 2.5\,\mathrm{s}$ is 0.2 MW for #32409 and 0.4 MW for #32410.

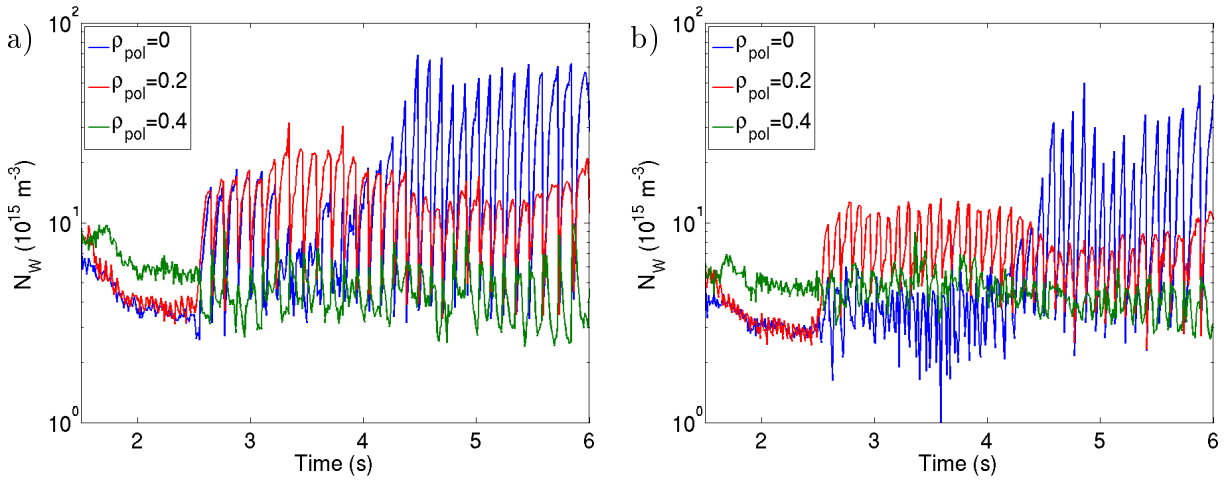

Figure 4.12: Time evolution of the tungsten density measured at $\rho_{pol} \simeq 0$ (*blue*), $\rho_{pol} \simeq 0.2$ (*red*) and $\rho_{pol} \simeq 0.4$ (*green*) during the discharges a) #32409 and b) #32410.

4.2.4 Effect of injected ECCD power

The ASDEX-Upgrade discharges #32409 and #32410 are analysed in this section. As shown in Figure 4.4, 1MW of ECRH is injected near the magnetic axis ($\rho_{RF} \simeq 0.1$) until $t = 2.5\,\mathrm{s}$, and then switched to ECCD afterwards. The scan of the radial position of ECCD starts at $t = 3.6\,\mathrm{s}$, starting from the core and moving towards the edge. Scenarios are identical in both discharges except for ECCD power, equal to 200 kW for #32409, and 400 kW for #32410.

Figure 4.11 shows the evolution of the tungsten density profiles during the discharges. It is clearly visible that the tungsten density profile is hollow at the beginning of both discharges until $t = 2.5\,\mathrm{s}$, when 1 MW of ECRH is injected near the magnetic axis. After the ECRH is switched off and replaced by 200 kW of ECCD at $t = 2.5\,\mathrm{s}$, the depletion of the tungsten density profile is barely visible in discharge #32409 (Figure 4.11-a). The tungsten density profile is hollow only in the time interval $3.2\,\mathrm{s} < t < 3.8\,\mathrm{s}$. This behaviour is illustrated by

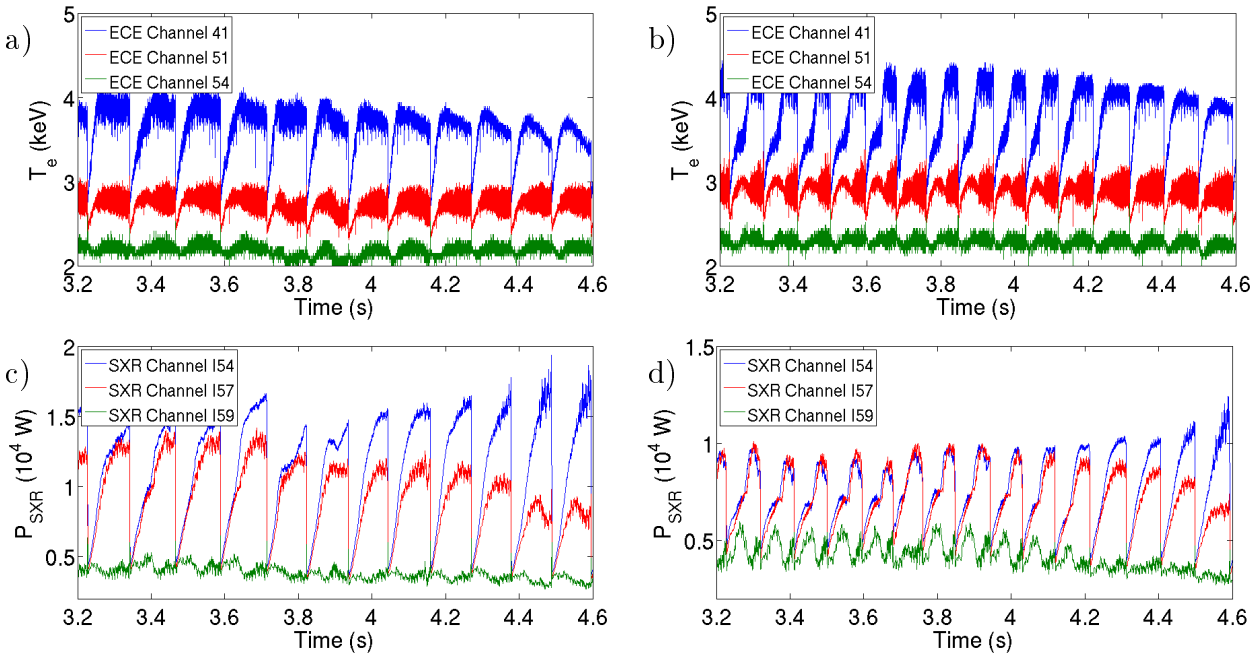

Figure 4.13: a)-b) The electron temperature and c)-d) and the line-integrated SXR measurements during the time interval $3.2\,\mathrm{s} < t < 4.6\,\mathrm{s}$ of the ASDEX-Upgrade discharges #32409 (a,c) and #32410 (b,d). The displayed measurements correspond to $\rho_{pol} \simeq 0$ (*blue*), $\rho_{pol} \simeq 0.2$ (*red*) and $\rho_{pol} \simeq 0.4$ (*green*) (cf. Figure 4.6-b).

Figure 4.12-a. Also, it can be noticed that the tungsten profile is flat during the time interval $2.5\,\mathrm{s} < t < 3.2\,\mathrm{s}$ and starts to peak after $t \simeq 4\,\mathrm{s}$. On the contrary, the tungsten density profile is hollow until $t \simeq 4.2\,\mathrm{s}$ for discharge #32410 (Figures 4.11-b and 4.12-b).

From these two discharges, two conclusions can be drawn concerning the effects of EC wave deposition on impurity control. First, the impurity profiles are more likely to remain hollow for the cases with a higher gyrotron power injected. Second, the impurity accumulation is controlled more efficiently when the ECCD is injected near the magnetic axis. Indeed, the tungsten density profile starts to peak as soon as the ECCD deposition radius is moved off-axis at $t \simeq 4\,\mathrm{s}$. The efficiency of the on-axis EC wave deposition was also mentioned in previous studies [Dux et al., 2003][Leigheb et al., 2007]. In the discharge #31114, it can be noticed that impurity peaking is prevented by a continuous control with ECRH.

Looking at the electron temperature and the line-integrated SXR measurements (Figure 4.6-b) displayed in Figure 4.13, a correlation between the shape of sawteeth and the depletion of tungsten density profiles can be deduced. In particular, significant changes of the sawtooth dynamics are visible from the electron temperature at $\rho_{pol} \simeq 0.2$ measured by the ECE channel 51. Indeed, a small bump is present at the beginning of the 5 sawtooth cycles between $t \simeq 3.32\,\mathrm{s}$ and $t \simeq 3.86\,\mathrm{s}$ in the discharge #32409 (Figure 4.13-a). Figure 4.12-a shows that the tungsten density profile remains hollow during these sawtooth cycles. Sawtooth cycles with similar shape, with a more visible bump, appear more frequently between $t \simeq 3.22\,\mathrm{s}$ and $t \simeq 4.21\,\mathrm{s}$ of the discharge #32410 (Figure 4.13-b). Again, the tungsten density profile is hollow during this time interval as shown in Figure 4.12-b. On the contrary, tungsten density

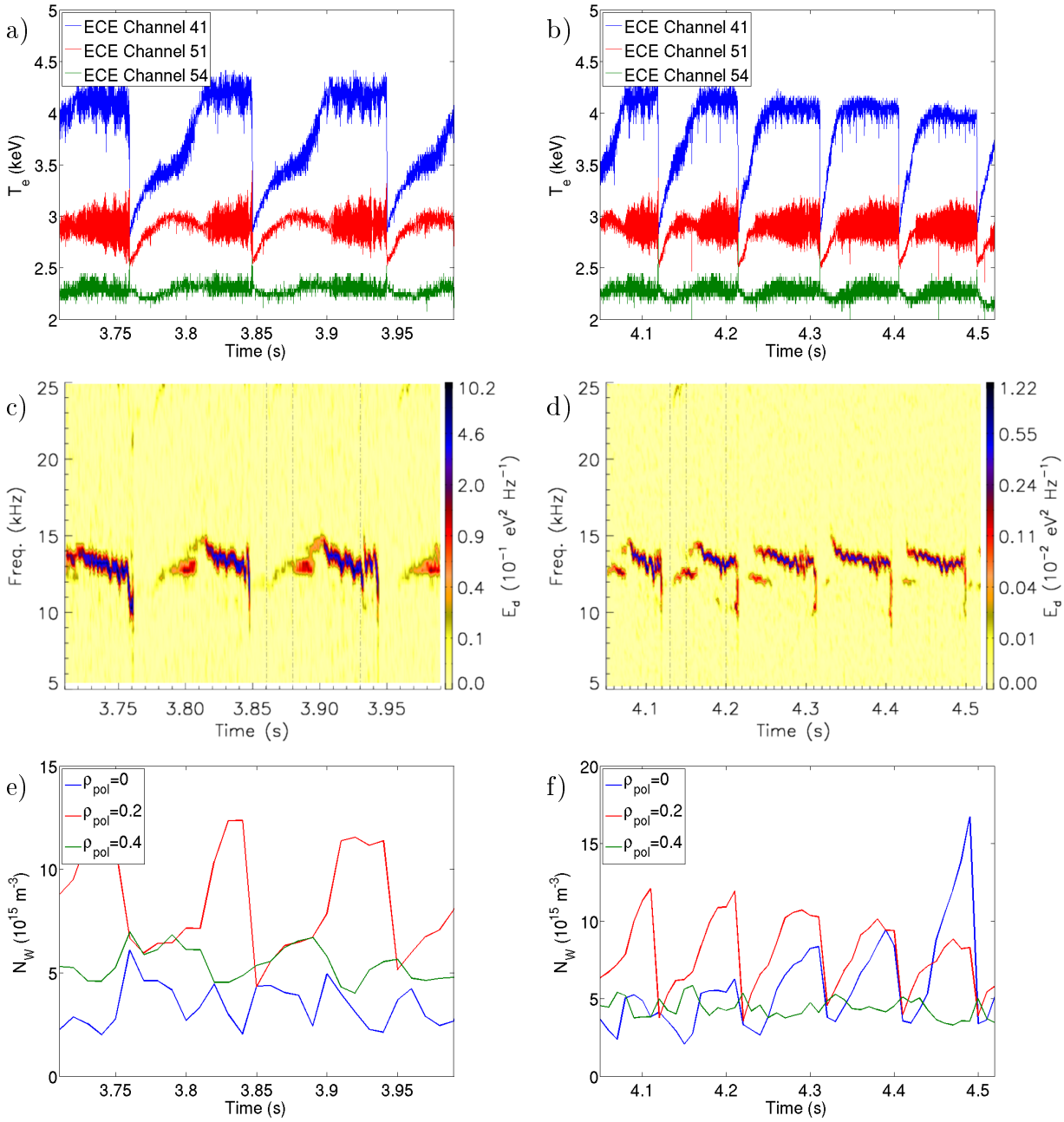

Figure 4.14: a)-b) The electron temperature measurement, c)-d) the spectrogram of the ECE channel [Sertoli, MST-1 TFM] located at $\rho_{pol} \simeq 0.1$ and e)-f) the tungsten density at different radii which correspond to the time intervals $3.71\,\mathrm{s} < t < 3.99\,\mathrm{s}$ and $4.05\,\mathrm{s} < t < 4.52\,\mathrm{s}$ of the discharge #32410.

profiles are either flat or peaked in both discharges if the 'bump' is not visible.

The shapes of sawteeth previously described were analysed in detail. Two time windows are chosen for the analysis : $3.71\,\mathrm{s} < t < 3.99\,\mathrm{s}$ where sawtooth cycles with a 'bump' in the ECE channel 51 signal are observed (Figure 4.14-a), and $4.05\,\mathrm{s} < t < 4.52\,\mathrm{s}$ where the 'bump' starts vanishing (Figure 4.14-b). Figures 4.14-c,d show the spectrograms of the ECE channel located at $\rho_{pol} \simeq 0.1$. The spectrograms indicate that the 'bumps' observed in the ECE channel 51 are characterized by a mode with a frequency $f \simeq 13\,\mathrm{kHz}$. Indeed, the change of sawtooth shapes observed at $4.05\,\mathrm{s} < t < 4.52\,\mathrm{s}$ is correlated with a lower amplitude

of this mode. The tungsten density values at different radii during these time windows are shown in Figures 4.14-e,f. They reveal that the tungsten profile is hollow when the amplitude of the mode at $f \simeq 13\,\mathrm{kHz}$ is dominant. Also, the impurity profile starts to peak when the amplitude of the mode at $f \simeq 13\,\mathrm{kHz}$ decays and the mode at $f \simeq 14\,\mathrm{kHz}$ becomes dominant. Therefore, from this analysis, it can be deduced that the tungsten density profile depletion is related to the mode frequency. Profiles are hollower for lower frequencies.

4.2.5 Open questions

The ASDEX-Upgrade discharges display a complex impurity behaviour in presence of sawteeth. The resulting impurity transport is a competition between MHD driven transport, neoclassical and turbulent transport. Furthermore, the centrifugal force due to toroidal rotation and the radiative cooling increase the complexity of the phenomenon. A particular point in these discharges is that gyrotrons are used to heat electrons or drive current in the core region. The roles played by EC waves have to be clearly identified in order to understand the observations.

ECRH is shown to affect the impurity transport properties. Indeed, the impurity diffusivity in the core region is increased by about a factor of 3 with respect to the neoclassical predictions when the deposition layer is located near the magnetic axis [Dux et al., 2003]. The impurity pinch velocity which is initially directed inward can reverse direction when ECRH is added [Scavino et al., 2003]. It can be noticed that ECCD in the core region has the same effect on impurity transport coefficients [Dux et al., 2003]. It has been suggested that turbulent transport is the reason for such a reversal in the direction of the impurity pinch [Angioni and Peeters, 2006] since the RF heating modifies the temperature gradients and the current profile.

EC waves are also known to modify the MHD dynamics of plasmas. In particular, the sawtooth dynamics is strongly affected when the deposition layer is located in the core region. Indeed, the stability of the internal kink mode is sensitive to the shear value at the $q = 1$ surface [Porcelli et al., 1996]. When the ECCD is located in the core region, the plasma current profile, thus the q-profile, is modified. ECRH induces a current as well, similarly to an ECCD mechanism, since electrons at the deposition layer are strongly heated. The so-called 'humpback' sawteeth, the period of which is characterized by the poloidal rotation of the displaced hot core, are reported in TCV experiments [Pietrzyk et al., 1999][Furno et al., 2001][Angioni et al., 2003]. Therefore, it is necessary to investigate how the impurity behaves during the saturated (1,1) mode, in order to explain the difference between ASDEX-Upgrade observations and calculations with transport codes.

- First, the presence of a displaced hot core breaks the assumption of toroidal symmetry. Thus, the neoclassical transport properties are strongly modified as the toroidal canonical momentum is no longer an invariant [Helander and Sigmar, 2005]. Therefore, the impurity transport has to be revised and computed with a 3-D equilibrium

configuration [Garcìa-Regaña et al., 2013].

- Second, the underlying reconnection process related to the sawtooth shape modification by EC waves provides another option in an MHD framework. Indeed, the radially displaced hot core which remains inside the $q = 1$ surface is reminiscent of the partial crash described in Chapter 3. As Figure 3.16 shows, the energy content inside the $q = 1$ surface slightly and slowly decreases during the partial crash, which is a signature of magnetic reconnection. This may lead to the onset of a large impurity density gradient. If it is the case, impurities are then slowly flushed out from the core region during the reconnection.

The observed impurity behaviour results from complex physics which combine MHD, neoclassical and turbulent transport. However, different transport processes must not be treated separately as synergistic effects exist between neoclassical and turbulent transport [Estève, 2015], MHD and 3-D transport. Consequently, a model including the transport theory and the sawtooth instability is necessary to investigate the underlying mechanism which expels tungsten from the hot core.

4.3 Summary

In this chapter, the impurity behaviour in experiments is described.

- The SXR diagnostic has a great advantage to give measurements proportional to the impurity density at a fast acquisition frequency. Combined with electron density and temperature measurements, the tomographic inversion of SXR measurements allows one to assess the 2-D impurity distribution in the core during a fast MHD events such as sawteeth. The impurity behaviour during ASDEX-Upgrade discharges is deduced from these measurements.

- The impurity profiles observed in ASDEX-Upgrade discharges are different from the predictions with transport codes.

- Two main conclusions can be drawn from the detailed analysis of measurements. First, the impurity profile is hollow when EC waves are injected in the core region. Second, the depletion of tungsten in the core region is closely related to the internal kink mode characterized by a lower frequency.

As an intermediate step towards the understanding of the impurity behaviour observed in ASDEX-Upgrade discharges, the next chapter focuses on modelling heavy impurity transport in sawtoothing plasmas.

The impurity behaviour is a result of a complex combination of MHD driven transport, neoclassical and turbulent transport. However, no code is so far able to address the 3 transport processes at the same time. Since heavy impurities are highly collisional in the core,

appropriate fluid equations can be used to model neoclassical transport. Therefore, the interaction between MHD and neoclassical transport can be addressed with the XTOR-2F code. Three main milestones have to be achieved in order to study such ASDEX-Upgrade scenarios using the XTOR-2F code.

- An appropriate heavy impurity transport model has to be implemented in the XTOR-2F code.
- A new set of rescaled parameters has to be found in order to simulate sustained sawtooth cycles with ASDEX-Upgrade equilibrium and geometry.
- A sawtoothing bulk plasma with saturated (1,1) mode has to be simulated with the implemented ECCD propagation model [Février, 2016].

The geometrical aspect of sawtooth dynamics has already been discussed in Chapter 3. Chapter 5 focuses on a particular point : impurity transport in sawtoothing plasmas. The study of the combined effect of neoclassical transport and sawteeth is presented.

CHAPTER 5

Transport of heavy impurities in presence of sawtooth oscillations

Contents

As seen in Chapter 4, the impurity behaviour results from a complex combination of MHD, collisional and turbulent transport. Indeed, the measured impurity profiles in presence of the internal kink mode differ from those predicted by neoclassical and turbulent theories [Sertoli et al., 2015b]. As heavy impurities are in a highly collisional region, collisional and MHD transport can be described in a fluid framework. Therefore, the interplay between MHD instabilities and impurity transport is investigated by using MHD codes. Turbulent transport is modelled by adding appropriate transport coefficients in the fluid equations. The main results presented in this chapter are published in Ref.[Ahn et al., 2016b].

5.1 Particle trajectories and collisions

5.1.1 Trapped and passing particles

Particle motion

The motion of a particle a with charge e_a and mass m_a in a magnetic field $\mathbf{B}$ is described by the Newton equation

$$\frac{\mathrm{d}\mathbf{v}}{\mathrm{d}t} = \frac{e_a B}{m_a}\mathbf{v}\times\mathbf{b} \tag{5.1}$$

where $\mathbf{v}$ is the velocity of the particle a and $\mathbf{b}\equiv\mathbf{B}/B$ is the unit vector along the magnetic field line. The velocity $\mathbf{v}$ can be decomposed into a velocity parallel to the magnetic field line $\mathbf{v}_\parallel = v_\parallel\mathbf{b}$ and a perpendicular velocity $\mathbf{v}_\perp = \mathbf{b}\times(\mathbf{v}\times\mathbf{b})$ which corresponds to cyclotron rotation. The particle a gyrates around a magnetic field line with a cyclotron pulsation ω_c and Larmor radius ρ_L defined as

$$\omega_\mathsf{c} = \frac{|e_a|B}{m_a} \qquad \rho_\mathsf{L} = \frac{m_a v_\perp}{|e_a|B} \tag{5.2}$$

The center of the gyration motion is the guiding center and will be noted G.

The strong guide field ordering can be used in tokamak plasmas. Here, a small parameter $\rho^* = \rho_\mathsf{L}/L \ll 1$ is considered, where $L\sim|\nabla\ln B|^{-1}$. At this scaling, gradients of macroscopic fields are assumed to be small on the scale of the Larmor radius. Also, the macroscopic flow variations are considered to be slower than cyclotron motion. Thus, $\omega/\omega_\mathsf{c}\ll 1$, where $\omega\sim|\partial_t\ln B|$.

At the lowest order in ρ^*, only the cyclotron motion is taken into account, and the guiding center G follows the magnetic field lines with a constant velocity. However, at the next order, the trajectory of the guiding center G is modified by drift velocities. These particle drifts are due to magnetic field gradient $\boldsymbol{\nabla}B$ and toroidal curvature $\boldsymbol{\kappa}\equiv(\mathbf{b}\cdot\boldsymbol{\nabla})\mathbf{b}$. The magnetic drift velocity then reads

$$\mathbf{v}_\mathrm{d} = \frac{v_\perp^2}{2\omega_\mathsf{c}}\frac{\mathbf{B}\times\boldsymbol{\nabla}B}{B^2} - \frac{v_\parallel^2}{\omega_\mathsf{c}}\boldsymbol{\kappa}\times\mathbf{b} \tag{5.3}$$

In particular, $\boldsymbol{\kappa}\simeq\boldsymbol{\nabla}_\perp B/B$ in a low-beta plasma and

$$\mathbf{v}_\mathrm{d} \simeq -\frac{v_\parallel^2 + v_\perp^2/2}{\omega_\mathsf{c}\mathsf{R}}\hat{\mathbf{e}}_\mathsf{Z} \tag{5.4}$$

The presence of an electric field $\mathbf{E}$ yields an additional drift velocity. The $\mathbf{E}\times\mathbf{B}$ drift velocity $\mathbf{V}_E$ defined as

$$\mathbf{V}_E = \frac{\mathbf{E}\times\mathbf{B}}{B^2} \tag{5.5}$$

is independent of the particle charge and mass. As a consequence, this drift leads to a net flow of the plasma but not to a current. The polarization drift or inertia drift velocity defined

as

$$\mathbf{v}_P = \frac{1}{B\omega_c}\frac{\partial \mathbf{E}_\perp}{\partial t} \tag{5.6}$$

must be added at the next order in ω/ω_c, if the electric field $\mathbf{E}$ is time dependent with a time scale ω^{-1}.

Trapping condition

An axisymmetric equilibrium with an adiabatic approximation can be characterized by three constants of motion : the magnetic moment μ_a, the kinetic toroidal angular momentum $\mathsf{p}_{\varphi,a}$ and the total energy E_a

$$\mu_a = \frac{m_a v_\perp^2}{2B} \tag{5.7}$$

$$\mathsf{p}_{\varphi,a} = m_a \mathsf{R} v_\varphi - e_a \psi \tag{5.8}$$

$$\mathsf{E}_a = \frac{1}{2} m_a v_\parallel^2 + \mu_a B + e_a \phi \tag{5.9}$$

In the absence of electrostatic potential ϕ, the particle energy of the species a is

$$\mathsf{E}_a = \frac{1}{2} m_a v_\parallel^2 + \mu_a B \tag{5.10}$$

Thus, the parallel velocity reads

$$v_\parallel = \pm\sqrt{\frac{2}{m_a}\left(\mathsf{E}_a - \mu_a B\right)} \tag{5.11}$$

A particle is decelerated by the mirror force $-\mu_a \nabla_\parallel B$ as it moves to the high-field side (HFS). As a consequence, the particle can be either trapped or passing, depending on its energy E_a. At small inverse aspect ratio ϵ, the magnetic field B varies as

$$B(r,\theta) \simeq \frac{B_0}{1+\epsilon\cos\theta} \tag{5.12}$$

where $\epsilon = r/\mathsf{R}_0$ is the inverse aspect ratio. Hence, $B_{min} \leq B \leq B_{max}$ with

$$B_{min} = B(r,\theta=0) = \frac{B_0}{1+\epsilon} \qquad B_{max} = B(r,\theta=\pi) = \frac{B_0}{1-\epsilon} \tag{5.13}$$

If $\mathsf{E}_a > \mu_a B_{max}$, particles are decelerated in the HFS, but still have sufficient energy to explore the whole range of poloidal angles. The particle is then called passing or circulating. If $\mu_a B_{min} < \mathsf{E}_a < \mu_a B_{max}$, a bounce angle θ_b, where the parallel velocity $v_\parallel = 0$, is found. In this case, the particle moves along the magnetic field line within a poloidal angle range $|\theta| < \theta_\mathsf{b}$ (Figure 5.1).

Using the invariance of μ_a and E_a, one can deduce

$$B_{\mathsf{b}} = B(r, \theta = \pm\theta_{\mathsf{b}}) = B_{min}\left(1 + \left.\frac{v_\parallel^2}{v_\perp^2}\right|_{\theta=0}\right) \tag{5.14}$$

As a consequence, the condition $B_{min} \leq B_{\mathsf{b}} \leq B_{max}$ gives the trapping condition, for $\epsilon \ll 1$

$$\left.\frac{v_\parallel}{v_\perp}\right|_{\theta=0} \leq \sqrt{\frac{2\epsilon}{1-\epsilon}} \simeq \sqrt{2\epsilon} \tag{5.15}$$

The fraction of trapped particles on a magnetic surface of minor radius r reads

$$f_t \simeq 1.46\sqrt{\epsilon} \tag{5.16}$$

Particle excursion from magnetic flux surfaces

As seen in the expression (5.4), the presence of the drift velocity $\mathbf{v}_{\mathrm{d}}$ shifts the guiding center trajectory in a direction perpendicular to the magnetic field (Figure 5.1).

The invariance of the toroidal angular momentum $\mathsf{p}_{\varphi,a}$ (5.8) for a passing particle gives

$$m_a r \cos\theta v_\varphi \simeq e_a \frac{\mathrm{d}\psi}{\mathrm{d}r}\delta r_{\mathsf{c}} \tag{5.17}$$

As $v_\varphi \simeq v_\parallel$, $\mathrm{d}\psi/\mathrm{d}r \simeq \mathsf{R}_0 B_\theta$ and $q \simeq rB_\varphi/(\mathsf{R}_0 B_\theta)$

$$\delta r_{\mathsf{c}} \simeq \frac{r}{\mathsf{R}_0 B_\theta}\frac{m_a v_\parallel}{e_a}\cos\theta \simeq q\frac{v_\parallel}{\omega_{\mathsf{c},a}}\cos\theta \tag{5.18}$$

For passing particles, $v_\perp \ll v_\parallel \simeq V_{T,a}$, where

$$V_{T,a} = \sqrt{\frac{T_a}{m_a}} \tag{5.19}$$

is the thermal velocity of the particle a. The guiding center trajectory is shifted by δr_{c} after one poloidal turn, where

$$\delta r_{\mathsf{c}} \sim q\rho_{\mathsf{L}} \tag{5.20}$$

For trapped particles, $v_\parallel \ll v_\perp \simeq V_{T,a}$. The trajectory of its guiding center takes the form of a banana in the poloidal plane. The poloidal angle θ bounces between the angles $\pm\theta_{\mathsf{b}}$. Its characteristic width δr_{b} is maximum at $\theta = 0$, and is called banana width. Again, the invariance of the toroidal angular momentum $\mathsf{p}_{\varphi,a}$ (5.8) at two points of the trajectory $\theta = 0$ and $\theta = \theta_{\mathsf{b}}$ gives

$$m_a R v_\varphi \simeq e_a \frac{\mathrm{d}\psi}{\mathrm{d}r}\delta r_{\mathsf{b}} \tag{5.21}$$

As $v_\varphi \simeq v_\parallel \simeq \epsilon^{1/2} v_\perp$

$$\delta r_{\mathsf{b}} \simeq \frac{m_a v_\parallel}{e_a B_\theta} \simeq q\rho_{\mathsf{L}}\epsilon^{-1/2} \tag{5.22}$$

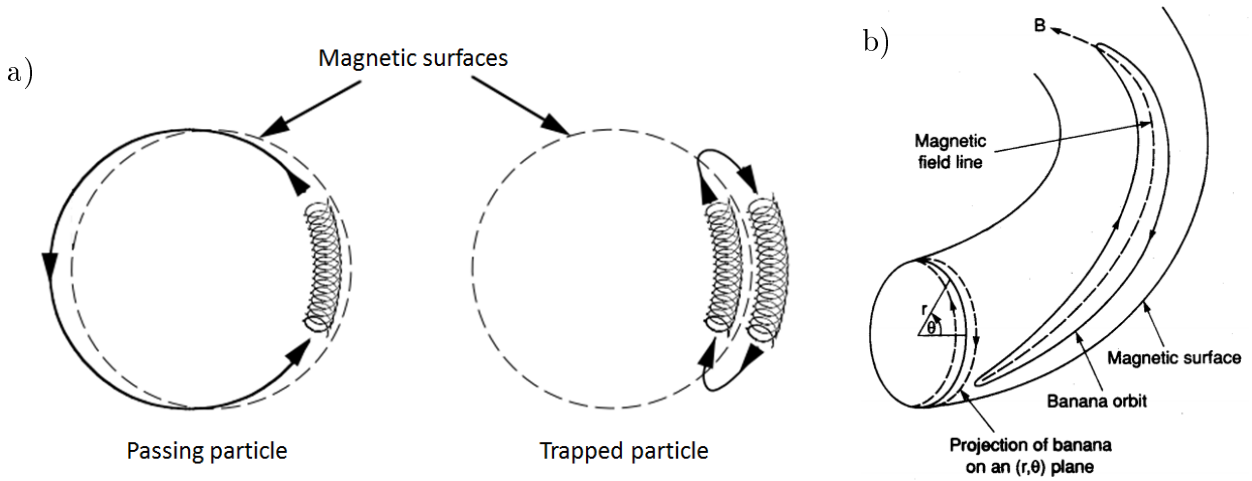

Figure 5.1: a) Schematic figures of passing and trapped particle trajectories projected in a poloidal cross section. b) A 3-D representation of a banana orbit.[1]

Along its trajectory, a trapped particle moves over a typical distance $q\mathsf{R}_0$ with a speed $v_\parallel$. An estimation of the bounce time of a trapped particle travelling along the field line is

$$\tau \simeq \frac{q\mathsf{R}_0}{v_\parallel} \tag{5.23}$$

The characteristic frequency of a particle oscillating between the two cusps of the banana orbit is called bounce frequency ω_b

$$\omega_\mathsf{b} \simeq \tau^{-1} \simeq \frac{V_{T,a}}{q\mathsf{R}_0}\epsilon^{1/2} \tag{5.24}$$

5.1.2 Coulomb collisions

Charged particles in tokamak plasmas interact through Coulomb collisions. A transfer of momentum due to the Coulomb force results in a deviation of particle velocities. Due to the long range of the Coulomb force, the velocity deflection is usually small. Still, in tokamak plasmas, collisions with large scattering angle exist with a small probability. These collisions allow fusion reactions to occur. Nonetheless, large scattering collisions are rare enough to be neglected in the framework of transport and MHD studies of this thesis.

As an example, let us consider a simple model in order to evidence the main features of the process : a population of particles a with mass m_a, charge e_a and velocity V_a, passing through a medium of particles b at rest with mass m_b, charge e_b and density N_b (Figure 5.2). Both charges are supposed to have the same sign ($e_a e_b > 0$). The deviation of particle trajectory is quantified by the scattering angle α_d. The distance r_{min} corresponds to the closest distance between particles a and b within the trajectory. These quantities depend on the impact

[1] Images from a lecture of plasma physics, Australian National University

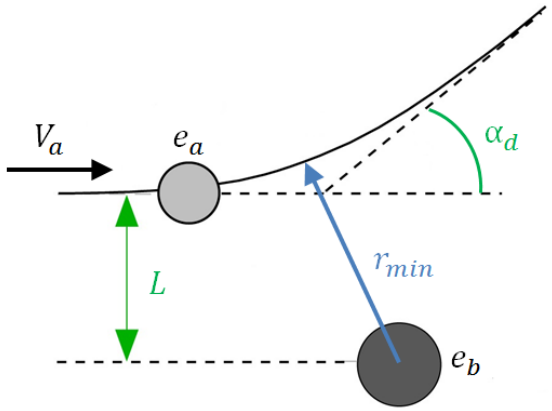

Figure 5.2: Schematic figure of Coulomb collision between two charged particles with the same sign.

parameter L. The minimum distance of approach λ_{min} is defined as $\lambda_{min} = r_{min}|_{L=0}$.

$$\lambda_{min} = \frac{e_a e_b}{2\pi\varepsilon_0 m_a V_a^2} \tag{5.25}$$

This distance corresponds to the Landau length.

A typical collision occurs with an impact parameter L of the order of the Debye length

$$\lambda_D = \sqrt{\frac{\varepsilon_0 T_e}{N_e e^2}} \tag{5.26}$$

where N_e and T_e are respectively the electron density and temperature of the plasma, and e is the elementary charge. Indeed, the Coulomb interaction is shielded for particles with $L \gg \lambda_D$. In the case of laboratory plasmas, $\lambda_D \gg \lambda_{min}$. Thus, most collisions are well described by small velocity deflections as illustrated in Figure 5.2. The Coulomb logarithm $\Lambda = \ln(\lambda_D/\lambda_{min})$ is in the range $\Lambda = 10 - 20$ for tokamak plasmas with typical density $N_e \simeq 10^{20}\mathrm{m}^{-3}$ and temperature $T \simeq 10\mathrm{keV}$.

The collision frequency ν_{ab} between two species a and b for this example is

$$\nu_{ab} \simeq \frac{4\sqrt{2\pi}}{3} \frac{e_a^2 e_b^2 \Lambda}{(4\pi\varepsilon_0)^2} \frac{N_b}{m_a^2 V_a^3} \tag{5.27}$$

Note that there are different ways to define ν_{ab}. An expression of the collision frequency given by Ref.[Hinton, 1983] reads

$$\nu_{ab} = \frac{4\sqrt{2\pi}}{3} \frac{N_b}{m_a} \left(\frac{1}{m_a} + \frac{1}{m_b}\right) \frac{e_a^2 e_b^2 \Lambda}{(4\pi\varepsilon_0)^2} \frac{1}{(V_a^2 + V_b^2)^{3/2}} \tag{5.28}$$

This expression is consistent with the action-reaction principle given by

$$m_a N_a \nu_{ab} = m_b N_b \nu_{ba} \tag{5.29}$$

5.1.3 Transport in tokamak plasmas

Collisional transport

Collisions lead to radial diffusion by moving particles from one orbit to another. This occurs with a step-size of the order of the Larmor radius $\rho_{\mathsf{L},a}$ and a characteristic time ν_a^{-1}. The associated 'classical' diffusion coefficient then reads

$$D_a^{CL} \simeq \rho_{\mathsf{L},a}^2 \nu_a \tag{5.30}$$

However, transport coefficients predicted by classical transport theory are not relevant to tokamak plasmas as most field geometric effects are omitted. Consequently, the 'neoclassical' theory which takes into account geometric and resonant effects has been developed.

The condition (5.15) separates the velocity space $(V_{\parallel,a}, V_{\mathsf{c},a})$ into trapping and circulating regions. The ratio between parallel and perpendicular velocities of a particle a is modified by collisions with a characteristic frequency ν_a. Therefore, collisions can be considered as the cause of random walks in the velocity space. After a sufficient number of collisions, a trapped particle is scattered out of the trapping region to become passing. An effective collision frequency ν_{eff} is defined to characterize this process

$$\nu_{\text{eff}} = \frac{\nu_a}{2\epsilon} \tag{5.31}$$

The collisionality parameter ν_a^* is then defined as the ratio of this effective collision frequency ν_{eff} and the bounce frequency ν_{b}

$$\nu_a^* = \frac{\nu_{\text{eff}}}{\nu_{\mathsf{b}}} \simeq \frac{q\mathsf{R}_0}{\epsilon^{3/2}} \frac{\nu_a}{V_{T,a}} \tag{5.32}$$

This dimensionless number characterizes the capacity of a particle to complete an orbit of its trapped trajectory before it is detrapped.

Three regimes of neoclassical transport are identified according to the value of the collisionality ν_a^*.

- In the *banana* or *Galeev-Sagdeev* regime, trapped particles barely collide and usually complete a bounce or transit motion before experiencing a collision. The collisionality parameter is then small ($\nu_a^* \ll 1$). The radial diffusion is mainly governed by the modification of trapped particle motion through collisions. The diffusion coefficient can be written as

  $$D_a^B \simeq q^2 \frac{\rho_{\mathsf{L},a}^2}{\epsilon^{3/2}} \nu_a \tag{5.33}$$

  At such low collisionalities, passing particles do not contribute to transport.

- On the contrary, the *Pfirsch-Schlüter* regime corresponds to a very high collisionality $\nu_a^* \gg \epsilon^{-3/2}$. Collisions occur for both passing and trapped particles, before they

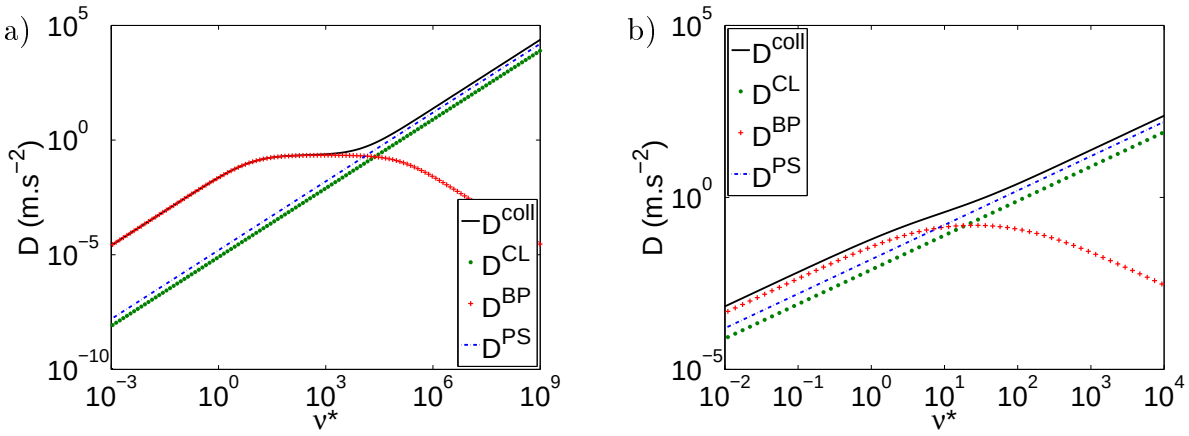

Figure 5.3: Diffusion coefficients of different collisional regimes computed according to Ref.[Wenzel and Sigmar, 1990] (a) in the limit of $\epsilon \ll 1$ ($\epsilon = 10^{-3}$) and (b) $\epsilon = 0.1$.

complete a transit motion. The Pfirsch-Schlüter diffusion coefficient reads

$$D_a^{PS} \simeq q^2 \rho_{\mathrm{L},a}^2 \nu_a \tag{5.34}$$

- The *plateau* regime corresponds to an intermediate collisionality $1 \ll \nu_a^* \ll \epsilon^{-3/2}$. Only a fraction of trapped particles can complete their trajectories before collision. The diffusion coefficient is independent of the collision frequency

$$D_a^P \simeq \frac{D_a^B}{\nu_a^*} = q \rho_{\mathrm{L},a}^2 \frac{V_{T,a}}{\mathrm{R}_0} \tag{5.35}$$

Figure 5.3-a shows classical and neoclassical diffusion coefficients as function of collisionality in the limit of $\epsilon \ll 1$.

Each diffusion coefficient has its own expression defined on the entire domain of collisionality [Hirshman and Sigmar, 1981][Wenzel and Sigmar, 1990]. Hence, they are summed to give the total contribution of collisional transport

$$D_a^{coll} = D_a^{CL} + D_a^{NC} \qquad D_a^{NC} = D_a^{BP} + D_a^{PS} \tag{5.36}$$

It can be noticed that the consideration of small inverse aspect ratio ($\epsilon \ll 1$) is not really valid in tokamaks. As a consequence, the plateau regime almost vanishes for realistic geometrical parameters (Figure 5.3-b).

Turbulent transport

Particle and heat transport coefficients measured in experiments are larger than neoclassical predictions by an order of magnitude for ions (two orders for electrons). The effects of turbulence have been studied to explain this anomalous transport. It is due to fluctuations of

the magnetic field $\mathbf{B}$ and the electric field $\mathbf{E}$ around their equilibrium values. These quantities can be written as $\mathbf{B} = \mathbf{B}_0 + \widetilde{\mathbf{B}}_1$ and $\mathbf{E} = \mathbf{E}_0 + \widetilde{\mathbf{E}}_1$, with $|\widetilde{\mathbf{B}}_1|/|\mathbf{B}_0| \ll 1$ and $|\widetilde{\mathbf{E}}_1|/|\mathbf{E}_0| \ll 1$.

The variation of $\widetilde{\mathbf{B}}_1$ around the equilibrium magnetic field $\mathbf{B}_0$ induces a perpendicular velocity $\mathbf{V}_{\delta B} = V_{\|}\widetilde{\mathbf{B}}_1/B$. This velocity depends on the parallel velocity, which is of the order of the thermal velocity. Hence, the radial transport driven by magnetic perturbations is negligible for ion species and impurities compared to electrons. The perturbation $\widetilde{\mathbf{E}}_1$ of the electric field causes a radial transport directly via the electrical drift velocity $\mathbf{V}_E$ which is the same for all species. These radial fluxes modify the density and temperature gradients, which in turn sustain the turbulence via micro-instabilities.

Neoclassical transport is associated with small toroidal and poloidal mode numbers ($\mathsf{n} = 0$, $\mathsf{m} \gtrsim 1$), whereas turbulent transport process has much larger mode numbers m, $\mathsf{n} \gg 1$. Hence, the total diffusion coefficient D^{tot} and pinch velocity V_p^{tot} are then deduced by adding collisional and turbulent transport coefficients

$$D^{tot} = D^{coll} + D^{turb} \qquad V_p^{tot} = V_p^{coll} + V_p^{turb} \tag{5.37}$$

Heavy impurity transport

Understanding the dynamics of heavy impurities in fusion plasmas is an important issue, especially since it has been decided to equip ITER with a tungsten ($\mathcal{Z}_{\mathrm{W}} = 74$, $\mathcal{A}_{\mathrm{W}} = 184$) divertor. The collisionality of the impurity has to be known in order to characterize its neoclassical regime. In general, the collision frequency of the species a in multi-species plasmas is a sum of collision frequencies with other species b : $\nu_a = \nu_{aa} + \sum_{b \neq a} \nu_{ab}$. A general expression of collision frequency is given in (5.28).

Here, quantities related to the main ion species and to an impurity will be labelled respectively with indexes i and z. Heavy impurities have high charge numbers in the core region ($Z_z \gg Z_i$). The relevant parameter to quantify the impurity content in plasmas is the impurity strength parameter

$$\alpha_z \equiv \frac{Z_z^2 N_z}{Z_i^2 N_i} \tag{5.38}$$

rather than its concentration N_z/N_i, as Coulomb collisions involve charge numbers. Heavy impurities are considered as trace ($\alpha_z \ll 1$) and thermalized to ion temperature ($T_z \simeq T_i$). Under these assumptions,

$$\nu_{iz} = \sqrt{2}\frac{Z_z^2 N_z}{Z_i^2 N_i}\nu_{ii} \simeq \alpha_z \nu_{ii} \qquad \nu_{zi} \simeq \alpha_z^{-1}\nu_{zz} \tag{5.39}$$

Therefore, $\nu_i \simeq \nu_{ii}$ and $\nu_z \simeq \nu_{zi}$. Finally

$$\nu_z \simeq \frac{Z_z^2 m_i}{Z_i^2 m_z}\nu_i \tag{5.40}$$

and the impurity collisionality reads

$$\nu_z^* \simeq \frac{Z_z^2}{Z_i^2}\sqrt{\frac{m_i}{m_z}}\nu_i^* \tag{5.41}$$

As a consequence, heavy impurities are highly collisional due to their high charge number. For tungsten, an approximate charge $Z_{\mathrm{W}} \simeq 45$ can be retained according to the tungsten ion charge distribution in the core region where the electron temperature ranges from 3 to 6keV (Figure 4.1).

At high collisionality, the relevant framework is the Pfirsch-Schlüter regime. However, the main ion species characterized by low charge number remains in the weakly collisional banana or plateau regime except in the pedestal region and near the magnetic axis. In this case, neoclassical theory predicts that the ion temperature gradient drives an outward impurity flux, and is thus responsible for a favourable thermal screening effect [Hirshman and Sigmar, 1981][Helander and Sigmar, 2005]. Recent experiments and simulations with transport codes are consistent with this picture [Angioni et al., 2014][Casson et al., 2015].

In addition, neoclassical transport for heavy impurities is shown to be enhanced due to the poloidal asymmetry of the impurity density caused by the centrifugal force [Hinton and Wong, 1985][Catto et al., 1987][Belli et al., 2014] or RF heating [Reinke et al., 2012][Bilato et al., 2014][Casson et al., 2015]. Indeed, the effects due to rotation are stronger for heavy impurities. In a rotating plasma with toroidal angular frequency Ω, an ion species a has a Mach number

$$M_a = \frac{m_a \Omega^2 \mathrm{R}^2}{2T_i} \tag{5.42}$$

with T_i the temperature of the main ion species. For heavy impurities, the Mach number M_z can be of order unity ($M_z \sim 1$) even if $M_i \ll 1$ for the main ion species. As a consequence, neoclassical transport has to be considered along with turbulent transport for heavy impurities. In addition, strong toroidal rotation is shown to affect the impurity transport properties. Indeed, the impurity diffusivity is enhanced by toroidal plasma rotation by a factor $(1+M_z)^2$ [Romanelli and Ottaviani, 1998]. Also, the thermal screening effect is weakened due to the effect of rotation, and can even change its sign so that the temperature gradient contribution drives an unfavourable influx of impurity [Fülöp and Helander, 1999][Angioni and Helander, 2014].

5.2 Fluid description of heavy impurity transport

5.2.1 Stakes

Magneto-hydrodynamic (MHD) instabilities such as tearing modes and sawtooth oscillations add complexity to the impurity behaviour in core plasmas. It is well known that sawtooth crashes drive an efficient core radial transport of impurities [Wesson et al., 1997][Dux

et al., 1999][Yamada et al., 2010]. If the pre-crash impurity profile is peaked, the profile is flattened after a sawtooth crash in a region which is approximatively encompassed by the $q = 1$ surface. Sawteeth then tend to prevent impurity accumulation in the center. On the contrary, for a hollow impurity density profile, the impurities penetrate inside the $q = 1$ surface at each sawtooth crash. This behaviour is consistent with the Kadomtsev reconnection model [Kadomtsev, 1975][Furno et al., 2001] for different pre-crash impurity profiles [Ödblom et al., 1996]. In addition, the presence of 2D structures of impurity density during sawtooth crashes has been evidenced in the XTOR-2F simulations [Nicolas et al., 2014]. All in all, sawteeth tend to smooth the impurity density gradients in the core.

In the following, we will illustrate and analyse heavy impurity transport during sawtooth oscillations with the XTOR-2F code [Lütjens and Luciani, 2010]. As described in Chapter 2, the XTOR-2F code has been upgraded to modulate impurity continuity and parallel momentum equations. Both are coupled self-consistently with the set of two-fluid equations describing the bulk plasma, which is an important improvement made during this thesis, compared to the work in Ref.[Nicolas et al., 2014]. For this study, let us consider a plasma containing only one type of impurity.

5.2.2 Relationship between radial particle flux and parallel forces

Orderings

A species is in a highly collisional regime when the collisionality $\nu/\omega_t \gg 1$, where ν and ω_t are the characteristic collision and transit frequencies respectively. The distribution function in the velocity space is then relaxed to a Maxwellian function due to the collisions. Also, macroscopic scale lengths L (e.g. density or temperature gradients) are large compared to the Larmor radius ρ_L : $\rho^* \equiv \rho_L/L \ll 1$. Therefore, the fluid description is legitimate for species in a collisional regime.

MHD equations are derived from the kinetic equation by supposing a large perpendicular electric field, i.e. $|\mathbf{V}_E|/V_T \sim 1$. In the framework of the neoclassical theory, rapid fluid motions are neglected by using the drift ordering where $|\mathbf{V}_E|/V_T \sim \rho^*$. Thus, the plasma is supposed to be in a quiescent state, i.e. in a configuration of nested magnetic flux surfaces for long time scales. These assumptions are likely not to be fulfilled during a sawtooth crash. However, this is not a strong limitation since particle and heat fluxes are mainly tied to fast reconnection processes during the crash. For now, we restrict the analysis to conventional neoclassical theory.

Tokamak plasmas are usually magnetized with a field such that the gyrofrequency ω_c is large compared to the collision frequency ν. Then, the dimensionless small parameter $\delta \equiv \nu/\omega_c$ is small and can be used as an expansion parameter. Each field is then separated into a mean field represented by a flux surface averaged quantity and small perturbations which correspond to poloidal asymmetries. For example, the density N in the toroidal coordinate

system (ψ, θ, φ) is written as $N(\psi,\theta) = N_0(\psi) + \widetilde{N}_1(\psi,\theta) + O(\delta^2)$ with $\left|\widetilde{N}_1(\psi,\theta)\right| / N_0(\psi) \sim O(\delta) \ll 1$.

The starting point is the continuity and momentum equations for the species a

$$\partial_t N_a + \boldsymbol{\nabla} \cdot (N_a \mathbf{V}_a) = 0 \tag{5.43}$$

$$N_a m_a \left(\partial_t \mathbf{V}_a + (\mathbf{V}_a \cdot \boldsymbol{\nabla})\mathbf{V}_a\right) = -\boldsymbol{\nabla} P_a + N_a e_a \left(\mathbf{E} + \mathbf{V}_a \times \mathbf{B}\right) + \boldsymbol{\mathcal{R}}_a \tag{5.44}$$

The pressure anisotropy is neglected since only high collisionality (Pfirsch-Schlüter regime) is considered for this study [Hinton and Hazeltine, 1976]. The fluid velocity of the species a is a sum of the $\mathbf{E} \times \mathbf{B}$, diamagnetic and parallel velocities

$$\mathbf{V}_a = \mathbf{V}_E + \mathbf{V}_a^* + V_{\parallel,a}\mathbf{b} \tag{5.45}$$

where $\mathbf{V}_a^* = \mathbf{B} \times \boldsymbol{\nabla} P_a / (N_a e_a B^2)$.

In the force balance equation, the effect of collisions between the species a and other species b lies in the friction force $\boldsymbol{\mathcal{R}}_a = \sum_b \boldsymbol{\mathcal{R}}_{ab}$. The friction force between two species $\boldsymbol{\mathcal{R}}_{ab}$ is a sum of drag and thermal forces. A drag force is induced by a difference of velocities between the two species. A thermal force appears due to the velocity dependence of collision frequencies and is proportional to the heat fluxes. From the action-reaction principle, $\boldsymbol{\mathcal{R}}_{ab} = -\boldsymbol{\mathcal{R}}_{ba}$. As neoclassical fluxes are associated with parallel friction, the parallel components of the friction force are to be expressed in terms of different gradient lengths in the incompressible fluid limit.

In the drift ordering where flow variations are slow in space and time, the force balance equation (5.44) reads

$$-N_a e_a \left(\mathbf{E} + \mathbf{V}_a \times \mathbf{B}\right) = -\boldsymbol{\nabla} P_a + \boldsymbol{\mathcal{R}}_a \tag{5.46}$$

Through this study, the inertia term $(\mathbf{V}_a \cdot \boldsymbol{\nabla})\mathbf{V}_a$ is supposed to be small compared to other terms in the expression (5.46). In other words, the toroidal plasma rotation is considered to be weak enough so that the centrifugal force can be neglected. This corresponds for example to plasmas with little momentum injection by NBI, which is not the case for ASDEX-Upgrade discharges presented in Chapter 4. Ω in the expression (5.42) is then considered small enough so that $M_a \ll 1$ for every ion species.

Friction force between impurity and main ion species

With the expression (2.4) of the magnetic field in the toroidal coordinate system (ψ, θ, φ), the projection of Equation (5.46) along the toroidal direction $\mathsf{R}^2 \boldsymbol{\nabla} \varphi$ reads [Hazeltine and Meiss, 2003]

$$N_a e_a \mathbf{V}_a \cdot \boldsymbol{\nabla} \psi = -\mathsf{R}^2 \boldsymbol{\mathcal{R}}_a \cdot \boldsymbol{\nabla} \varphi \tag{5.47}$$

Here, the quantities are supposed to be axisymmetric : $\partial_\varphi P_a = 0$ and $\partial_\varphi \phi = 0$ with ϕ the electric potential. Also, the ion and impurity Ware fluxes are negligible compared to

neoclassical fluxes (for more detail, see p.1155 of Ref.[Hirshman and Sigmar, 1981]) so that the contribution of the induction field to E_φ can be ignored. Thus, $E_\varphi \simeq 0$ under these conditions.

Neoclassical transport is associated with poloidal asymmetries on magnetic flux surfaces. The neoclassical impurity particle flux across the flux surfaces is then $\Gamma_a^\psi = \langle \boldsymbol{\Gamma}_a \cdot \boldsymbol{\nabla}\psi \rangle$, where

$$\langle G \rangle \equiv \int \frac{G \mathrm{d}\theta}{\mathbf{B}\cdot\boldsymbol{\nabla}\theta} \Big/ \int \frac{\mathrm{d}\theta}{\mathbf{B}\cdot\boldsymbol{\nabla}\theta} \tag{5.48}$$

corresponds to a flux surface average of the quantity G.

By writing $\boldsymbol{\mathcal{R}}_a = \mathcal{R}_{\parallel,a}\mathbf{b} + \boldsymbol{\mathcal{R}}_{\perp,a}$, Equation (5.47) becomes

$$\Gamma_a^\psi = -\frac{I(\psi)}{e_a}\left\langle \frac{1}{B}\mathcal{R}_{\parallel,a} \right\rangle \tag{5.49}$$

The perpendicular friction force $\boldsymbol{\mathcal{R}}_{\perp,a}$ is responsible for the classical transport. It is neglected since the classical flux is small compared to the neoclassical flux at large aspect ratio [Hazeltine and Meiss, 2003]. The parallel friction force $\mathcal{R}_{\parallel,a}$ is to be written as a function of gradient lengths to derive the expression of the neoclassical radial flux. For this study, the plasma is supposed to contain a single type of impurity ion, and the impurity is considered as a trace ($\alpha_z \equiv N_z e_z^2/(N_i e_i^2) \ll 1$). For heavy impurities ($m_z/m_i \gg 1$), the friction force $\boldsymbol{\mathcal{R}}_z \simeq \boldsymbol{\mathcal{R}}_{zi}$ and its projection along the parallel direction is then written in the form [Helander and Sigmar, 2005][Braginskii, 1965][Rutherford, 1974]

$$\mathcal{R}_{\parallel,zi} = -m_z N_z \nu_{zi}(V_{\parallel,z} - V_{\parallel,i}) - \frac{2}{5}C_0 m_z N_z \nu_{zi}\frac{Q_{\parallel,i}}{P_i} \tag{5.50}$$

Here, $Q_{\parallel,i} = -\chi_{\parallel,i} N_i \boldsymbol{\nabla}_\parallel T_i$ is the parallel heat flux of the main ion species and ν_{zi} the collision frequency between the impurity and the main ion species.

It can be noticed that Ref.[Rutherford, 1974] adopted Braginskii's procedure for electron-ion collision [Braginskii, 1965] to derive the impurity flux in the Pfirsch-Schlüter regime. However, this computation considers both the impurity and the main ion species in the Pfirsch-Schlüter regime. In this case, the favourable thermal screening effect predicted by the neoclassical theory is not retrieved. This is why the adjustable coefficient C_0 is defined as a fluid closure. It is chosen in order to obtain the appropriate screening factor for the impurity Pfirsch-Schlüter flux with bulk ions in the low collisionality regime. In general, C_0 depends on the impurity strength parameter α_z, and is thus a radial function which is deduced from kinetic computations accounting for collisions [Estève et al., 2015][Estève, 2015]. Since our study deals with trace impurities only ($\alpha_z \ll 1$), C_0 can be chosen as a constant, and is calculated in the following section.

5.2.3 Derivation of impurity radial fluxes

Parallel fluxes

It is shown in the expression (5.49) that the perpendicular Pfirsch-Schlüter flux is associated with the parallel friction force. Hence, parallel velocities and heat fluxes have to be derived in order to deduce $\mathcal{R}_{\parallel,zi}$ according to the expression (5.50). For this, the assumption on fluid incompressibility is crucial. The perpendicular particle and heat flows are then balanced by parallel flows to ensure particle and heat conservation.

At the lowest order in δ and using the expressions (2.4) and (5.45), the particle velocity of species a reads

$$\mathbf{V}_a = K_a(\psi,\theta)\mathbf{B} - \frac{T_{a,0}}{e_a} A_{P_a^*,\psi} \mathsf{R}^2 \boldsymbol{\nabla}\varphi \tag{5.51}$$

where

$$A_{P_a^*,\psi} \equiv \partial_\psi \ln P_{a,0} + \frac{e_a}{T_{a,0}} \partial_\psi \phi_0 \tag{5.52}$$

and K_a is *a priori* a function of ψ and θ. In the neoclassical time scale, the continuity equation

$$\partial_t N_a + \boldsymbol{\nabla}\cdot\boldsymbol{\Gamma}_a = 0 \tag{5.53}$$

gives a divergence-free particle flux $\boldsymbol{\nabla}\cdot\boldsymbol{\Gamma}_a = 0$ for each species a. This yields the fluid incompressibility $\boldsymbol{\nabla}\cdot\mathbf{V}_a = 0$ as $N_a(\psi,\theta) \simeq N_{a,0}(\psi)$ at the lowest order in δ. Under this constraint, K_a needs to be a radial function. As a consequence, the parallel velocity of the species a is written as

$$V_{\parallel,a} = K_a(\psi) B - \frac{T_{a,0}}{e_a} \frac{I(\psi)}{B} A_{P_a^*,\psi} \tag{5.54}$$

Unlike for the particle flux $\boldsymbol{\Gamma}_a$, the assumption $\boldsymbol{\nabla}\cdot\mathbf{Q}_a = 0$ for each species a is not general. Indeed, the energy equation for the species a is written in the form

$$\partial_t(N_a\mathcal{S}_a) + \boldsymbol{\nabla}\cdot(N_a\mathcal{S}_a\mathbf{V}_a) = -\frac{2}{3}\frac{\boldsymbol{\nabla}\cdot\mathbf{Q}_a}{T_a} + \sum_b \mathcal{H}_{ab} \tag{5.55}$$

where $\mathcal{S}_a \equiv \ln(P_a N_a^{-\gamma})$ is the entropy, and $\mathcal{H}_{ab}$ is the energy exchange with another species b. Hence, even if the convective term $\boldsymbol{\nabla}\cdot(N_a\mathcal{S}_a\mathbf{V}_a)$ is negligible at lowest order in δ, only the total heat flux is divergence free (i.e. $\boldsymbol{\nabla}\cdot\sum_a \mathbf{Q}_a = 0$). Nevertheless, $\boldsymbol{\nabla}\cdot\mathbf{Q}_a = 0$ for each species a, if the energy exchanges due to collisions with other species $\sum_b \mathcal{H}_{ab}$ are negligible. This is the case for species with large mass disparity since the energy transfer term in the collision operator is proportional to the mass ratio [Helander and Sigmar, 2005]. In the case of plasmas with heavy impurities ($m_z/m_i \gg 1$), main ions and electrons, this assumption is valid.

The perpendicular heat flux reads

$$\mathbf{Q}_{\perp,a} = \frac{5}{2}\frac{P_a}{e_a}\frac{\mathbf{B}\times\boldsymbol{\nabla}T_a}{B^2} \tag{5.56}$$

Hence, at lowest order in δ, the heat flux can be written as

$$\mathbf{Q}_a = L_a(\psi)\mathbf{B} - \frac{5}{2}\frac{P_{a,0}}{e_a}\partial_\psi T_{a,0}\mathsf{R}^2\boldsymbol{\nabla}\varphi \tag{5.57}$$

where L_a is constant along magnetic flux surfaces because of the incompressible heat flux constraint $\boldsymbol{\nabla}\cdot\mathbf{Q}_a = 0$. Therefore, the parallel heat flux has the following form

$$Q_{\parallel,a} = L_a(\psi)B - \frac{5}{2}\frac{P_{a,0}}{e_a}\frac{I(\psi)}{B}\partial_\psi T_{a,0} \tag{5.58}$$

Impurity radial flux

With the expressions (5.54) and (5.58), the parallel friction force $\mathcal{R}_{\parallel,zi}$ can be expressed as a function of different radial derivatives. The force balance equation (5.46) projected along the parallel direction of the impurity z gives

$$N_z e_z \nabla_\parallel \phi = -\nabla_\parallel P_z + \mathcal{R}_{\parallel,zi} \tag{5.59}$$

It can be noticed that

$$\left\langle B\nabla_\parallel G\right\rangle = 0 \tag{5.60}$$

for a scalar function G, by definition of flux-surface average operator in Equation (5.48). Hence, averaging Equation (5.59) over flux surfaces, with $N_z \simeq N_{z,0}(\psi)$, gives the constraint

$$\left\langle B\mathcal{R}_{\parallel,zi}\right\rangle = 0 \tag{5.61}$$

From the expressions (5.50), (5.54) and (5.58), the perpendicular impurity particle flux then reads

$$\begin{aligned}\Gamma_z^\psi = -m_z N_{z,0} T_0 \nu_{zi}\frac{I(\psi)^2}{e_z^2}&\left[\left\langle\frac{1}{B^2}\right\rangle - \frac{1}{\langle B^2\rangle}\right]\\ &\left(\partial_\psi \ln P_{z,0} - \frac{e_z}{e_i}\partial_\psi \ln P_{i,0} + C_0\frac{e_z}{e_i}\partial_\psi \ln T_{i,0}\right)\end{aligned} \tag{5.62}$$

by considering the isothermal assumption $T_z \simeq T_i = T$.

For a geometry of circular concentric magnetic surfaces, it is known [Hinton and Hazeltine, 1976] that

$$I(\psi)^2\left[\left\langle\frac{1}{B^2}\right\rangle - \frac{1}{\langle B^2\rangle}\right] \simeq 2r^2 \tag{5.63}$$

in the limit of small inverse aspect ratio $\epsilon \ll 1$. Also, $\partial_r\psi = B_0 r/q$ in this approximation.

For highly-charged heavy impurities, $e_z/e_i \gg 1$ and the radial flux reads

$$\begin{aligned}\langle \boldsymbol{\Gamma}_z \cdot \boldsymbol{\nabla} r \rangle &= \left\langle \frac{q}{B_0 r} \Gamma_z^{\psi} \right\rangle \\ &= -D_z^{PS} N_{z,0} \left\{ \partial_r \ln N_{z,0} - \frac{e_z}{e_i} \partial_r \ln N_{i,0} + (C_0 - 1) \frac{e_z}{e_i} \partial_r \ln T_{i,0} \right\}\end{aligned} \tag{5.64}$$

with the Pfirsch-Schlüter diffusion coefficient $D_z^{PS} = 2\rho_z^2 q^2 \nu_{zi}$.

Depending on the value of the coefficient C_0 in the expression (5.64), the temperature gradient will reduce or enhance the impurity influx. For trace impurities (i.e. $\alpha_z \ll 1$), computations from the neoclassical theory show that $C_0 \simeq 1$ when the impurity and the main ion species are both in the Pfirsch-Schlüter regime [Rutherford, 1974]. In that case, the temperature gradient has no effect on the impurity radial flux. However, for the most common case of heavy impurities in the Pfirsch-Schlüter regime and the main ion species in the banana-plateau regime, the coefficient C_0 is predicted to be $C_0 = 3/2$ in Ref.[Hirshman and Sigmar, 1981]. The ion temperature gradient then drives a favourable thermal screening effect. For this study, $C_0 = 3/2$ is set in the expression (5.50) of the collisional force to reproduce the appropriate neoclassical prediction.

Poloidal asymmetry of impurity density

The derivation of the Pfirsch-Schlüter fluxes in this section is done under the assumption of small poloidal asymmetries compared to surface averaged quantities. With the expressions (5.50), (5.54), (5.58) and the constraint (5.61), the parallel friction force reads, in the small inverse aspect ratio limit $\varepsilon = r/R_0 \ll 1$,

$$\mathcal{R}_{\parallel,zi} = m_z N_{z,0} \nu_{zi} \frac{T_0}{e_z} \left(\partial_\psi \ln P_{z,0} - \frac{e_z}{e_i} \partial_\psi \ln P_{i,0} + C_0 \frac{e_z}{e_i} \partial_\psi \ln T_{i,0} \right) 2r \cos\theta \tag{5.65}$$

by writing $B = B_0/(1 + \varepsilon \cos\theta)$ and $I = B_0 \mathsf{R}_0$. In this limit, the parallel gradient can be written as $\nabla_\parallel = 1/(q\mathsf{R}_0)\partial_\theta$.

If only the poloidal asymmetry of impurity density is considered, the parallel projection of the force balance equation (5.59) reads

$$\frac{1}{q\mathsf{R}_0} \frac{\partial_\theta N_z}{N_{z,0}} = -\frac{2q}{\mathsf{R}_0} \frac{\nu_{zi}}{\omega_{c,z}} \left[\frac{\mathsf{R}_0}{L_{N_z}} + \frac{e_z}{e_i} \frac{\mathsf{R}_0}{L_{N_i}} - (C_0 - 1) \frac{e_z}{e_i} \frac{\mathsf{R}_0}{L_{T_i}} \right] \cos\theta \tag{5.66}$$

where $L_Y \equiv |\partial_r \ln Y|^{-1}$ is the gradient length of the quantity Y. The integration of the expression (5.66) along θ for highly-charged heavy impurities ($e_z/e_i \gg 1$) gives

$$\frac{N_{z,1}}{N_{z,0}} = -2q^2 \frac{e_z}{e_i} \frac{\nu_{zi}}{\omega_{c,z}} \left[\frac{\mathsf{R}_0}{L_{N_i}} - (C_0 - 1) \frac{\mathsf{R}_0}{L_{T_i}} \right] \sin\theta \tag{5.67}$$

Hence, the ordering used to derive the Pfirsch-Schlüter fluxes in Equation 5.62 reads

$$2q^2\frac{e_z}{e_i}\frac{\nu_{zi}}{\omega_{c,z}}\left|\frac{\mathsf{R}_0}{L_{N_i}}-(C_0-1)\frac{\mathsf{R}_0}{L_{T_i}}\right|\ll 1 \tag{5.68}$$

It should be noted that the relative level of poloidal asymmetry of the impurity density $N_{z,1}/N_{z,0}$ is proportional to the parameter $\delta \ll 1$. However, the assumption of small poloidal asymmetries is far from being satisfied. Indeed, $N_{z,1}/N_{z,0}$ is also proportional to the square of the safety factor q^2, the impurity charge and the ion density and temperature gradient lengths. Therefore, the assumption becomes easily invalid in the edge region, where the safety factor values can go up to $q \simeq 5$ or more, and the ion density and temperature gradients are steep. In the core region, $q \simeq 1$ and the ion density and temperature gradient lengths are usually large. Hence, the validity condition is fulfilled in the framework of this study.

5.3 Numerical studies with the XTOR-2F code

5.3.1 Numerical methods

Implementation in the XTOR-2F code

In addition to Equations (2.45), (2.46), (2.47) and (2.48) of the XTOR-2F code, fluid equations for the considered impurity are implemented and coupled with them, as explained in Chapter 2

$$\partial_t N_z + \boldsymbol{\nabla}\cdot(N_z\mathbf{V}_z) = \boldsymbol{\nabla}\cdot(D_{\perp,z}\boldsymbol{\nabla}N_z - \mathbf{V}_{p,z}N_z) + S_z \tag{5.69}$$

$$N_z m_z\left(\partial_t V_{\parallel,z} + (\mathbf{V}_z\cdot\boldsymbol{\nabla})V_{\parallel,z}\right) = -\nabla_\parallel P_z + N_z e_z E_\parallel + \mathcal{R}_{\parallel,zi} \tag{5.70}$$

where $\mathbf{V}_z$ is the impurity fluid velocity as defined in (5.45), $D_{\perp,z}$ and $\mathbf{V}_{p,z}$ are the perpendicular impurity diffusion coefficient and radial pinch velocity, S_z is the impurity density source, and $\mathcal{R}_{\parallel,zi}$ is the parallel friction force represented in (5.50). The impurity pressure is $P_z = N_z T$, by assuming $T = T_z = T_i$ due to collisional thermalization.

It is necessary to have $\boldsymbol{\nabla}\cdot\mathbf{Q}_i = 0$ to derive the expression (5.58) for the main ion species. However, the energy equation (2.47) is written for the total pressure $P = P_e + P_i$ in the current XTOR-2F model, which would only give $\boldsymbol{\nabla}\cdot(\mathbf{Q}_e + \mathbf{Q}_i) = 0$. In this case, it is not straightforward to deduce the ion heat flux incompressibility from the current energy equation (2.47). Moreover, the contribution of the diamagnetic heat flux becomes negligible in the expression of $\mathbf{Q}_e + \mathbf{Q}_i$ for $T_e \simeq T_i$ and $N_e \simeq N_i$, because of opposite charge numbers. Therefore, an additional equation for the main ion species is added

$$\begin{aligned}\partial_t P_i + \mathbf{V}\cdot\boldsymbol{\nabla}P_i + \frac{\gamma}{e_i}\boldsymbol{\Xi}\cdot\boldsymbol{\nabla}(P_i T_i)& \\ = (\gamma-1)\left[\boldsymbol{\nabla}\cdot(N\chi_{\parallel,i}\nabla_\parallel T_i\mathbf{b}) + \boldsymbol{\nabla}\cdot(N\chi_{\perp,i}\boldsymbol{\nabla}_\perp T_i)\right] + S_{H_i}&\end{aligned} \tag{5.71}$$

Here, the source term S_{H_i} is set to

$$S_{H_i} = \frac{\tau}{Z_i + \tau} S_H \tag{5.72}$$

with $\tau = T_i/T_e$, in order to have a heat source consistent with the total heat source S_H of Equation (2.47).

The mesh used in the following simulations is $(M_r, M_\theta, M_\phi) = (255, 32, 12)$, where M_r, M_θ, M_ϕ are the number of grid points in r, θ, ϕ directions respectively. A total of 4 toroidal modes ($n = 0$, ..., 3) and $n + 8$ poloidal modes ($m = 0$, ..., $n + 7$) for each toroidal mode, are evolved in the simulations.

Plasma parameter settings and initial conditions

As mentioned in Chapter 2, the Lundquist number is rescaled to $S = 10^7$ for the XTOR-2F sawtooth simulations. Other plasma parameters are rescaled so as to preserve the ratios between different characteristic time scales with respect to experimental values. The diamagnetic parameter is then set to $\bar{d}_i = 0.1$, which is about two or three times larger than the experimental values. Also, the normalized perpendicular heat diffusivity is set to $\bar{\chi}_\perp = 3 \times 10^{-6}$. The products $S\bar{d}_i$ and $S\bar{\chi}_\perp$ are then about a third of those expected from the experiments. As far as the viscosity is concerned, measurements of this quantity in experiments are not available. In this paper, the normalized plasma viscosity is set to $\bar{\mu} = 5 \times 10^{-6}$, so that the magnetic Prandtl number is $Pr_m = S\bar{\mu} = 50$. The parameter $\tau \equiv P_i/P_e$ becomes $\tau = T_i/T_e$ under the quasi-neutrality constraint $N_e = N_i$. In the following simulations, electron and ion temperatures are equal, i.e. $\tau = 1$. It should be noted that this is usually not the case in experiments as different auxiliary heatings are added. The initial density and temperature profiles used for the present study are shown in Figure 5.4-a. For the following simulations, a flat initial impurity density profile is set. The main ion density is normalized to the on-axis density value $N_0 = 3 \times 10^{19}\,\mathrm{m}^{-3}$. The impurity is considered as a trace in the simulations, with a concentration $Nz, 0/N_0 = 10^{-5}$ such that the bulk MHD dynamics is not affected. The normalized impurity density is $\bar{N}_z = 1$ with $\bar{N}_z \equiv N_z/N_{z,0}$.

In the present XTOR-2F model, the transport coefficients $D_{\perp,z}$ and $\mathbf{V}_{p,z}$ on the right hand side of the impurity density equation (5.69) include the contributions of turbulent, classical and neoclassical transport. However, calculations of Section 5.2.3 show that a Pfirsch-Schlüter impurity flux is driven by poloidal asymmetries. Thus, it is important to notice that the Pfirsch-Schlüter particle flow is intrinsically present in the $\boldsymbol{\nabla} \cdot \boldsymbol{\Gamma}_z = \boldsymbol{\nabla} \cdot (N_z \mathbf{V}_z)$ term of Equation (5.69). Hence, the neoclassical part of the coefficients $D_{\perp,z}$ and $\mathbf{V}_{p,z}$ contain only the classical and the banana-plateau coefficients. In Figure 5.4-b, the red dashed line represents the diffusion coefficient $D_{\perp,z}$ on the right hand side of Equation (5.69) which is set to reproduce the experimental radial shape. Indeed, this diffusion coefficient profile is based on fluctuation measurements which show that the turbulence intensity is small inside the $q = 1$ surface [Mattioli et al., 1998][Guirlet et al., 2010]. The blue solid line in Figure

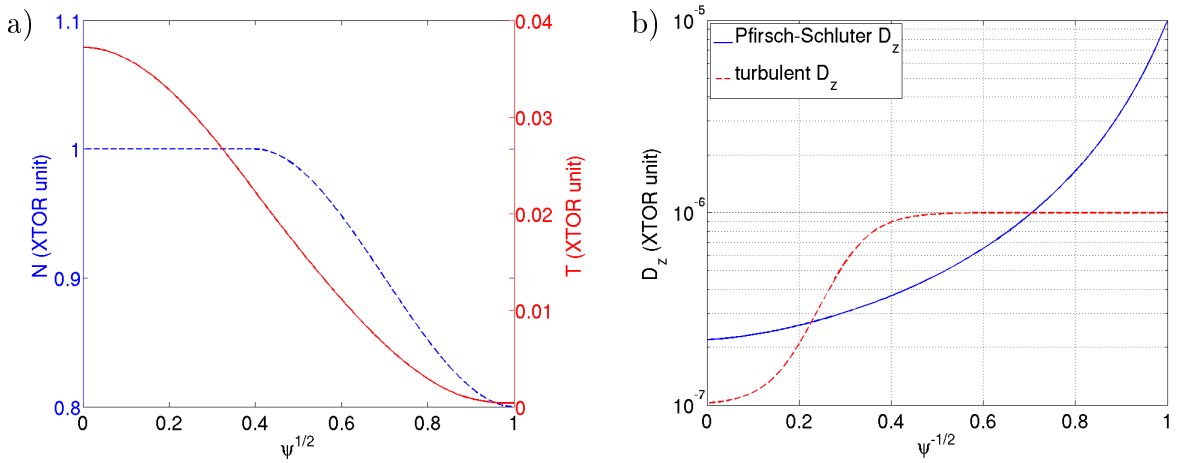

Figure 5.4: (a) The initial density (*blue line*) and temperature (*red line*) profiles used in the simulations. (b) The initial diffusion profile set to represent the turbulent transport (*red line*), and the initial Pfirsch-Schlüter diffusion profile (*blue line*) computed intrinsically from the impurity fluid equations.

5.4-b corresponds to the Pfirsch-Schlüter diffusion coefficient computed from the poloidal asymmetries as shown in Section 5.2.3. It can be noticed that the proportionality to q^2 of the diffusion coefficient in the Pfirsch-Schlüter regime is recovered in the limit of $\epsilon \ll 1$ as shown by Equation (5.64) of the radial flux. The 'turbulent' diffusion coefficient is chosen such that it has the same order of magnitude compared to the Pfirsch-Schlüter diffusion coefficient in the core region. The neoclassical impurity pinch velocity in the Pfirsch-Schlüter regime, depending on the main ion density and temperature gradient lengths, is taken into account by the model. However, the 'turbulent' pinch velocity $\mathbf{V}_{p,z}$ on the right hand side of Equation (5.69) is set to zero in this study.

In the simulations, fully-stripped carbon (C^{6+}) is chosen as the impurity species. The impurity is present as a trace, without any feedback on MHD quantities. Using carbon ion allows one to avoid accounting for centrifugal force and radiation. As high-Z impurities are in a highly collisional regime, the collisionality of carbon ion is rescaled to a large value such that it is in the Pfirsch-Schlüter regime. The results are expected to be the same for tungsten provided it behaves as a tracer, and centrifugal and radiation effects are negligible.

5.3.2 Simulation results

Temperature screening effect from thermal force

It was shown in Section 5.2.3 that the Pfirsch-Schlüter impurity flux is related to the collisional force $\boldsymbol{\mathcal{R}}_{zi}$ between the main ion species and the impurity. Moreover, the expression of the impurity radial flux in Equation (5.64) shows that the drag force and the thermal force give respectively the appropriate contributions of the main ion density gradient and the temperature gradient. In a first step, simulations without the internal kink mode are performed in order to verify whether the implemented model reproduces expected features

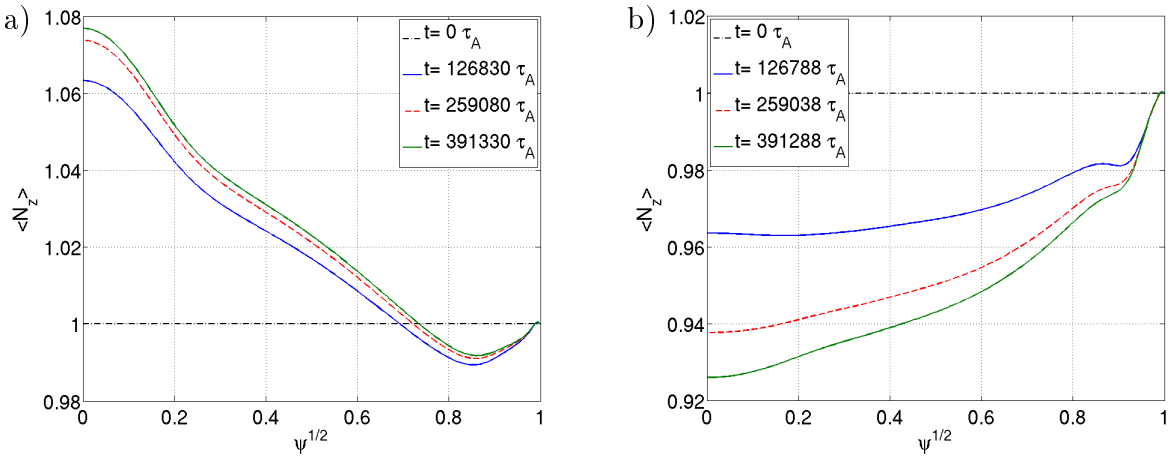

Figure 5.5: Evolution of the impurity profiles for the cases (a) without thermal force ($C_0 = 0$), and (b) with an appropriate coefficient for the thermal force ($C_0 = 3/2$) as predicted by the neoclassical theory. The temperature screening effect appears in presence of the thermal force.

of the radial impurity flux.

To illustrate this point, cases with and without thermal force are simulated by setting appropriate values of the coefficient C_0 in the expressions of the parallel friction force (5.50) and the impurity radial flux (5.64). With the density and temperature profiles presented in Figure 5.4-a, an influx of impurity is obtained by considering only the drag force ($C_0 = 0$). For the case with thermal force, the coefficient C_0 is set to $C_0 = 3/2$, so that an outward flux of impurity appears due to the temperature screening effect, as predicted in Ref.[Hirshman and Sigmar, 1981]. In Figure 5.5, the time evolution of the flux surface average of the impurity density profile is presented for the two cases. These figures show that the impurity radial fluxes behave in accordance with the analytical calculations.

Effects of sawtooth oscillations on impurity transport

With the rescaled plasma parameters mentioned in the previous paragraph, sustained sawtooth cycles are obtained with the XTOR-2F code (Figure 5.6). These simulations are used to assess the impurity behaviour in sawtoothing plasmas. The neoclassical time scales are very large compared to the duration of sawtooth crashes. Hence, the temperature screening effect, resulting from the collisions between the main ion species and the impurity, affects the impurity dynamics only during the sawtooth ramp phase.

The evolution of the surface averaged impurity profiles throughout the sawtooth cycles is presented in Figure 5.7-a. The impurity profiles are those between the post-cursor and precursor oscillations of a sawtooth cycle. It is noticed again that when the temperature screening effect is taken into account, an impurity outflow is driven throughout the sawtooth cycles. However, a clear difference on the impurity behaviour is seen between the simulations with and without sawteeth (Figure 5.7-b). The surface averaged impurity profiles after $t \simeq 3.2 \times 10^5\, \tau_A$ at a quasi-stationary state, show that the impurity profiles get flatter in the

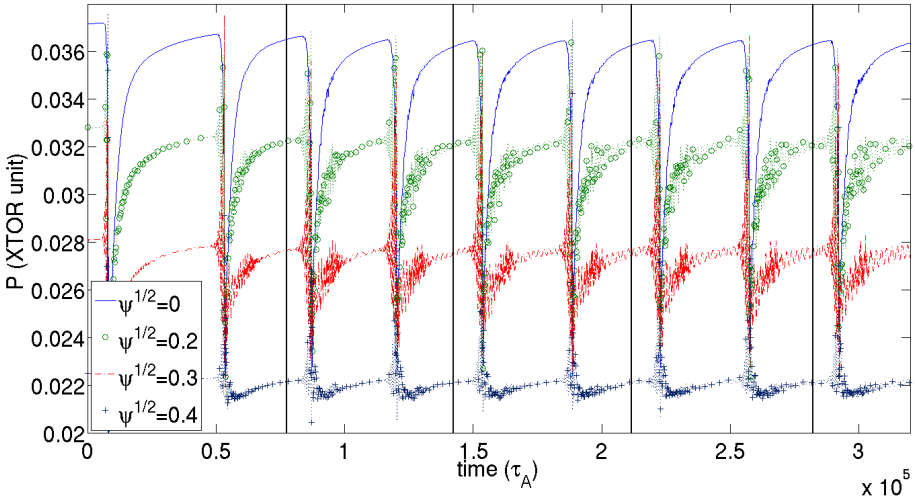

Figure 5.6: Evolution of the pressure at different radii. The time points which correspond to the surfaces averaged impurity profiles in Figure 5.7-a are marked by the vertical lines. These time points are chosen during the quiescent phase when the plasma has reached a quasi-stationary equilibrium.

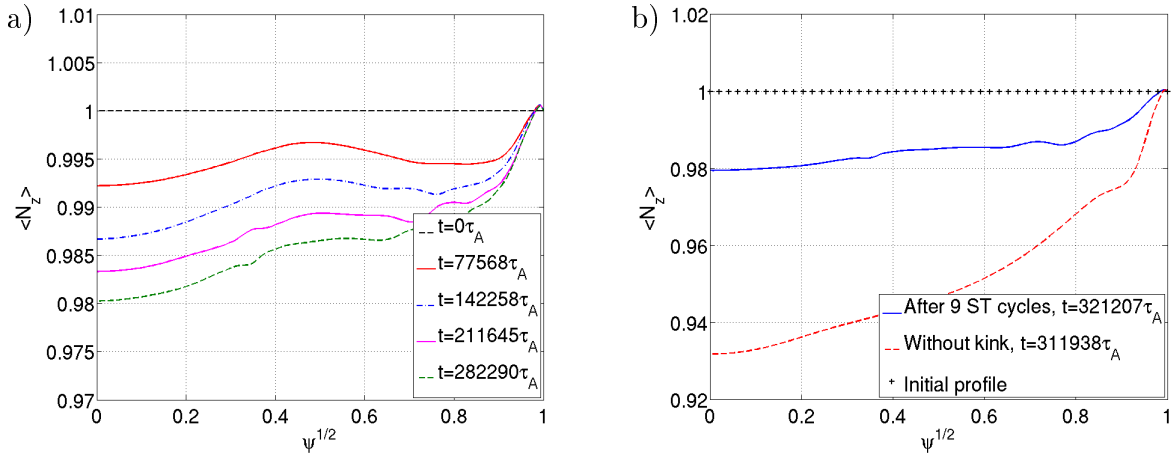

Figure 5.7: (a) Evolution of the surface averaged impurity density throughout the sawtooth cycles. The profiles correspond to the times marked by the vertical lines in Figure 5.6. (b) Comparison of the surface averaged impurity density profiles between the cases with (*blue line*) and without (*red line*) sawteeth after $t \simeq 3.2 \times 10^5\, \tau_A$ from the initial profile (+). The presence of sawtooth cycles decreases the quantity of impurities expelled from the core region.

presence of sawteeth. Indeed, the central impurity density has decreased by about 2% for the case with sawteeth, which is less than a third of what is obtained for the case without sawteeth.

The weakened temperature screening effect is partly related to the time averaged temperature profile which is less peaked than the initial temperature profile. This is due to a periodic flattening of the temperature profile at sawtooth crashes [Porcelli et al., 1996]. Hence, the overall radial pinch velocity of the impurity is less important than in the case

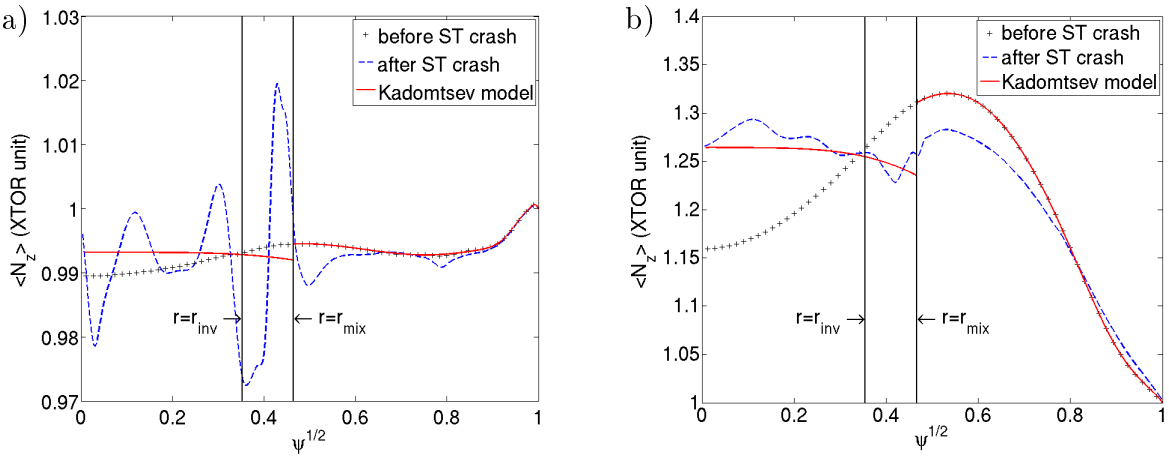

Figure 5.8: Impurity profiles after sawtooth crash for (a) shallow and (b) hollow pre-crash profiles (+). Post-crash impurity profiles computed by the XTOR-2F code (*blue lines*) and with Kadomtsev reconnection model (*red lines*) are shown. The inversion radius r_{inv} and the mixing radius r_{mix} are marked by vertical lines. For a pre-crash profile with more contrasted hollowness, the penetration of impurity is clearly visible and is in accordance with the Kadomtsev reconnection model.

without sawteeth, where the temperature profile remains unchanged. Also, the particle redistribution during the sawtooth crash tends to weaken the impurity outflow. Indeed, sawtooth crashes drive an efficient radial transport of impurities. In particular, the Kadomtsev reconnection model [Kadomtsev, 1975][Furno et al., 2001] predicts an influx of impurity during sawtooth crashes for a hollow pre-crash impurity profile [Ödblom et al., 1996], regardless of its steepness (Figure 5.8). However, in the XTOR-2F simulations, a density flutter of about 5% is found in the impurity profiles after a sawtooth crash (blue dashed lines). Impurity penetration is not as visible as predicted by the Kadomtsev reconnection model, if the pre-crash impurity density profile is flatter than the corrugations due to the crash (Figure 5.8-a). On the contrary, the impurity profile after a sawtooth crash obtained by the XTOR-2F code is consistent with Kadomtsev's prediction for a hollow pre-crash profile (Figure 5.8-b). The radial redistribution of particles due to sawtooth crashes is sufficient to weaken the outward impurity flux compared to the case without sawteeth, although the impurity profiles in the present study are almost flat.

5.3.3 Correlation of impurity dynamics with convective cells

In this paragraph, the mechanisms that underlie the impurity transport during a crash are investigated in more detail. For this purpose, different time points during a sawtooth crash are selected and marked by vertical lines in Figure 5.9-a. The corresponding magnetic configurations are displayed as Poincaré plots in Figures 5.9-b to 5.9-f. In Figure 5.10, the impurity density that corresponds to the time points marked in Figure 5.9-a are shown in color background. As the electron mass is very small compared to the ion mass, electron heat conduction is expected to be faster than the ion convection. Thus, the temperature contours

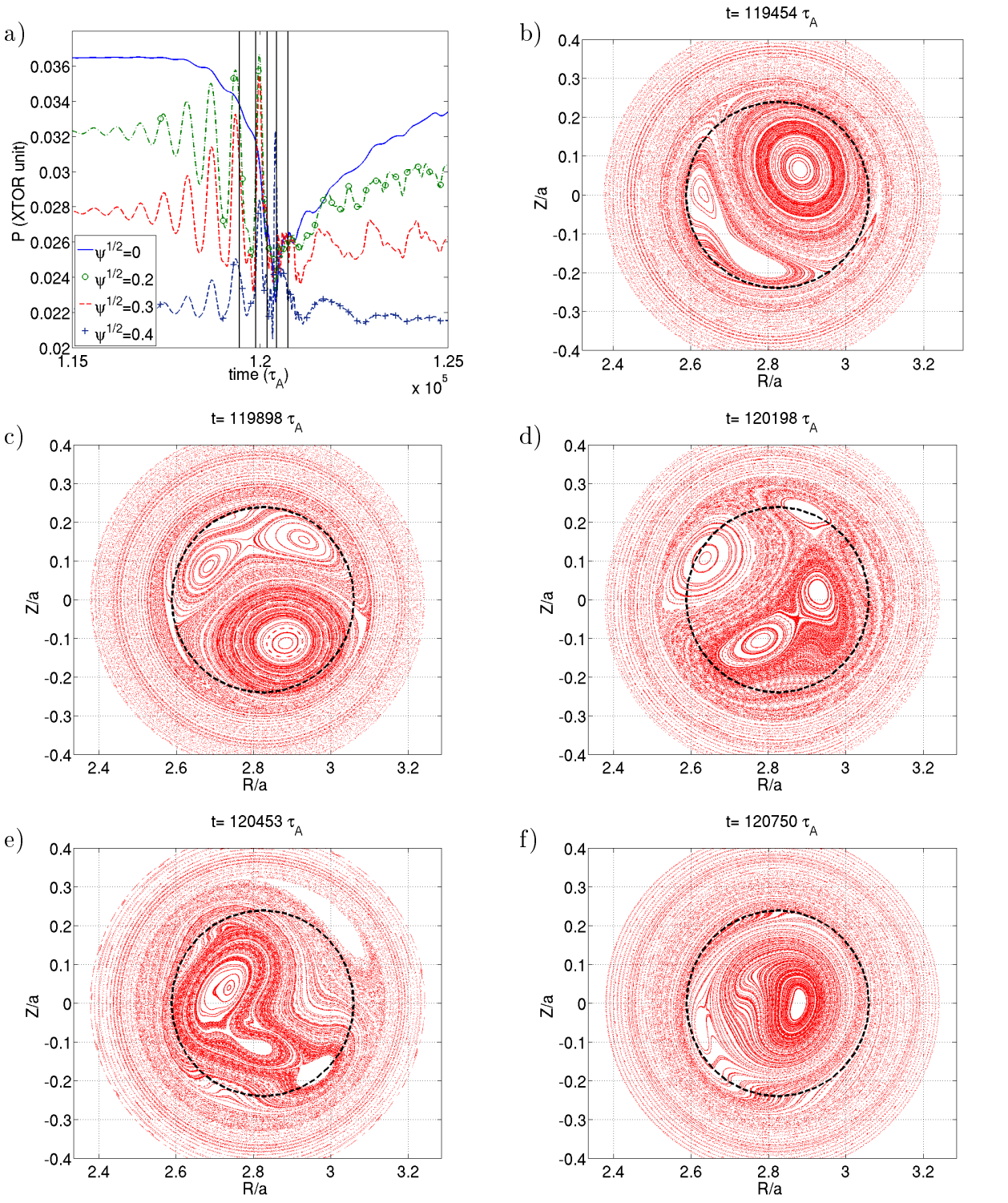

Figure 5.9: (a) Time evolution of pressure at different radii during sawtooth crash and (b)-(f) Poincaré of the core region ($r/a < 0.6$) plots corresponding to the time points marked by vertical lines. The $q = 1$ surface is represented by dashed lines.

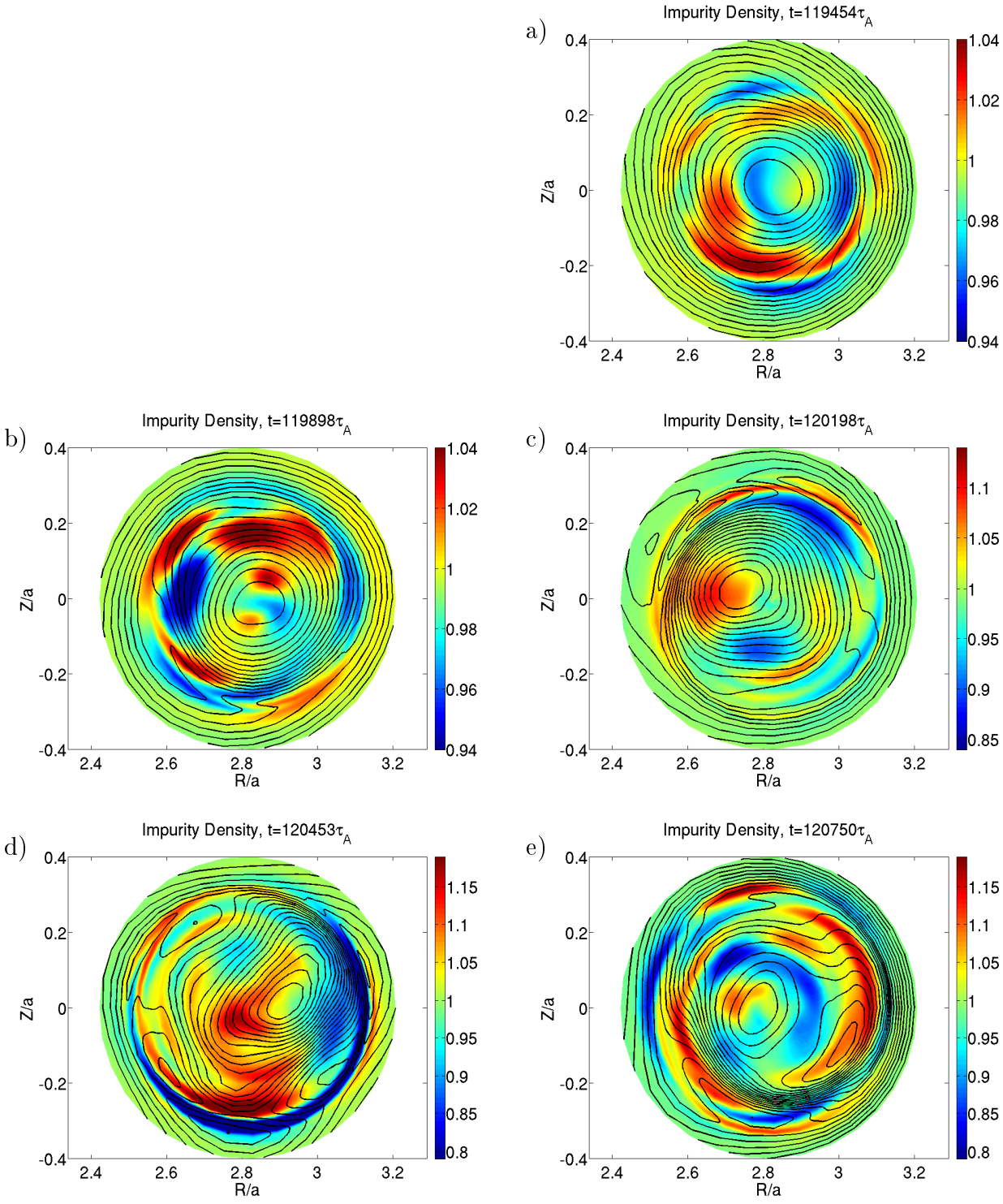

Figure 5.10: Impurity density structures during the sawtooth crash in the background and the electric potential ϕ in contour lines. Each figure corresponds respectively to Poincaré plots of Figure 5.9-b to 5.9-f.

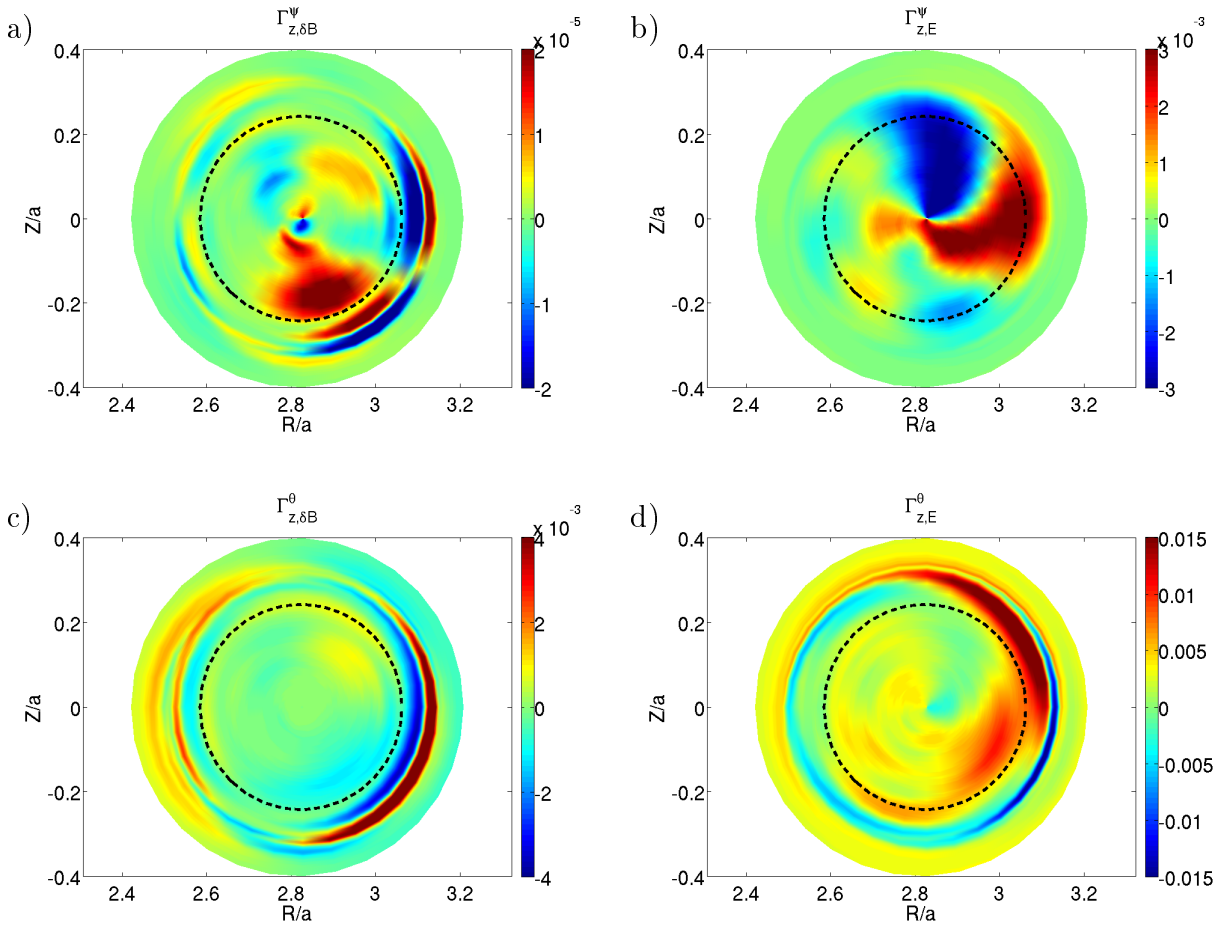

Figure 5.11: The radial and poloidal components (a) $\Gamma^{\psi}_{z,\delta B}$, (b) $\Gamma^{\psi}_{z,E}$, (c) $\Gamma^{\theta}_{z,\delta B}$ (d) $\Gamma^{\theta}_{z,E}$ of the parallel impurity flux $\mathbf{\Gamma}_{z,\delta B}$ and the impurity flux driven by the $\mathbf{E}\times\mathbf{B}$ velocity $\mathbf{\Gamma}_{z,E}$, corresponding to $t \simeq 1.205\times10^5\,\tau_A$ (Figure 5.10-d) are represented in the poloidal plane at $\varphi = 0$. The dashed lines represent the $q = 1$ surface.

are often considered as a representation of magnetic surfaces. Unlike for the ion species, the convection perpendicular to magnetic surfaces also has to be considered. The contour lines which represent the reconstructed stream function associated with the $\mathbf{E}\times\mathbf{B}$ velocity are also shown in Figure 5.10.

It can be noticed that the impurity density structures shown in Figure 5.10 bear similarities with the patterns in the Poincaré maps of the field line (Figure 5.10), with a slight poloidal shift. This is an indication of the role of the parallel dynamics, which tends to align the impurity density structures with the magnetic topology. At the same time, it can also be seen that the orientation of these structures is reminiscent of the $\mathbf{E}\times\mathbf{B}$ velocity field. These structures are driven by the $\mathbf{E}\times\mathbf{B}$ flow. For example, in Figure 5.10-b, the impurity density bump and hole located respectively at $\theta \simeq \pi/2$ and $\theta \simeq \pi$, are more or less similar to magnetic surfaces in the island (Figure 5.9-c). These same structures are then rotated along the reconstructed streamlines (Figures 5.10-b,c).

Since it is difficult to establish the relative roles of parallel and $\mathbf{E}\times\mathbf{B}$ flows using maps, another method is adopted here. It is based on the comparison of the two components of

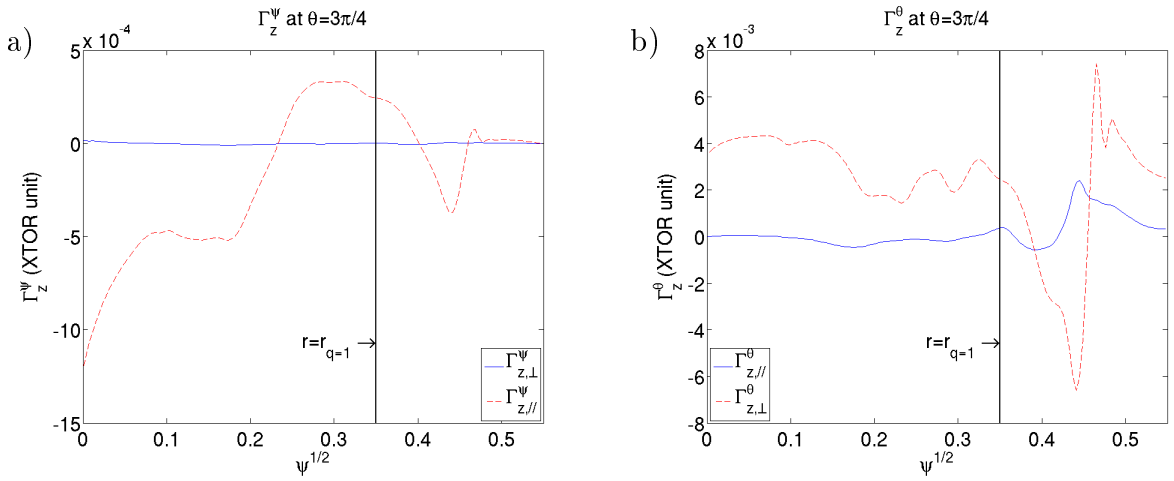

Figure 5.12: The profiles at $(\theta, \varphi) = (3\pi/4, 0)$ of the (a) radial and (b) poloidal components of the impurity flux along the magnetic field line $\mathbf{\Gamma}_{z,\delta B}$ (*blue lines*) and the flux driven by $\mathbf{E} \times \mathbf{B}$ velocity $\mathbf{\Gamma}_{z,E}$ (*red lines*). The $q = 1$ radius is marked by vertical lines.

the impurity flux. This approach provides quantitative correlations of the impurity density structures with magnetic flutter and $\mathbf{E} \times \mathbf{B}$ convection. From the expression (5.45) of the velocity, the impurity fluxes parallel and perpendicular to the magnetic surfaces respectively reads

$$\mathbf{\Gamma}_{z,\delta B} = N_z V_{z,\parallel} \frac{\widetilde{\mathbf{B}}_1}{B} \tag{5.73}$$

and

$$\mathbf{\Gamma}_{z,E} = N_z \mathbf{V}_E \tag{5.74}$$

The impurity flux driven by the diamagnetic velocity is neglected since $Z \gg 1$ for heavy impurities.

In Figure 5.11, the radial and poloidal components $\left(\Gamma^{\psi}_{z,\delta B}, \Gamma^{\theta}_{z,\delta B}\right)$ and $\left(\Gamma^{\psi}_{z,E}, \Gamma^{\theta}_{z,E}\right)$ in the poloidal section at $\varphi = 0$, are represented, by defining

$$\Gamma^{x}_{z,y} \equiv \mathbf{\Gamma}_{z,y} \cdot \boldsymbol{\nabla} x \tag{5.75}$$

These fluxes are calculated at time $t \simeq 1.205 \times 10^5 \, \tau_A$ (Figure 5.11), when the magnetic reconnection process during sawtooth crash has almost ended. At this time, the expelled hot core is located outside the $q = 1$ surface, and the cooler island occupies a large part of the core region (Figure 5.9-e). Also, complex impurity density structures are seen inside the $q = 1$ surface (Figure 5.10-d). It appears that $\Gamma^{\psi}_{z,E} \gg \Gamma^{\psi}_{z,\delta B}$ and $\Gamma^{\theta}_{z,E} \gg \Gamma^{\theta}_{z,\delta B}$ in most of the core region, i.e. the $\mathbf{E} \times \mathbf{B}$ flux overcomes the magnetic flutter flux in all directions. However, in some specific locations, e.g. $\pi/2 < \theta < \pi$ and outside the inversion radii, $\Gamma^{\psi}_{z,E} \simeq \Gamma^{\psi}_{z,\delta B}$ and $\Gamma^{\theta}_{z,E} \simeq \Gamma^{\theta}_{z,\delta B}$ (Figures 5.11, 5.12). Hence, the impurity structures during the sawtooth crash are driven by the two fluxes, but the $\mathbf{E} \times \mathbf{B}$ velocity plays a prominent role in most locations during sawtooth crashes.

In Ref.[Nagayama et al., 1991], soft X-ray (SXR) and temperature measurements are

analysed in detail during a sawtooth crash. The presence of the background metal impurities allows the impurity behaviour to be deduced from SXR emission. It is shown that a SXR emission peak is expelled out of the $q = 1$ surface during a sawtooth crash, along with the hot core. However, SXR and temperature contours become uncorrelated after the sawtooth crash. Particles escape from the reconnection layer during the sawtooth crash and are transported with their respective thermal velocity. Hence, the impurity transport time scale is large compared to the electron one which can be associated with the modifications of the magnetic configuration [Wesson et al., 1997]. The impurity behaviour during a sawtooth crash obtained by the XTOR-2F code is consistent with this picture. Indeed, the impurity density structures are not representative of magnetic flux surfaces, and they are spread along streamlines associated with the $\mathbf{E} \times \mathbf{B}$ velocity.

As a consequence, the impurity density bump and hole result from the time lag between impurity and electron transport.

5.4 Towards comparison with experiments

In the experimental scenarios analysed in Chapter 4, the dynamics of sawteeth are modified and the saturated helical state is obtained by adding ECCD sources. XTOR-2F simulations of the saturated helical state is then necessary in order to investigate the effects of the modified bulk plasma dynamics on the impurity behaviour in the core region, as observed in ASDEX-Upgrade discharges.

A model of ECCD source has been developed and implemented in the XTOR-2F code for magnetic island control [Février, 2016], in parallel to the present model of impurity transport [Ahn et al., 2016b]. Starting with a geometry of circular concentric magnetic surfaces [Halpern et al., 2011b], XTOR-2F simulation results show that the dynamics of sawteeth is modified by adding a radially localized ECCD source [Février et al., 2017]. These are consistent with the experimental observations previously reported [Furno et al., 2001][Angioni et al., 2003]. In particular, when the ECCD source is localized near the inversion radius ($r_{RF} \simeq 0.9\, r_{inv}$), the precursor phase lasts more than half a sawtooth period, as shown in Figure 5.13. Indeed, the time evolution of the pressure shows that the shape of sawteeth is changed as soon as the ECCD source is switched on at $t \simeq 9.8 \times 10^4\, \tau_A$. These long-living helical oscillations of the hot core simulated by the XTOR-2F code are reminiscent of the saturated internal kink mode in ASDEX-Upgrade scenarios described in Chapter 4. Here, the current driven by the ECCD source is set equal to 1% of the total plasma current, which is the order of magnitude necessary to control sawteeth [Hender et al., 2007].

The impurity behaviour in presence of the saturated helical state is then studied using the model implemented in the XTOR-2F code and described in this chapter. In this simulation, a partially stripped tungsten ion ${}^{184}_{74}\mathrm{W}^{45+}$ is considered. Tungsten is supposed to be present as a tracer ($N_W/N_e = 10^{-5}$) and the effect of toroidal rotation is again neglected.

Figure 5.14 represents the initial impurity density profile and surface averaged impurity

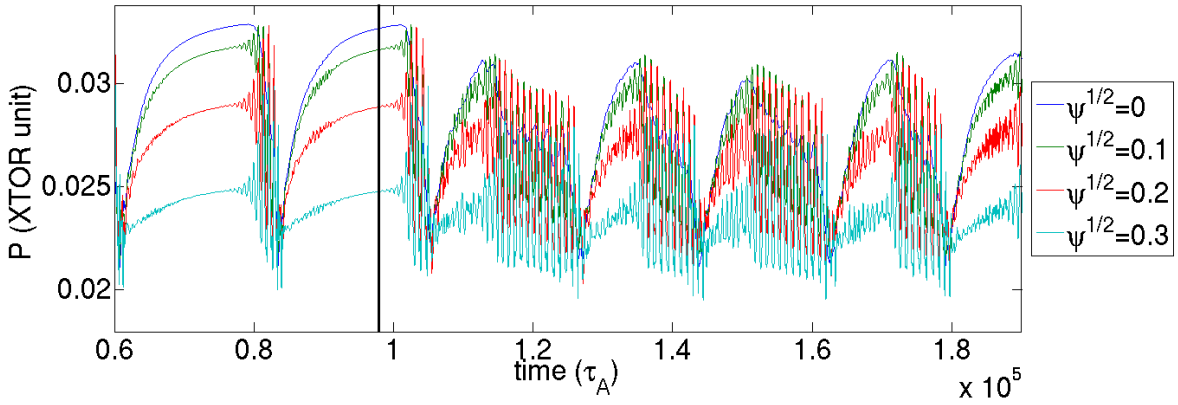

Figure 5.13: Time evolution of the pressure at different radii. An ECCD source localized near the inversion radius ($r_{RF} \simeq 0.9\, r_{inv}$) is added at $t \simeq 9.8 \times 10^4\, \tau_A$, marked by the vertical line. A change of sawtooth shape is clearly visible.

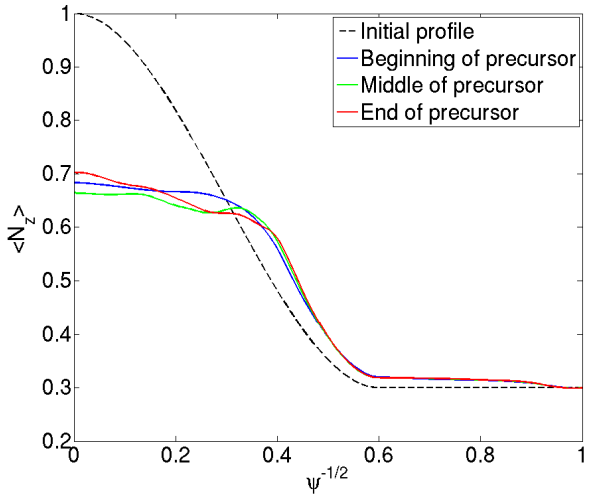

Figure 5.14: Surface averaged impurity density profiles at the beginning ($t \simeq 1.7 \times 10^5\, \tau_A$, *blue*), middle ($t \simeq 1.75 \times 10^5\, \tau_A$, , *green*) and end ($t \simeq 1.8 \times 10^5\, \tau_A$, *red*) of precursor oscillations. The impurity density profiles are flat in the core region during the helical oscillations, despite the peaked initial profile (*black dashed lines*).

density profiles at different phases of the precursor of a single sawtooth period ($1.6 \times 10^5\, \tau_A < t < 1.8 \times 10^5\, \tau_A$). These surface averaged profiles are also time averaged during one helical cycle. Here, the initial tungsten profile is peaked in order to be consistent with the ASDEX-Upgrade experiment. It should be noted that the initial impurity density profile is almost recovered before the next sawtooth crash for ordinary sawtooth cycles. However, it can be seen in Figure 5.14 that the impurity density profile is flat in the core region, in presence of long-living precursor oscillations. Therefore, these preliminary simulation results show that the overall impurity content is weaker in presence of the long-living helical state.

These simulations which are to some extent representative of the ASDEX-Upgrade discharges show that the saturated helical state is responsible for tungsten depletion in the core region. Still, hollow impurity density profiles as observed in ASDEX-Upgrade (Figure 4.10) have not been reproduced so far.

5.5 Summary

Appropriate fluid equations for impurities in the Pfirsch-Schlüter regime have been implemented in the XTOR-2F code in order to investigate the combined effect of neoclassical transport and sawtooth crashes. An analytical calculation shows that the neoclassical impurity flux in the Pfirsch-Schlüter regime is recovered by adjusting the friction between the impurity and the main ion species.

It has been numerically verified that the impurity radial fluxes obtained with this model are consistent with neoclassical predictions. The simulations show that the presence of sawtooth crashes changes the impurity thermal screening. Indeed, the time averaged outward impurity flux is weaker in presence of sawteeth. This is mainly due to a sudden influx of impurity during the sawtooth crash for hollow pre-crash profiles. It is consistent with the observations presented in Chapter 4, where tungsten density profile is regularly flattened in the core region after each sawtooth crash. Also, periodic flattening of the core temperature profile weakens the thermal screening effect during the recovery phase. Impurity density flutter in the percent range persists after each sawtooth crash. This makes it difficult to assess the agreement with the predictions of the Kadomtsev model for weakly hollow impurity profiles. Nevertheless, the long time scale behaviour is definitely consistent with a weaker thermal screening effect.

Impurities are transported across the $q = 1$ surface via the dynamics of density bump and hole which appear during sawtooth crashes. These structures are shown to be mainly driven by the $\mathbf{E}\times\mathbf{B}$ flow in the core region. Impurities are more sensitive to $\mathbf{E}\times\mathbf{B}$ flows than magnetic flutter because their fluid velocity along the field lines is very small. This is to be contrasted with electrons which move fast along the magnetic field so that magnetic flutter is the dominant electron transport mechanism. Hence, impurity transport is controlled by $\mathbf{E}\times\mathbf{B}$ vortices that cross the $q = 1$ surface during the reconnection process.

Finally, the presence of a saturated helical state in the core region flattens the impurity density profile during the whole duration of the precursor, i.e. flushes out more efficiently than ordinary sawtooth cycles. However, the impurity transport model has to be further improved since hollow impurity density profiles as observed in the ASDEX-Upgrade discharge are not reproduced.

CHAPTER 6

Conclusion

The production of sustained electricity using Deuterium-Tritium fusion reactions offers a promising alternative to present sources of electricity. Yet, several issues must be solved before achieving a commercial fusion reactor. Impurity accumulation in the plasma core region is one of these issues as it may degrade fusion performances due to dilution and radiative cooling. Therefore, impurity transport has become a subject of utmost importance. Impurity concentration is determined by turbulence and neoclassical physics on long time scales, of the order of the confinement time. However, radial transport is also affected by MHD (Magneto-Hydro-Dynamic) events which occur on much faster time scales. In particular, sawtooth cycling plays a crucial role as it periodically redistributes the impurity density in the core region. Thus, the global impurity behaviour results from a complex combination of different transport processes : MHD instabilities, collisions and turbulence.

There is no code so far able to address these 3 transport processes at the same time. However, it appears that collisional and MHD transport can be described in the same framework, bound on fluid equations. Indeed, heavy impurities are in the high collisional (Pfirsch-Schlüter) regime due to high charge numbers. This allowed tackling this subject with one tool only, to address two classes of processes out of three. In addition, turbulent transport can be taken into account by adding appropriate transport coefficients. This thesis work aimed at studying heavy impurity transport in sawtoothing plasmas using non-linear tridimensional MHD simulations with the XTOR-2F code.

The basic numerical tools used in this work are the CHEASE code and the XTOR-2F code, which model the magnetic equilibrium and non-linear two-fluid MHD respectively. A set of rescaled plasma parameters is used to simulate sustained sawtooth cycles with the XTOR-2F code, since using an experimental plasma resistivity in simulations is numerically demanding. The impurity behaviour in sawtoothing bulk plasmas can now be simulated with the XTOR-2F code in an elongated cross-section, in order to compare simulations with experiments.

Features that bear similarities with compound sawteeth reported in experiments were noticed in several simulations in an elongated geometry. A detailed analysis on the simulated compound sawteeth showed that the plasma hot core is radially displaced and poloidally rotates during the partial crash. It is only partially expelled out of the $q = 1$ surface and returns

back to the center after the partial crash. This behaviour is consistent with experimental observations. The unstable internal kink mode is shown to be responsible for the displacement of the hot core. Partial crashes occur when the $q = 1$ radius exceeds a critical value, at fixed poloidal beta β_p. This critical value is shown to depend on the plasma elongation, which was the other control parameter used in this work. It has been revealed that the model used for the heat diffusivity plays an important role as it affects the temperature profile, thus the current profile via the resistivity. Also, a weaker diamagnetic stabilization during the ramp phase made the partial crash time larger than the collapse time of an ordinary sawtooth. Thus, a partial crash is shown to be the result of a competition between destabilizing effects such as the $q = 1$ radius and diamagnetic stabilization. The consistency of simulated compound sawteeth with experimental observations again confirmed the capability of the XTOR-2F code to be used as a predictive model.

The behaviour of tungsten in ASDEX-Upgrade sawtoothing plasmas was evaluated using 2-D SXR (Soft X-Ray), electron density and temperature measurements. The objective of these discharges was to study the effects of core deposition of EC (Electron Cyclotron) waves on controlling tungsten accumulation in presence of sawteeth. The observations showed that the tungsten density profile is hollow when EC waves are located near the magnetic axis and is likely associated with the internal kink mode with a lower mode frequency. The predictions by turbulent and neoclassical transport models did not reproduce the observations. The global tungsten transport is indeed a result from complex physics combining MHD, collision and turbulence. Thus, a numerical tool which models MHD instabilities and includes appropriate impurity transport model has been developed during this thesis in order to investigate and understand experimental observations.

Since tungsten is in the Pfirsch-Schlüter regime, fluid equations can be used to model its transport. Thus, the effects of sawteeth on impurity transport are studied by deriving appropriate fluid equations for impurities in the high collisionality (Pfirsch-Schlüter) regime, which have been implemented in the XTOR-2F code. The simulations without MHD instabilities reproduced the effects of the main ion density and temperature gradients which are consistent with neoclassical theory. The presence of regular sawtooth crashes is shown to flatten the impurity profile. Also, a spatial non-uniformity of 5% in post-crash impurity density profiles is obtained due to 2-D structures of impurity density which appear during sawtooth crashes. They are shown to be mainly driven by the $\mathbf{E} \times \mathbf{B}$ drift velocity, and responsible for the sudden impurity transport in the core plasmas. Finally, sawtoothing bulk plasmas with a saturated helical state are simulated with the XTOR-2F code by adding an ECCD (Electron Cyclotron Current Drive) source located inside the $q = 1$ surface. These simulations which are reminiscent of the ASDEX-Upgrade discharge scenario show that the saturated internal kink mode is responsible for tungsten depletion in the core region. Indeed, the impurity density profile remains flatter than what was expected for ordinary sawtooth cycles. However, hollow impurity density profiles as observed in the ASDEX-Upgrade discharge are not reproduced. This could be due to limitations of the closure that is being used

for reproducing neoclassical transport.

The main conclusion of this work is that the impurity behaviour in sawtoothing plasmas results from a competition of sawtooth relaxations with turbulent and neoclassical transport processes. The radial transport of impurities during sawtooth crashes is governed by the impurity density structures which are driven by MHD flows. These structures are responsible for the fluctuations of the post-crash impurity density profiles in the core region, which is not predicted by Kadomtsev's model.

Future work

Now that the appropriate fluid equations for heavy impurities are implemented in the XTOR-2F code, the effects of the saturated (1,1) mode on the impurity behaviour remain to be explored. For that purpose, sawtooth cycles with a helical equilibrium between two consecutive crashes (so-called 'humpback' sawteeth) have to be simulated. An EC wave source and its propagation model developed and implemented in the XTOR-2F code for NTM (Neoclassical Tearing Mode) controls is used for this purpose.

The effects due to toroidal rotation on tungsten redistribution have to be taken into account to complete the model. On the one hand, preliminary simulations without MHD instabilities showed that the centrifugal force weakens the temperature screening effect. This is consistent with predictions made by analytical computations. On the other hand, the poloidal asymmetry of the impurity density was completely wiped out by the violent impurity redistribution during sawtooth crashes. In addition, the complex interaction between heavy impurity radiation and the sawtooth dynamics can be addressed. For instance, the radiative cooling due to heavy impurities can be high enough to modify the bulk plasma dynamics which leads to a reduced temperature gradient and resistivity. Simulations can be compared with experimental SXR measurements using synthetic SXR diagnostic modules which have been implemented in the XTOR-2F code.

Furthermore, the XTOR-K code which is an upgrade of the XTOR-2F code models a population of particles kinetically, resulting in a mixed fluid-kinetic description. Modelling the main ion and impurity species in the kinetic framework allows one to address the impurity transport self-consistently. Indeed, the adjustment of the fluid equations to recover the Pfirsch-Schlüter transport would be avoided. Also, the transport of impurities in the banana-plateau regime can be modelled with this new tool.

APPENDIX A

Résumé long de la thèse

Les performances des plasmas de fusion confinés magnétiquement peuvent être dégradées par l'accumulation d'impuretés. Plus particulièrement, les impuretés lourdes accumulées au centre du plasma diluent les réactifs, et peuvent aussi conduire à un collapse radiatif du plasma lorsque les pertes par rayonnement sont élevées. La compréhension du transport des impuretés lourdes produites lors de l'interaction plasma-paroi est donc cruciale.

Le coeur du plasma est sujet à une instabilité magnétohydrodynamique (MHD) appelée "kink interne" caractérisée par des nombres de mode poloïdal et toroïdal $(m, n) = (1, 1)$. Cette instabilité conduit à des oscillations de relaxation nommées "dents-de-scie". Les dents-de-scie entraînent une relaxation périodique de densité et de température dans le coeur du plasma. Un cycle de dents-de-scie est consitué principalement de deux phases : une phase de rampe et une phase de collapse. Pendant une durée du crash, de l'ordre de $100\mu s$, qui est très courte par rapport au temps de confinement, les particules et la chaleur sont redistribuées et le transport radial est significativement affecté. Dans cette thèse, l'outil numérique utilisé pour simuler les dents-de-scie est le code XTOR-2F. XTOR-2F est un code non-linéaire tridimensionnel résolvant les équations de la MHD bi-fluide dans une géométrie toroïdale.

Afin de préparer la modélisation des décharges expérimentales, une étude paramétrique a été conduite afin de simuler des dents-de-scie avec le code XTOR-2F, dans une géométrie allongée. Il s'avère que certaines simulations présentent des caractéristiques similaires aux observations expérimentales des dents-de-scie composées. En effet, dans des cas particuliers, les simulations avec le code XTOR-2F montrent que le coeur chaud du plasma est déplacé dans la direction radiale et tourne dans le sens poloidal, tout en restant à l'intérieur de la surface résonante $q = 1$. Ce phénomène, nommé 'crash partiel', correspond aux observations expérimentales. Le balayage en position de la surface $q = 1$ montre que le crash partiel apparaît lorsque ce paramètre se trouve au-delà d'une valeur critique. Cette valeur critique dépend de l'élongation du plasma, qui est un autre paramètre de contrôle utilisé pour cette étude. Il s'avère que la durée du crash partiel est plus longue que celle d'un crash ordinaire, ce qui est probablement dû à une stabilisation diamagnétique. Ceci suggère que le crash partiel résulte d'une compétition entre effets déstabilisants, par exemple la position de la surface q=1, et la stabilisation diamagnétique.

Dans cette thèse, on se réfèrera aux observations expérimentales du tokamak ASDEX-Upgrade, dont l'interprétation a motivé une modélisation numérique avec le code XTOR-2F. Ces décharges sont destinées aux études du transport du tungstène en présence des dents-

de-scie et son contrôle en injectant dans la région centrale des ondes dont la fréquence correspond à la fréquence cyclotronique électronique. Le diagnostic X-mou est l'outil principal qui permet de suivre l'évolution des impuretés lourdes dans le coeur du plasma. Des mesures expérimentales montrent que la dynamique des impuretés en présence des dents de scie est différente des prédictions faites par les codes de transport qui ne tiennent pas compte de la MHD. En effet, le comportement des impuretés résulte d'une combinaison complexe des différents processus de transport. Il est alors nécessaire d'avoir un outil numérique capable de modéliser les instabilités MHD en ayant un modèle approprié du transport d'impuretés, afin de poursuivre et compléter les études expérimentales.

En l'absence d'instabilités MHD, le transport des impuretés est porté par les collisions (transport néoclassique) et la turbulence. Il est établi que le transport néoclassique est important pour les impuretés lourdes dans la région centrale du plasma de tokamak. Les équations fluides modélisant le transport des impuretés dans un régime de collisionalité élevée (Pfirsch-Schlüter) ont été implémentées et couplées à l'ensemble des équations de la MHD bi-fluide. Le couplage des équations a conduit à une amélioration de la matrice du préconditionnement, ce qui est un progrès apporté dans le code XTOR-2F en terme numérique. Dans les simulations, les impuretés sont considérés comme des traceurs afin de négliger les rétroactions sur le plasma de fond. Les résultats des simulations sans instabilités MHD sont cohérents avec le transport radial prédit par la théorie néoclassique. Les simulations avec des dents-de-scie montrent que la présence des relaxations peŕiodiques affectent significativement le transport des impuretés, en accord avec les observations expérimentales. Ceci résulte d'une compétition entre processus néoclassiques et relaxations dues aux dents de scie. Premièrement, l'effet favorable d'écrantage thermique est affaibli par rapport au cas sans dents-de-scie. Deuxièmement, une fluctuation de 5% apparaît dans les profils de densité d'impuretés après un crash dents-de-scie. Elle est due aux structures de densité d'impuretés qui apparaissent pendant la phase du crash. Il est montré que ces structures sont principalement convectées par la vitesse $\mathbf{E} \times \mathbf{B}$. Enfin, un état hélicoïdal saturé, qui se rapproche des scénarios expérimentaux, est simulé avec le code XTOR-2F en ajoutant une source de courant. Il s'avère qu'une durée prolongée des oscillations du précurseur fait que les profils de densité d'impuretés restent plus plats que ceux prédits pour les cycles de dents-de-scie ordinaires.

Bibliography

Ahn J.-H., Garbet X., Lütjens H., Marx A., Nicolas T. *et al.* (**2016a**), *Non-linear dynamics of compound sawteeth in tokamaks.* Physics of Plasmas, *23*, 052509.

Ahn J.-H., Garbet X., Lütjens H. and Guirlet R. (**2016b**), *Dynamics of heavy impurities in non-linear MHD simulations of sawtoothing tokamak plasmas.* Plasma Physics and Controlled Fusion, *58*, 125009.

Angioni C., Goodman T. P., Henderson M. A. and Sauter O. (**2003**), *Effects of localized electron heating and current drive on the sawtooth period.* Nuclear Fusion, *43*, pp.455–468.

Angioni C. and Peeters A. G. (**2006**), *Direction of impurity pinch and auxiliary heating in tokamak plasmas.* Physical Review Letters, *96*, 095003.

Angioni C., Mantica P., Pütterich T., Valisa M., Baruzzo M. *et al.* (**2014**), *Tungsten transport in JET H-mode plasmas in hybrid scenario, experimental observations and modelling.* Nuclear Fusion, *54*, 083028.

Angioni C. and Helander P. (**2014**), *Neoclassical transport of heavy impurities with poloidally asymmetric density distribution in tokamaks.* Plasma Physics and Controlled Fusion, *56*, 124001.

Anton M., Weisen H., Dutch M. J., von der Linden W., Buhlmann F. *et al.* (**1996**), *X-ray tomography on the TCV tokamak.* Plasma Physics and Controlled Fusion, *38*, pp. 1849–1878.

Ara G., Basu B., Coppi B., Laval G., Rosenbluth M. *et al.* (**1978**), *Magnetic reconnection and $m = 1$ oscillations in current carrying plasmas.* Annals of Physics, *112*, pp.443–476.

Aydemir A. Y., Wiley J. C. and Ross D. W. (**1989**), *Toroidal studies of sawtooth oscillations in tokamaks.* Physics of Fluids B, *1*, pp.774–787.

Aydemir A. Y. (**1992**), *Nonlinear studies of $m = 1$ modes in high temperature plasmas.* Physics of Fluids B, *4*, pp.3469–3472.

Aydemir A. Y., Kim J. Y., Park B. H. and Seol J. (**2015**), *On resistive magnetohydrodynamic studies of sawtooth oscillations in tokamaks.* Physics of Plasmas, *22*, 032304.

Belli E. A. and Candy J. (**2012**), *Full linearized Fokker-Planck collisions in neoclassical transport simulations.* Plasma Physics and Controlled Fusion, *54*, 015015.

Belli E. A., Candy J. and Angioni C. (**2014**), *Pfirsch–Schlüter neoclassical heavy impurity transport in a rotating plasma.* Plasma Physics and Controlled Fusion, *56*, 124002.

Belmont G., Grappin R., Mottez F., Pantellini F. and Pelletier G. (**2013**), *Collisionless Plasmas in Astrophysics.* Wiley.

Bhatnagar V. P., Taroni A., Ellis J. J., Jacquinot J. and Start D. F. H. (**1989**), *ICRF power-deposition profiles, heating and confinement of monster sawtooth and peaked-density profile discharges in JET.* Plasma Physics and Controlled Fusion, *31*, pp.2111–2126.

Bierwage A., Yun G. S., Choe G. H., Nam Y., Lee W. *et al.* (**2015**), *Dynamics of multiple flux tubes in sawtoothing KSTAR plasmas heated by electron cyclotron waves : II. Theoretical and numerical analysis.* Nuclear Fusion, *55*, 013016.

Bilato R., Maj O. and Angioni C. (**2014**), *Modelling the influence of temperature anisotropies on poloidal asymmetries of density in the core of rotating plasmas.* Nuclear Fusion, *54*, 072003.

Biskamp D. and Drake J. F. (**1994**), *Dynamics of the sawtooth collapse in tokamak plasmas.* Physical Review Letters, *73*, pp.971–974.

Biskamp D. and Sato T. (**1997**), *Partial reconnection in the nonlinear internal kink mode.* Physics of Plasmas, *4*, pp.1326–1329.

Biskamp D. (**2005**), *Magnetic reconnection in plasmas.* Cambridge University Press.

Boileau A., von Hellermann M., Horton L. D., Spence J. and Summers H. P. (**1989**), *The deduction of low-Z ion temperature and densities in the JET tokamak using charge exchange recombination spectroscopy.* Plasma Physics and Controlled Fusion, *31*, pp. 779–804.

Braginskii S. I. (**1965**), *Transport processes in plasma.* In Review of Plasma Physics, *1*, pp.201–311. Consultants Bureau.

Brennan D. P., Kruger S. E., Gianakon T. A. and Schnack D. D. (**2005**), *A categorization of tearing mode onset in tokamaks via nonlinear simulation.* Nuclear Fusion, *45*, pp. 1178–1190.

Bussac M. N., Pellat R., Edery D. and Soule J. L. (**1975**), *Internal kink modes in toroidal plasmas with circular cross sections.* Physical Review Letters, *35*, pp.1638–1641.

Buttery R. J., Hender T. C., Howell D. F., La Haye R. J., Parris S. *et al.* (**2004**), *On the form of NTM onset scalings.* Nuclear Fusion, *44*, pp.678–685.

Camacho J. F. and Granetz R. S. (**1986**), *Soft X-ray tomography diagnostic of the Alcator C tokamak*. Review of Scientific Instruments, *57*, pp.417–425.

Campbell D. J., Gill R. D., Gowers C. W., Wesson J. A., Bartlett D. V. *et al.* (**1986**), *Sawtooth activity in ohmically heated JET plasmas*. Nuclear Fusion, *26*, pp.1085–1092.

Carraro L., Gabellieri L., Mattioli M., Finkenthal M., Fournier K. *et al.* (**2004**), *Study of impurity transport in FTU ITB plasmas*. Plasma Physics and Controlled Fusion, *46*, pp. 389–407.

Casson F. J., Peeters A. G., Angioni C., Camenen Y., Hornsby W. A. *et al.* (**2010**), *Gyrokinetic simulations including the centrifugal force in a rotating tokamak plasma*. Physics of Plasmas, *17*, 102305.

Casson F. J., Angioni C., Belli E. A., Bilato R., Mantica P. *et al.* (**2015**), *Theoretical description of heavy impurity transport and its application to the modelling of tungsten in JET and ASDEX Upgrade*. Plasma Physics and Controlled Fusion, *57*, 014031.

Catto P. J., Bernstein I. B. and Tessarotto M. (**1987**), *Ion transport in toroidally rotating tokamak plasmas*. Physics of Fluids, *30*, pp.2784–2795.

Chapman I. T., Buttery R. J., Coda S., Gerhardt S., Graves J. P. *et al.* (**2010**), *Empirical scaling of sawtooth period for onset of neoclassical tearing modes*. Nuclear Fusion, *50*, 102001.

Chapman I. T. (**2011**), *Controlling sawtooth oscillations in tokamak plasmas*. Plasma Physics and Controlled Fusion, *53*, 013001.

Chapman I. T., Graves J. P., Johnson T., Asunta O., Bonoli P. *et al.* (**2011**), *Sawtooth control in ITER using ion cyclotron resonance heating*. Plasma Physics and Controlled Fusion, *53*, 124003.

Chapman I. T., La Haye R. J., Buttery R. J., Heidbrink W. W., Jackson G. L. *et al.* (**2012**), *Sawtooth control using electron cyclotron current drive in ITER demonstration plasmas in DIII-D*. Nuclear Fusion, *52*, 063006.

Chapman I. T., Graves J. P., Sauter O., Zucca C., Asunta O. *et al.* (**2013**), *Power requirements for electron cyclotron current drive and ion cyclotron resonance heating for sawtooth control in ITER*. Nuclear Fusion, *53*, 066001.

Coppi A. C. and Coppi B. (**1992**), *Stability of global modes in advanced plasma confinement configurations*. Nuclear Fusion, *32*, pp.205–216.

Cormack A. M. (**1964**), *Representation of a function by its line integrals, with some radiological applications II*. Journal of Applied Physics, *35*, pp.2908–2914.

Cowley S. C. (**2016**), *The quest for fusion power.* Nature Physics, *12*, pp.384–386.

de Blank H. J. and Schep T. J. (**1991**), *Theory of the $m = 1$ kink mode in toroidal plasma.* Physics of Fluids B, *3*, pp.1136–1151.

de Michelis C. and Mattioli M. (**1981**), *Soft X-rays spectroscopic diagnostics of laboratory plasmas.* Nuclear Fusion, *53*, pp.677–754.

Denton R. E., Drake J. F., Kleva R. G. and Boyd D. A. (**1986**), *Skin currents and compound sawteeth in tokamaks.* Physical Review Letters, *56*, pp.2477–2480.

Dux R., Peeters A. G., Gude A., Kallenbach A., Neu R. *et al.* (**1999**), *Z dependence of the core impurity transport in ASDEX-Upgrade H mode discharges.* Nuclear Fusion, *39*, pp. 1509–1522.

Dux R., Neu R., Peeters A. G., Pereverzev G., Mück A. *et al.* (**2003**), *Influence of the heating profile on impurity transport in ASDEX Upgrade.* Plasma Physics and Controlled Fusion, *45*, pp.1815–1825.

Edwards A. W., Campbell D. J., Engelhardt W. W., Farhbach H.-U., Gill R. D. *et al.* (**1986**), *Rapid collapse of a plasma sawtooth oscillation in the JET tokamak.* Physical Review Letters, *57*, pp.210–213.

Estève D. (**2015**), *Etude gyrocinétique du transport multi-espèces néoclassique et turbulent dans un plasma de fusion.* PhD dissertation, Université Aix-Marseille.

Estève D., Garbet X., Sarazin Y., Grandgirard V., Cartier-Michaud T. *et al.* (**2015**), *A multi-species collisional operator for full-F gyrokinetics.* Physics of Plasmas, *22*, 122506.

Felici F., Goodman T., Sauter O., Canal G., Coda S. *et al.* (**2012**), *Integrated real-time control of MHD instabilities using multi-beam ECRH/ECCD systems on TCV.* Nuclear Fusion, *52*, 074001.

Février O., Maget P., Lütjens H., Luciani J.-F., Decker J. *et al.* (**2016**), *First principles fluid modelling of magnetic island stabilization by electron cyclotron current drive (ECCD).* Plasma Physics and Controlled Fusion, *58*, 045015.

Février O. (**2016**), *Global modelling of magnetic island control in tokamaks.* PhD dissertation, Université Aix-Marseille.

Février O., Ahn J.-H., Maget P., Garbet X., Nicolas T. *et al.* (**2017**), *MHD simulations of sawteeth response to ECCD deposition.* in preparation.

Fülöp T. and Helander P. (**1999**), *Nonlinear neoclassical transport in a rotating impure plasma with large gradients.* Physics of Plasmas, *6*, pp.3066–3075.

Furno I., Angioni C., Porcelli F., Weisen H., Behn R. *et al.* (**2001**), *Understanding sawtooth activity during intense electron cyclotron heating experiments on TCV.* Nuclear Fusion, *41*, pp.403–420.

Gantenbein G., Zohm H., Giruzzi G., Günter S., Leuterer F. *et al.* (**2000**), *Complete suppression of neoclassical tearing modes with current drive at the electron-cyclotron-resonance frequency in ASDEX Upgrade tokamak.* Physical Review Letters, *85*, pp.1242–1245.

Garcìa-Regaña J. M., Kleiber R., Beidler C. D., Turkin Y., Maaßberg H. *et al.* (**2013**), *On neoclassical impurity transport in stellarator geometry.* Plasma Physics and Controlled Fusion, *55*, 074008.

Granetz R. S. and Smeulders P. (**1988**), *X-ray tomography on JET.* Nuclear Fusion, *28*, pp.457–476.

Graves J. P. (**2005**), *Internal kink mode stabilization and the properties of auxiliary heated ions.* Physics of Plasmas, *12*, 090908.

Graves J. P., Chapman I. T., Coda S., Lennholm M., Albergante M. *et al.* (**2011**), *Control of magnetohydrodynamic stability by phase space engineering of energetic ions in tokamak plasmas.* Nature Communications, *3*, 624.

Guirlet R., Sirinelli A., Parisot T., Sabot R., Artaud J. F. *et al.* (**2010**), *Particle transport in low core turbulence Tore-Supra plasmas.* Nuclear Fusion, *50*, 095009.

Halpern F. D., Leblond D., Lütjens H. and Luciani J.-F. (**2011a**), *Oscillation regimes of the internal kink mode in tokamak plasmas.* Plasma Physics and Controlled Fusion, *53*, 015011.

Halpern F. D., Lütjens H. and Luciani J.-F. (**2011b**), *Diamagnetic thresholds for sawtooth cycling in tokamak plasmas.* Physics of Plasmas, *18*, 102501.

Hansen P. C. (**2001**), *The L-curve and its use in the numerical treatment of inverse problems.* In Computational inverse problems in electrocardiology. WIT Press.

Hastie R. J., Hender T. C., Carreras B. A., Charlton L. A. and Holmes J. A. (**1987**), *Stability of ideal and resistive internal kink modes in toroidal geometry.* Physics of Fluids, *30*, pp.1756–1766.

Hastie R. J. and Hender T. C. (**1988**), *Toroidal internal kink stability in tokamaks with ultra flat q profiles.* Nuclear Fusion, *28*, pp.585–594.

Hastie R. J. (**1998**), *Sawtooth instability in tokamak plasmas.* Astrophysics and Space Science, *256*, pp.177–204.

Hazeltine R. D. and Meiss J. D. (**2003**), *Plasma Confinement*. Dover Publications.

Helander P. and Sigmar D. J. (**2005**), *Collisional transport in magnetized plasmas*. Cambridge University Press.

Hender T. C., Wesley J. C., Bialek J., Bondeson A., Boozer A. H. *et al.* (**2007**), *Chapter 3: MHD stability, operational limits and disruptions*. Nuclear Fusion, *47*, pp.S128–S202.

Hender T. C., Buratti P., Casson F. J., Alper B., Baranov Y. F. *et al.* (**2016**), *The role of MHD in causing impurity peaking in JET hybrid plasmas*. Nuclear Fusion, *56*, 066002.

Hinton F. L. and Hazeltine R. D. (**1976**), *Theory of plasma transport in toroidal confinement systems*. Reviews of Modern Physics, *48*, pp.239–308.

Hinton F. L. (**1983**), *Collisional transport in plasma*. In Handbook of Plasma Physics, *1*, pp.148–197. Norh-Holland Publishing Company.

Hinton F. L. and Wong S. K. (**1985**), *Neoclassical ion transport in rotating axisymmetric plasmas*. Physics of Fluids, *28*, pp.3082–3098.

Hirshman S. P. and Sigmar D. J. (**1981**), *Neoclassical transport of impurities in tokamak plasmas*. Nuclear Fusion, *21*, pp.1079–1201.

Huba J. D. (**2011**), *NRL plasma Formulary*. Naval Research Laboratory.

Huber A., McCormick K., Andrew P., Beaumont P., Dalley S. *et al.* (**2007**), *Upgraded bolometer system on JET for improved radiation measurements*. Fusion Engineering and Design, *82*, pp.1327–1334.

Hutchinson I. H. (**1987**), *Principles of plasma diagnostics*. Cambridge University Press.

Ingesson L. C. (**1995**), *Visible-light tomography of tokamak plasmas*. PhD dissertation, Technische Universiteit Eindhoven.

Ingesson L. C., Alper B., Chen H., Edwards A. W., Fehmers G. C. *et al.* (**1998**), *Soft X ray tomography during ELMs and impurity injection in JET*. Nuclear Fusion, *38*, pp. 1675–1694.

Ingesson L. C., Böcker P. J., Reichle R., Romanelli M. and Smeulders P. (**1999**), *Projection-space methods to take into account finite beam-width effects in two-dimensional tomography algorithms*. Journal of the Optical Society of America A, *16*, pp.17–27.

Ingesson L. C., Alper B., Peterson B. J. and Vallet J.-C. (**2008**), *Tomography diagnostics: bolometry and Soft X-Ray detection*. Fusion Science and Technology, *53*, pp.528–576.

ITER Physics Expert Group on Disruptions, Plasma Control, and MHD and ITER Physics Basis Editors. (**1999**), *Chapter 3: MHD stability, operational limits and disruptions*. Nuclear Fusion, *39*, pp.2251–2389.

Janicki C., Simm C., Décoste R., Pacher G. W. and Pacher H. D. (**1990**), *Tomographic analysis of counpound sawteeth on the Tokamak de Varennes*. Nuclear Fusion, *30*, pp. 950–955.

Kadomtsev B. B. (**1975**), *On disruptive instability in tokamaks*. Soviet Journal of Plasma Physics, *1*, pp.389–391. [Fizika Plazmy, *1*, pp.710−715].

Kaufmann M. and Neu R. (**2007**), *Tungsten as first wall material in fusion devices*. Fusion Engineering and Design, *82*, pp.521–527.

Kim D., Goodman T. P. and Sauter O. (**2014**), *Real-time sawtooth control and neoclassical tearing mode preemption in ITER*. Physics of Plasmas, *21*, 061503.

Krasheninnikov S. I., Zakharov L. E. and Pereverzev G. V. (**2003**), *On lithium walls and the performance of magnetic fusion devices*. Physics of Plasmas, *10*, pp.1678–1682.

Kugel H. W., Bell M. G., Ahn J.-W., Allain J. P., Bell R. *et al.* (**2008**), *The effect of lithium surface coatings on plasma performance in the National Spherical Torus Experiment*. Physics of Plasmas, *15*, 056118.

Lawson J. D. (**1957**), *Some criteria for a power producing thermonuclear reactor*. In Proceedings of the Physical Society Section B, pp.6–10.

Leigheb M., Romanelli M., Gabellieri L., Carraro L., Mattioli M. *et al.* (**2007**), *Molybdenum transport in high density FTU plasmas with strong radio frequency electron heating*. Plasma Physics and Controlled Fusion, *49*, pp.1897–1912.

Lennholm M., Eriksson L.-G., Turco F., Bouquey F., Darbos C. *et al.* (**2009**), *Demonstration of effective control of fast-ion-stabilized sawteeth by electron-cyclotron current drive*. Physical Review Letters, *102*, 115004.

Luce T. C. (**2013**), *An analytic functional form for characterization and generation of axisymmetric plasma boundaries*. Plasma Physics and Controlled Fusion, *55*, 095009.

Lütjens H., Bondeson A. and Vlad G. (**1992**), *Ideal MHD stability of internal kinks in circular and shaped tokamaks*. Nuclear Fusion, *32*, pp.1625–1636.

Lütjens H., Bondeson A. and Sauter O. (**1996**), *The CHEASE code for toroidal MHD equilibria*. Computer Physics Communications, *97*, pp.219–260.

Lütjens H. and Luciani J.-F. (**1997**), *Stability thresholds for ballooning modes driven by high β internal kinks*. Physics of Plasmas, *4*, pp.4192–4194.

Lütjens H. and Luciani J.-F. (**2005**), *Saturation levels of neoclassical tearing modes in International Thermonuclear Experimental Reactor plasmas.* Physics of Plasmas, *12*, 080703.

Lütjens H., Luciani J.-F., Leblond D., Halpern F. and Maget P. (**2009**), *Non-linear modeling of core MHD in tokamaks.* Plasma Physics and Controlled Fusion, *51*, 124038.

Lütjens H. and Luciani J.-F. (**2010**), *XTOR-2F: A fully implicit Newton-Krylov solver applied to nonlinear 3D extended MHD in tokamaks.* Journal of Computational Physics, *229*, pp.8130–8143.

Maget P., Artaud J.-F., Eriksson L.-G., Huysmans G., Lazaros A. *et al.* (**2005**), *MHD activity triggered by monster sawtooth crashes on Tore Supra.* Plasma Physics and Controlled Fusion, *47*, pp.357–377.

Maget P., Lütjens H., Luciani J.-F., Garbet X., Février O. *et al.* (**2014**), *Bi-fluid and neoclassical effect on a Double-Tearing mode in Tore Supra.* Physics of Plasmas, *21*, 062504.

Marinoni A., Brunner S., Camenen Y., Coda S., Graves J. P. *et al.* (**2009**), *The effect of plasma triangularity on turbulent transport: modeling TCV experiments by linear and non-linear gyrokinetic simulations.* Plasma Physics and Controlled Fusion, *51*, 055016.

Martynov A., Graves J. P. and Sauter O. (**2005**), *The stability of the ideal internal kink mode in realistic tokamak geometry.* Plasma Physics and Controlled Fusion, *47*, pp. 1743–1762.

Mattioli M., de Michelis C. and Pecquet A. L. (**1998**), *Laser blow-off injected impurity transport in L mode Tore Supra plamsas.* Nuclear Fusion, *38*, pp.1629–1635.

Mazon D., Vezinet D., Pacella D., Moreau D., Gabelieri L. *et al.* (**2012**), *Soft X-ray tomography for real-time applications : present status at Tore Supra and possible future developments.* Review of Scientific Instruments, *83*, 063505.

McCarthy P. J., Martin P. and Schneider W. (**1999**), *The CLISTE interpretive equilibrium code.* Rep.5/85, Max-Plank-Institut für Plasmaphysik, Garching.

Mück A., Goodman T. P., Maraschek M., Pereverzev G., Ryter F. *et al.* (**2005**), *Sawtooth control experiments on ASDEX Upgrade.* Plasma Physics and Controlled Fusion, *47*, pp. 1633–1655.

Nagayama Y., McGuire K. M., Bitter M., Cavallo A., Fredrickson E. D. *et al.* (**1991**), *Analysis of sawtooth oscillations using simultaneous measurement of electron cyclotron emission imaging and X-ray tomography on TFTR.* Physical Review Letters, *67*, pp. 3527–3530.

Nagayama Y., Taylor G., Yamada M., Fredrickson E. D., Janos A. C. *et al.* (**1996**), *ECE image reconstruction of partial sawtooth crashes in ohmic plasmas.* Nuclear Fusion, *36*, pp.521–526.

Nicolas T., Sabot R., Garbet X., Lütjens H., Luciani J.-F. *et al.* (**2012**), *Non-linear magnetohydrodynamic simulations of density evolution in Tore Supra sawtoothing plasmas.* Physics of Plasmas, *19*, 112305.

Nicolas T. (**2013**), *Sawtooth driven particle transport on tokamak plasmas.* PhD dissertation, Ecole Polytechnique.

Nicolas T., Lütjens H., Luciani J.-F., Garbet X. and Sabot R. (**2014**), *Impurity behavior during sawtooth activity in tokamak plasmas.* Physics of Plasmas, *21*, 012507.

Noda N., Philips V. and Neu R. (**1997**), *A review of recent experiments on W and high Z materials as plasma-facing components in magnetic fusion devices.* Journal of Nuclear Materials, *241-243*, pp.227–243.

Ödblom A., Anderson D., Eriksson L.-G. and Lisak M. (**1996**), *Sawteeth-induced impurity transport in tokamak plasmas.* Physics of Plasmas, *3*, pp.956–964.

Odstrcil M., Mlynar J., Odstrcil T., Alper B. and Murari A. (**2012**), *Modern numerical methods for plasma tomography optimisation.* Nuclear Instruments and Methods in Physics Research Section A, *686*, pp.156–161.

Odstrcil T., Pütterich T., Weiland M., Odstrcil M., Gude A. *et al.* (**2015**), *SXR tomography of tungsten radiation patterns with and without MHD.* In 42nd EPS Conference on Plasma Physics, P1.133.

Odstrcil T. private communication.

Ongena J., Monier-Garbet P., Suttrop W., Andrew P., Bécoulet M. *et al.* (**2004**), *Towards the realization on JET of an integrated H-mode scenario for ITER.* Nuclear Fusion, *44*, pp.124–133.

Ongena J., Koch R., Wolf R. and Zohm H. (**2016**), *Magnetic-confinement fusion.* Nature Physics, *12*, pp.398–410.

Parail V. V. and Pereverzev G. V. (**1980**), *Internal disruption in a tokamak.* Soviet Journal of Plasma Physics, *6*, pp.14–17. [Fizika Plazmy, *6*, pp.27−33].

Parker E. N. (**1957**), *Sweet's mechanism for merging magnetic fields in conducting fluids.* Jounal of Geophysical Research, *62*, pp.509–520.

Pfeiffer W. (**1985**), *Double-sawtooth oscillations in the Doublet III tokamak.* Nuclear Fusion, *25*, pp.673–679.

Pietrzyk Z., Pochelon A., Goodman T. P., Henderson M. A., Hogge J.-P. *et al.* (**1999**), *Behaviour of central plasma relaxation oscillations during localized electron cyclotron heating on the TCV tokamak*. Nuclear Fusion, *39*, pp.587–611.

Pitts R. A., Carpentier S., Escourbiac F., Hirai T., Komarov V. *et al.* (**2011**), *Physics basis and design of the ITER plasma-facing components*. Journal of Nuclear Materials, *415*, pp.S957–S964.

Popov A. M. (**2006**), *Nonlinear 3D MHD code NFTC for simulations of plasma instabilities*. Journal of Plasma Physics, *72*, pp.1101–1104.

Porcelli F., Boucher D. and Rosenbluth M. N. (**1996**), *Model for the sawtooth period and amplitude*. Plasma Physics and Controlled Fusion, *38*, pp.2163–2186.

Puiatti M. E., Valisa M., Angioni C., Garzotti L., Mantica P. *et al.* (**2006**), *Analysis of metallic impurity density profiles in low collisionality Joint European Torus H-mode and L-mode plasmas*. Physics of Plasmas, *13*, 042501.

Pütterich T., Neu R., Dux R., Whiteford A. D., O'Mullane M. *et al.* (**2010**), *Calculation and experimental test of the cooling factor of tungsten*. Nuclear Fusion, *50*, 025012.

Reinke M. L., Hutchinson I. H., Rice J. E., Howard N. T., Bader A. *et al.* (**2012**), *Poloidal variation of high-Z impurity density due to hydrogen minority ion cyclotron resonance heating on Alcator C-Mod*. Plasma Physics and Controlled Fusion, *54*, 045004.

Rice J. E., Bonoli P. T., Marmar E. S., Wukitch S. J., Boivin R. L. *et al.* (**2002**), *Double transport barrier plasmas in Alcator C-Mod*. Nuclear Fusion, *42*, pp.510–519.

Rogers B. and Zakharov L. (**1995**), *Nonlinear ω^*-stabilization of the $m = 1$ mode in tokamaks*. Physics of Plasmas, *2*, pp.3420–3428.

Romanelli M. and Ottaviani M. (**1998**), *Effects of density asymmetries on heavy impurity transport in a rotating tokamak plasma*. Plasma Physics and Controlled Fusion, *40*, pp. 1767–1773.

Rosenberg A. L., Gates D. A., Pletzer A., Menard J. E., Kruger S. E. *et al.* (**2002**), *Modeling of neoclassical tearing mode stability for generalized toroidal geometry*. Physics of Plasmas, *9*, pp.4567–4572.

Rosenbluth M. N., Dagazian R. Y. and Rutherford P. H. (**1973**), *Nonlinear properties of the internal $m = 1$ kink instability in the cylindrical tokamak*. Physics of Fluids, *16*, pp. 1984–1902.

Rutherford P. H. (**1974**), *Effects of density asymmetries on heavy impurity transport in a rotating tokamak plasma*. The Physics of Fluids, *17*, pp.1782–1784.

Sabot R., Sirinelli A., Chareau J.-M. and Giaccalone J.-C. (**2006**), *A dual source D-band reflectometer for density profile and fluctuations measurements in Tore Supra.* Nuclear Fusion, *46*, pp.S685–S692.

Sauter O., Westerhof E., Mayoral M. L., Alper B., Belo P. A. *et al.* (**2002a**), *Control of neoclassical tearing modes by sawtooth control.* Physical Review Letters, *88*, 105001.

Sauter O., Buttery R. J., Felton R., Hender T. C., Howell D. F. *et al.* (**2002b**), *Marginal β-limit for neoclassical tearing modes in JET H-mode discharges.* Plasma Physics and Controlled Fusion, *44*, pp.1999–2019.

Sauter O., Henderson M. A., Ramponi G., Zohm H. and Zucca C. (**2010**), *On the requirements to control neoclassical tearing modes in burning plasmas.* Plasma Physics and Controlled Fusion, *52*, 025002.

Scavino E., Bakos J. S., Dux R., Weisen H. and TCV Team. (**2003**), *Effects of plasma shape on laser blow-off injected impurity transport in TCV.* Plasma Physics and Controlled Fusion, *45*, pp.1961–1974.

Sertoli M., Horváth L., Pokol G. I., Igochine V., Barrera L. *et al.* (**2013**), *Characterization of saturated MHD instabilities through 2D electron temperature profile reconstruction from 1D ECE measurements.* Nuclear Fusion, *53*, 053015.

Sertoli M., Dux R., Pütterich T. and the ASDEX-Upgrade Team. (**2015a**), *Modification of impurity transport in the presence of saturated $(m, n) = (1, 1)$ MHD activity at ASDEX Upgrade.* Plasma Physics and Controlled Fusion, *57*, 075004.

Sertoli M., Odstrcil T., Angioni C. and the ASDEX-Upgrade Team. (**2015b**), *Interplay between central ECRH and saturated $(m, n) = (1, 1)$ MHD activity in mitigating tungsten accumulation at ASDEX-Upgrade.* Nuclear Fusion, *55*, 113029.

Sertoli M. MST-1 Task Force meeting (25 May 2016).

Sertoli M. private communication.

Strachan J. D., Budny R., Coffey I., Dumortier P., Grisolia C. *et al.* (**2000**), *JET radiative mantle experiments in ELMy H-Mode.* Plasma Physics and Controlled Fusion, *42*, pp. A81–A88.

Sugai H. (**1982**), *Radio frequency control of impurity transport.* Physics Letters, *91A*, pp. 73–76.

Sugiyama L. E. (**2014**), *Compressible magnetohydrodynamic sawtooth crash.* Physics of Plasmas, *21*, 022510.

Sweet P. A. (**1958**), *The neutral point theory of solar flares.* In Proceedings of the IAU Symposium no.6 on Electromagnetic Phenomena in Cosmical Physics, pp.123–134.

Taylor G., Efthimion P. C., Arunasalam V., Goldston R. J., Grek B. *et al.* (**1986**), *Evolution of the electron temperature profile of ohmically heated plasmas in TFTR.* Nuclear Fusion, *26*, pp.339–348.

Tikhonov A. N. (**1963**), *Solution of incorrectly formulated problems and the regularization method.* Soviet Mathematics Doklady, *4*, pp.1035–1038. [Doklady Akademii Nauk SSSR, *151*, pp.501−504].

Troyon F., Gruber R., Sauremann H., Semenzato S. and Succi S. (**1984**), *MHD-limits to plasma confinement.* Plasma Physics and Controlled Fusion, *26*, pp.209–215.

Turnbull A. D. and Troyon F. (**1989**), *Toroidal effects on current driven modes in tokamaks.* Nuclear Fusion, *29*, pp.1887–1898.

Twomey S. (**1963**), *On the numerical solution of fredholm integral equations of the first kind by the inversion of the linear system produced by quadrature.* Journal of the ACM, *10*, pp.97–101.

Udintsev V. S., Ottaviani M., Maget P., Giruzzi G., Ségui J.-L. *et al.* (**2005**), *Experimental observation of $m/n = 1/1$ mode behaviour during sawtooth activity and its manifestations in tokamak plasmas.* Plasma Physics and Controlled Fusion, *47*, pp.1111–1136.

Vezinet D. (**2013**), *Soft X-ray measurements and analysis on tokamaks in view of real-time control.* PhD dissertation, Université Aix-Marseille.

Vezinet D., Mazon D., Guirlet R., Decker J. and Peysson Y. (**2014**), *Impurity density derivation from bandpass soft X-ray tomography: applicability, perspectives and limitations.* Nuclear Fusion, *54*, 083011.

von Goeler S., Stodiek W. and Sauthoff N. (**1974**), *Studies of internal disruptions and $m = 1$ oscillations in tokamak discharges with soft X-ray techniques.* Physical Review Letters, *33*, pp.1201–1203.

Waelbroeck F. L. (**1989**), *Current sheets and nonlinear growth of the $m = 1$ kink-tearing mode.* Physics of Fluids B, *1*, pp.2372–2380.

Wang X. and Bhattacharjee A. (**1993**), *Nonlinear dynamics of the $m = 1$ instability and fast sawtooth collapse in high-temperature plasmas.* Physical Review Letters, *70*, pp. 1627–1630.

Wenzel K. W. and Sigmar D. J. (**1990**), *Neoclassical analysis of impurity transport following transition to improved particle confinement.* Nuclear Fusion, *30*, pp.1117–1127.

Wesson J. A. (**1990**), *Sawtooth reconnection*. Nuclear Fusion, *30*, pp.2545–2549.

Wesson J. A., Alper B., Edwards A. W. and Gill R. D. (**1997**), *Transport in the sawtooth collapse*. Physical Review Letters, *79*, pp.5018–5021.

Wesson J. A. (**2011**), *Tokamaks*. Oxford University Press.

Xu L.-Q., Hu L.-Q., Chen K.-Y. and Li M.-H. (**2014**), *Compound sawtooth in EAST LHCD plasma: An experimental study*. Chinese Physics B, *23*, 085201.

Yamada I., Yamazaki K., Oishi T., Arimoto H. and Shoji T. (**2010**), *Transport analysis of high-Z impurities including sawtooth effects in a tokamak system*. Plasma and Fusion Research, *5*, S1022.

Yamada M., Levinton F. M., Pomphrey N., Budny R., Manickam J. *et al.* (**1994**), *Investigation of magnetic reconnection during a sawtooth crash in a high-temperature tokamak plasma*. Physics of Plasmas, *1*, pp.3269–3276.

Yun G. S., Park H. K., Lee W., Choi M. J., Choe G. H. *et al.* (**2012**), *Appearance and dynamics of helical flux tubes under electron cyclotron resonance heating in the core of KSTAR plasmas*. Physical Review Letters, *109*, 145003.

Zakharov L., Rogers B. and Migliuolo S. (**1993**), *The theory of the early nonlinear stage of $m = 1$ reconnection in tokamaks*. Physics of Fluids B, *5*, pp.2498–2505.

The impact of two-fluid MHD instabilities on the transport of impurities in tokamak plasmas

Keywords : MHD, sawteeth, impurity transport, signal analysis
Abstract : Impurity accumulation can degrade the performance of magnetically confined fusion plasmas. In particular, heavy impurities accumulated in the core plasma dilute fusion reactants and may also lead to a radiative collapse of the plasma due to excessive cooling by radiation. Therefore, understanding the transport of heavy impurities produced by plasma-wall interaction has become a subject of utmost importance. The plasma core is likely to be affected by a magnetohydrodynamic (MHD) instability called 'internal kink' that induces relaxation oscillations named 'sawteeth'. Sawteeth are responsible for periodic relaxations of the core density and temperature and affect significantly the radial transport. Especially, particles and heat are redistributed during the crash phase the duration of which is short compared to the confinement time. In absence of MHD instabilities, impurity transport is governed by collisions (neoclassical transport) and turbulence. It is shown that neoclassical transport is important for heavy impurities in the core region of tokamak plasmas. Meanwhile, experimental measurements in the ASDEX-Upgrade tokamak show that the impurity dynamics in presence of sawteeth differs from the predictions made by transport codes. In this thesis, the numerical tool used to simulate sawteeth is the XTOR-2F code, which is a non-linear tridimensional code solving two-fluid MHD equations. Fluid equations that model the transport of impurities in a highly collisional (Pfirsch-Schlüter) regime have been implemented and coupled to the set of two-fluid MHD equations. The simulations show a difference between the impurity profiles with and without sawteeth, which is consistent with experimental observations. This results from a competition between neoclassical processes and sawtooth relaxations.■

* * *

Impact des instabilités MHD bi-fluide sur le transport d'impuretés dans les plasmas de tokamaks

Mots-clés : MHD, dents-de-scie, transport d'impuretés, analyses des signaux
Résumé : Les performances des plasmas de fusion confinés magnétiquement peuvent être dégradées par l'accumulation d'impuretés. Plus particulièrement, les impuretés lourdes accumulées au centre du plasma diluent les réactifs, et peuvent aussi conduire à un collapse radiatif du plasma par de fortes pertes par rayonnement. La compréhension du transport des impuretés lourdes produites lors de l'interaction plasma-paroi est donc devenue cruciale. Le coeur du plasma est sujet à une instabilité magnétohydrodynamique (MHD) appelée "kink interne", conduisant à des oscillations de relaxation nommées "dents-de-scie". Les dents-de-scie entraînent une relaxation périodique de densité et de température dans le coeur du plasma, et affectent significativement le transport radial. Notamment, les particules et la chaleur sont redistribuées pendant un crash dont la durée est très courte par rapport au temps de confinement. En l'absence des instabilités MHD, le transport des impuretés est porté par les collisions (transport néoclassique) et la turbulence. Il est établi que le transport néoclassique est important pour les impuretés lourdes dans la région centrale du plasma de tokamak. Cependant, des mesures expérimentales du tokamak ASDEX-Upgrade montrent que la dynamique des impuretés en présence des dents-de-scie est différente des prédictions faites par les codes de transport. Dans cette thèse, l'outil numérique utilisé pour simuler les dents-de-scie est le code XTOR-2F, qui est un code non-linéaire tridimensionnel résolvant les équations de la MHD bi-fluide. Les équations fluides modélisant le transport des impuretés dans un régime de collisionalité élevée (Pfirsch-Schlüter) ont été implémentées et couplées avec l'ensemble des équations de la MHD bi-fluide. Les simulations montrent que les profils de densité d'impuretés sont affectés par les dents-de-scie, en accord avec les observations expérimentales. Ceci résulte d'une compétition entre processus néoclassiques et relaxations dues aux dents-de-scie.■